

**New Resonant Behavior in the Spin Resolved
Photoionization of the Rare Gas Atoms Kr 3d and
Xe 4p**

Dissertation

zur Erlangung des Doktorgrades
der Fakultät für Physik
der Universität Bielefeld

vorgelegt von

Tarek Khalil

aus El Giza, Ägypten

Dezember 2002

Contents

1	Introduction.....	5
2	Theory.....	8
2.1	Interaction of atoms with electromagnetic field.....	8
2.2	Spin polarization transfer for dipole resonance.....	11
2.2.1	Characterization of Auger electrons.....	11
2.2.2	The resonantly excited Kr $3d^{-1}5p$ Auger electrons.....	13
2.2.3	Transferred spin polarization of resonantly excited Kr $3d^{-1}5p$ electrons.....	15
2.3	Nondipole contributions to the angular intensity distribution of photoelectrons.....	18
2.4	Contribution of nondipole (Quadrupole –Dipole Interference) terms to photoelectron spin polarization of the Xe 4p shell.....	21
2.5	Separation of dipole and nondipole terms in particular geometries.....	23
2.6	Nondipole spin polarization angular distribution near ionization threshold.....	25
2.7	The Quadrupole resonances in the Xe 4p photoionization.....	27
3	Experimental Setup.....	32
3.1	Synchrotron Radiation.....	32
3.2	Photoionization Apparatus.....	39
3.2.1	Electron optics.....	41
3.2.2	Voltage supply and control of the electron optics.....	43
3.2.3	Mott polarimeter.....	45
3.2.4	Channeltrons and microchannelplates as electron detectors.....	48
3.2.5	Earth's magnetic field compensation.....	49
4	Measurement of the Electron Spin Polarization.....	52
4.1	Determination of the Sherman function.....	53
5	Discussion of the statistical and instrumental errors and the uncertainties in the measurements due to background subtraction.....	54
5.1	Errors resulting from instrumental asymmetries and external fields.....	54
5.2	Calculation of the Error in the Asymmetry.....	56
5.3	Subtraction of spectral background in Xe 4p.....	58
5.3.1	Determination of the spin polarization of the net Signal.....	59
5.4	Subtraction of Background due to neighbouring resonant Kr $3d^{-1}_{3/2}$ transitions.....	60
5.4.1	The line fitting of the $h\nu$ scan of the neighboring resonant Auger transitions Kr $3d_{3/2}^{-1}5p \rightarrow 4s^{-1}4p^{-1}5p$ and Kr $3d_{5/2}^{-1}5p \rightarrow 4s^{-1}4p^{-1}6p$	63
6	Results and Discussion.....	65
6.1	Spin polarization transfer for dipole resonances.....	65
6.1.1	Resonantly excited $3d^{-1}_{5/2} 5p$ state of Krypton.....	65
6.1.2	Resonantly excited $3d^{-1}_{3/2} 5p$ state of Krypton.....	66
6.2	Quadrupole–Dipole Interference in Spin Polarization of Photoelectrons from the Xe 4p shell.....	68
6.2.1	Asymmetry parameter β close to ionization.....	70
6.2.2	Electron Correlations in Xe 4p photoelectrons.....	71
6.2.3	Transferred spin component P_{trans}	73
6.2.4	Nondipole sensitive component P_{long}	74
7	Summary.....	75
8	Appendices.....	77
8.1	Appendix 1: Intrinsic parameters and Coulomb matrix elements of the Xe $N_4O_{2,3}O_{2,3}^3P_1$ Auger decay.....	77
8.2	Appendix 2: The parameters defining the nondipole corrections to the angular distribution and spin polarization of Xe np photoelectrons [18].....	79
9	Abbreviations.....	81
10	References.....	82
11	Acknowledgements (Danksagung).....	87
12	Oath (Eidesstattliche Erklärung).....	88
13	Curriculum vitae.....	90

1 Introduction

Spinpolarization in Photoionization

Photoionization is a very important tool for the understanding of atomic and molecular structure. Photoelectrons can be distinguished not only by their kinetic energy but also by their directions of emission. The angle-resolved photoionization has therefore become a powerful tool to probe physical and chemical structures in solids and surfaces. Similarly we can study the electron spin polarization which is a very important quantum mechanical observable enabling sensitive tests of the theoretical predictions for the photoionization process.

Auger and resonant Auger electrons and their spin polarization

The Auger electron is the finally-emitted electron in the Auger process. An incident beam of particles or photons removes a primary electron from a core level of an atom to produce a vacancy. A second electron from a higher energy level fills the vacancy under release of energy. This excess energy is transferred to the ejected Auger electron.

The Resonant Auger emission is defined [4] as a scattering event in which a photon promotes an atom into an excited final state accompanied by single-electron emission. The *spectator Auger decay* is defined as a photoexcitation of an electron into a Rydberg orbital¹, where it remains as a spectator to a core Auger transition. This ‘two-step’, ‘independent-particle’ viewpoint of spectator Auger decay leads to a terminology like ‘shake-up’, ‘shake-down’ and ‘pure spectator’ transitions, since the intermediate orbitals need not coincide with the final observed orbital. This is in contrast to transitions in which the excited electron participates, which is usually distinguished as *autoionization*.

The Auger decay after atomic core photoionization can be investigated by measuring the spin polarization of the emitted Auger electrons. The spin polarization of Auger electrons was theoretically investigated by Klar [47] and was attributed to the transfer of orientation from the initial inner-shell ionization process to the decay fragments. When the atoms are photoionized by circularly polarized light, then the so-called transferred spin polarization component, i.e. the component in the direction of the photon momentum, depends basically on the orientation of the intermediate ionic states and on certain intrinsic parameters determined by the Coulomb matrix elements for the particular transition [52]. The transferred spin polarization of the Xe $M_{4,5}N_{4,5}N_{4,5}$ Auger electrons has been measured by Snell et al [69] using circularly polarized light. The hole orientation was determined from the spin polarization of the $M_4^1S_0$ Auger line allowing an extraction of a linear combination of intrinsic Auger parameters, which characterize the dynamics of the Auger decay. These intrinsic Auger parameters were determined in an isolated form by Schmidtke et al [63] from the measured angular distribution of the spin polarization of the Xe $M_{4,5}N_{4,5}N_{4,5}^3P_1$ Auger line and they have discussed the feasibility of a complete experiment for the Auger decay which aims for an extraction of all relevant quantum mechanical information describing the atomic process of interest.

¹ Rydberg orbital: an orbital with principal quantum number greater than that of any occupied orbital of the ground state.

The angular distribution of resonant Auger electrons in the rare gases was studied experimentally by Carlson et al [14], [15], Becker et al [9] and Kämmerling et al [40]. An unusually large negative value of the angular distribution parameter was found by Hergenbahn et al [31] and a close relation between the angular anisotropies of the resonant Auger and normal Auger processes was found.

Although the anisotropy parameter meanwhile is generally well understood, the anisotropy parameter of the resonant Kr $3d^{-1}5p$ Auger lines is highly sensitive to the complex details of the atomic structures. Tulkki et al [71] and Aksela et al [1] have studied the influence of the final ionic state-configuration interaction (FISCI) on the anisotropy of the resonant Kr $3d^{-1}5p$ Auger lines.

Mursu et al [58] have found that the effects of FISCI between bound $4s^{-1}4p^{-1}np$ and $4s^24p^{-3}ndnp$ final states are essentially the same as in the corresponding normal Auger spectra. Kitajima et al [46] have studied the anisotropy parameter of the resonant Auger transitions from Kr $3d^{-1}5p$ to the bound $4s^{-1}4p^{-1}5p$ and $4s^25p$ levels experimentally and theoretically using multiconfiguration Dirac-Fock (MCDF) calculations including correlations of all the states involved. The MCDF calculations gave the energy position of the main spectral lines and their intensities satisfactorily, which is important for the analysis of the measured transferred spin polarization of these lines. The first step spectator transitions are found to be strongly anisotropic. The calculations agree very well with the experiment. In this thesis transferred spin polarization of the resonantly excited Kr $3d^{-1}_{5/2} 5p_{3/2}$ and the two coherently excited levels Kr $3d^{-1}_{3/2} 5p_{3/2}$ and Kr $3d^{-1}_{3/2} 5p_{1/2}$ was measured.

Breakdown of the Dipole Approximation in the Description of Photoionization at low Photon Energies

The dipole approximation assumes the spatial distribution of the electromagnetic field of the photon, $\exp(i\mathbf{k}\mathbf{r})$ where \mathbf{k} is the photon wave vector and \mathbf{r} is the position vector, to be expressed as a Taylor-series expansion, $1 + i\mathbf{k}\mathbf{r} + \dots$, which can be approximated to unity if all higher-order interactions are neglected [10]. The dipole approximation in photoionization by low energy photons in the far UV photon energy range is based on the qualitative argument that the wavelengths are much larger than the atomic dimensions corresponding to the Bohr radius a_0 .

Deviations from the dipole approximation in the angular distribution of photoelectrons energy were attributed to photon-electron momentum transfer [20] and were first observed by Krause [49] and Wuilleumier [74] and recently by Krässig 1995 et al [48] who measured the nondipole contribution to the angular distribution of Ar 1s photoelectrons in the 3.2-5.2 keV photon energy range. They found experimentally that the nondipolar interaction results in a forward-backward asymmetry. The nondipole contribution to the angular distribution of the Ne 2s and 2p photoelectrons was demonstrated at low photon energies in 250-1200 eV photon energy range by Hemmers et al [30]. The asymmetry parameters characterizing the first order nondipole contribution to the angular distribution of photoelectrons have been calculated by Derevianko et al [23] for photoelectron energies ranging from 20 to 5000 eV for all subshells of the rare gas atoms He, Ne, Ar, Kr, and Xe in the relativistic independent-particle approximation theory IPA. An experimental and theoretical study by Derevianko et al [24] of the angular distributions of neon valence photoelectrons in the 100–1200 eV photon-energy range revealed a breakdown of the dipole approximation in the angular distribution for Ne 2p photoelectrons. These significant second-order nondipole effects are primarily due to electric-octopole and pure-electric-quadrupole interactions in low energy photoionization.

The higher multipole corrections to the spin polarization of photoelectrons, resulting from polarized photons, ejected from the $2p_J$ subshell were investigated by Bechler et al [7] using a nonrelativistic approach. The contribution of the electric-dipole-electric-quadrupole interference terms of the spin polarization of photoelectrons from Xe 4p and 5p shells has been calculated by Cherepkov et al [17] using the non relativistic random phase approximation with exchange and they showed that this nondipole contribution to spin polarization near the ionization threshold can be observed in a definite measurement geometry. Cherepkov et al [18] have attributed this nondipole effect to a quadrupole resonance resembling the well-known dipole resonance of Xe 4d photoelectrons. In this thesis the spin polarization of Xe 4p photoelectrons was measured near ionization threshold and for the first time a non-vanishing nondipole contribution to spin polarization was verified.

2 Theory

2.1 Interaction of atoms with electromagnetic field

The Interaction between atoms and electromagnetic radiation can be described in a **semi-classical model**¹, in which the interaction is treated by time-dependent perturbation theory [73]. This perturbation results from a classical radiation field, which is regarded as a superposition of plane waves periodic in time. In this situation we will have a weak external time-dependent field which induces the atom to emit or absorb one photon.

The time dependent perturbation H' in the Hamiltonian will be then:

$$H' = e/m \mathbf{A}(t) \cdot \mathbf{p}, \quad (2-1 1)$$

The time dependence of H' is determined through the vector potential $\mathbf{A}(t)$ characterising the radiation and e , m and \mathbf{p} are the charge, mass and momentum of the electron respectively. $\mathbf{A}(t)$ can be represented as a monochromatic plane wave. We assume our atomic system has two non-degenerate stationary states $|i\rangle$ and $|j\rangle$. The transition rate for photon absorption is mainly characterised through the matrix element of the perturbation connecting these stationary states $|i\rangle$ and $|j\rangle$:

$$|\langle j | (e/m) \mathbf{e} \cdot \mathbf{p} \exp(i\mathbf{k} \cdot \mathbf{r}) | i \rangle|^2, \quad (2-1 2)$$

where \mathbf{e} is a unit vector in the direction of $\mathbf{A}(t)$ (polarization of the photon) and \mathbf{k} is the wave vector: $\mathbf{k} = 2\pi/\lambda$, λ is the wave length. The spatial dependence of interacting photon is expressed by the factor $\exp(i\mathbf{k} \cdot \mathbf{r})$ which can be expanded:

$$\exp(i\mathbf{k} \cdot \mathbf{r}) = 1 + i\mathbf{k} \cdot \mathbf{r} + \dots, \quad (2-1 3)$$

when the wave length $\lambda \gg r$ that is the amplitude of the wave is constant over the atom, then the factor $\exp(i\mathbf{k} \cdot \mathbf{r})$ is ≈ 1 which is called the *electric dipole approximation*. In this electric dipole approximation the transition matrix element in (2-1 2) will take the form (assuming \mathbf{A} is polarized in the x-direction):

$$\langle j | p_x | i \rangle = \langle j | m dx/dt | i \rangle = 2i\pi/h \langle j | H_{0x-x} H_0 | i \rangle, \quad (2-1 4)$$

where we have used

$$dx/dt = 2i\pi/h [H_0, x], \quad (2-1 5)$$

¹ This discussion can be read in detail in chapter 3 of G. K. Woodgate. See References.

and H_0 is the Hermitian unperturbed Hamiltonian ($H_0|i\rangle = E_i|i\rangle$) and h is the Planck's constant, then we will have

$$\langle j|(e/m)p_x|i\rangle = 2i\pi/mh (E_j-E_i) \langle j|ex|i\rangle, \quad (2-1 6)$$

and the atomic part of the problem is reduced to the matrix element of the electric dipole operator ex .

The inclusion of the second term in the expansion (2-1 3) leads to the *magnetic dipole* and *electric quadrupole* terms.

In the matrix element in (2-1 2) the electron momentum \mathbf{p} is projected onto the vector potential \mathbf{A} , due to the transverse nature of the electromagnetic wave we have $\mathbf{k}\cdot\mathbf{A} = 0$, this means that only the component of \mathbf{p} is important for which $\mathbf{k}\cdot\mathbf{p} = 0$. Taking for example $\mathbf{k} = k_x\mathbf{x}$ and $\mathbf{p} = p_y\mathbf{y}$ (\mathbf{x} and \mathbf{y} are unit vectors), the squared matrix element (2-1 2) will be in this higher order approximation:

$$|\langle j|(e/m) p_y (1+ik_x x) |i\rangle|^2, \quad (2-1 7)$$

The relatively small second order multiple operator is the interesting one now, thus we consider:

$$|\langle j|(ie\omega/mc) p_y x) |i\rangle|^2, \quad (2-1 8)$$

where we have put $k_x = \omega/c$.

Since $[x,p_y] = 0$, then we can write xp_y as follows:

$$xp_y = 1/2 (xp_y - p_x y) + 1/2 (xp_y + p_x y) = \pi h l_z + 1/2 m(x dy/dt + dx/dt y), \quad (2-1 9)$$

the first term in the sum (2-1 9) above $\pi h l_z$ (l_z is the z-component of the orbital angular momentum) leads to the magnetic dipole term :

$$\text{magnetic dipole term: } (\omega^2/c^2) |\langle j|(eh/4\pi m) l_z|i\rangle|^2 = (\omega^2/c^2) |\langle j| \mu_{lz}|i\rangle|^2, \quad (2-1 10)$$

where $(eh/4\pi m) l_z = \mu_{lz}$ is the z-component of the magnetic dipole moment of the atom.

The second term in the sum (2-1 9) can be written as:

$$\begin{aligned} 1/2 m(x dy/dt + dx/dt y) &= \pi mi/h (xH_{0y} - xyH_0 + H_0xy - xH_{0y}) \\ &= \pi mi/h (H_0xy - xyH_0). \end{aligned} \quad (2-1 11)$$

As in (2-1 6) the contribution of this term to the matrix element will lead to the *electric quadrupole term*:

$$(e^2 \omega^2 \pi^2 / c^2 \hbar^2) (E_j - E_i) |\langle j | \text{exy} | j \rangle|^2 = \omega^4 / 4c^2 |\langle j | \text{exy} | j \rangle|^2, \quad (2-1 12)$$

where $2\pi(E_j - E_i) / \hbar =: \omega$.

Both magnetic dipole and electric quadrupole terms are greatly reduced relative to the electric dipole by the factor $Z^2 \alpha^2$, where Z is the atomic number and α is the fine structure constant.

2.2 Spin polarization transfer for dipole resonance

2.2.1 Characterization of Auger electrons

One major object of the spin resolved spectroscopy on Auger electrons is to characterise the Auger decay completely i.e. to extract all matrix elements representing all possible channels of the Auger decay from the experimentally accessible observables.

For the case of non resonant Auger decay it was found [63] that an exclusive measurement of Auger electron properties is not sufficient to extract all matrix elements because the intrinsic parameters (the experimentally accessible observables) are intertwined. In this experiment [63] the intrinsic parameters β_1, γ_1 and α_2 were determined from measurement of the transferred spin polarization of the two lines Xe N₅ O_{2,3} O_{2,3} ¹S₀ and Xe N₄ O_{2,3} O_{2,3} ³P₁ and their angular distribution using circularly polarized light and then using a fitting procedure. The intrinsic parameters describe the dynamical properties of the decay process. The relation between the spin polarization of Auger electrons and the intrinsic parameters is shown in Appendix 1(A1 1 – A-1 4).

In the case of the Xe N₄ O_{2,3} O_{2,3} ³P₁ Auger decay there are only three allowed outgoing partial waves due to the conservation of the angular momentum and parity [38]

$$\text{Xe}(4d)^{-1} \ ^2D_{3/2} \rightarrow \text{Xe}(5p)^{-2} \ ^3P_1 + \begin{cases} \varepsilon s_{1/2} \rightarrow M_1, \Delta_1 \\ \varepsilon d_{3/2} \rightarrow M_2, \Delta_2 \\ \varepsilon d_{5/2} \rightarrow M_3, \Delta_3 \end{cases} \quad (2-2 \ 1)$$

Associated with these transitions are three reduced Coulomb matrix elements with amplitude M_i and complex phase factor $\exp i\Delta_k$ [52]. If the ratios of the amplitudes of the reduced Coulomb matrix elements are considered then we will have four independent quantum mechanical quantities describing this Auger decay [38] :

$$\eta_1 = M_1/M_3, \quad (2-2 \ 2)$$

$$\delta_1 = \Delta_1 - \Delta_3, \quad (2-2 \ 3)$$

$$\eta_2 = M_2/M_3, \quad (2-2 \ 4)$$

$$\delta_2 = \Delta_2 - \Delta_3, \quad (2-2 \ 5)$$

It was found that in analogy with the photoionization case [62], there is an equation connecting the intrinsic parameters for the Auger decay Xe N₄ O_{2,3} O_{2,3} ³P₁. This equation is valid for the particular Auger transition $(4d_{3/2})^{-1} \rightarrow (5p)^{-2} \ ^3P_1$.

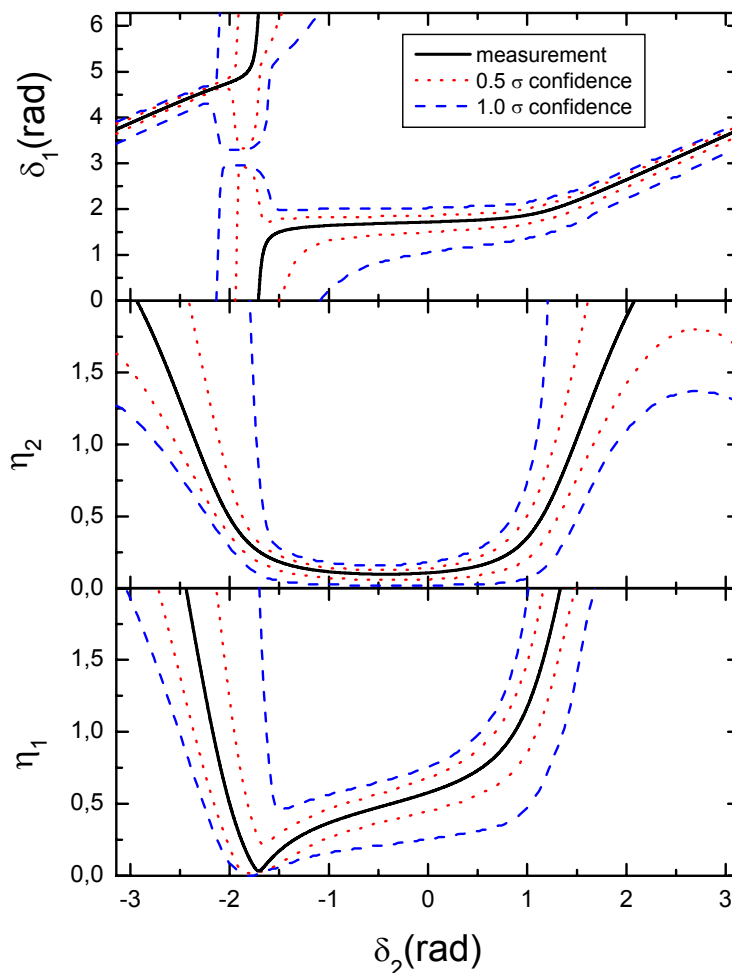
$$(\alpha_2 - 3/2 \sqrt{5}\gamma_1)^2 + (2\xi_2)^2 = (1+\alpha_2)(5 - 3\sqrt{5}\beta_1). \quad (2-2 \ 6)$$

As a consequence of equation(2-2 6) one of the parameters α_2 , β_1, γ_1 , and ξ_2 is redundant and can be evaluated knowing the others. The ξ_2 parameter describing the dynamical spin polarization has not been measured and can be determined from this equation.

The intrinsic parameters β_1, γ_1 , α_2 and ξ_2 can be expressed as functions of the involved Coulomb matrix elements. See Appendix 1(A1 5 – A-1 8)

Now there are three known non-redundant experimental parameters α_2 , β_1, γ_1 and four unknown Coulomb matrix elements; two amplitude ratios and two phase shift differences η_1 , η_2 , δ_1 and δ_2 . The extraction of these quantities from the intrinsic parameters corresponds to an inversion of the formulae given in Appendix 1. The problem of inversion of these formulae corresponds to find a solution in a one-dimensional subspace of the four dimensional space spanned by η_1 , η_2 , δ_1 and δ_2 .

In figure(2-2 1) this one-dimensional subspace is determined by the three projections of η_1 , η_2 , and δ_1 onto the δ_2 coordinate, while the relativistic phase shift difference δ_2 has been chosen as the independent variable.



Figure(2-2 1). Solution space of the Coulomb matrix element ratios and phase shift differences for the Xe $N_4O_{2,3}O_{2,3}^3P_1$ Auger decay transition. The solid curve represents the solution which corresponds to the measured values of the experiment. The dotted/dashed curves make up the area which may be occupied if the measured intrinsic parameters 0.5s/1s, respectively. Source: B. Schmidtke et al J.Phys. B. At. Mol. Phys. 33 , 5225 (2000).

The extracted amplitude ratios and the phase shift differences are interconnected due to the interdependence between the intrinsic parameters specified by equation (2-2 6) and the solution must be a one-dimensional space, then a mathematically unambiguous extraction of Coulomb matrix element ratios and phase shift differences is possible if at least one further approximation is made; physically meaningful constraints reduce the possible range of values considerably. As a consequence of the above-discussed interconnection of the intrinsic parameters additional information about the orientation of the intermediate states of the Auger decay is necessary to carry out a complete experiment.

2.2.2 The resonantly excited Kr $3d^{-1}5p$ Auger electrons

The resonant Auger transitions correspond to the excitation of an inner shell electron to one of the unoccupied outer-shell orbitals, the Rydberg orbitals [45]. The ion core of Kr is differentiated into two states of total angular momentum $j = \ell \pm 1/2$ due to the LS coupling of the angular momentum ℓ and the spin $1/2$ of the hole in the inner shell. The resulting two states of the core $3d_{3/2}$ and $3d_{5/2}$ have then a separation of the order of 1 eV. The inspected resonant Auger spectrum arising from the transitions of the Kr $3d^{-1}5p$ to the states with configurations $4s^{-1}4p^{-1}np$ and $4s^{-2}np$ have the following features:

The spectrum analyzed by Mursu et al [58] is characterized by a strong final ionic state interaction FISCI. *The correlation satellites* result from the strong mixing of the final-state configurations $4s^{-1}4p^{-1}np$ of the diagram transitions with the states $4s^{-2}4p^{-3}mnp$ configurations. *The shake-up satellites* result when the spectator $5p$ electron is shaken up to an upper orbital in the Auger decay.

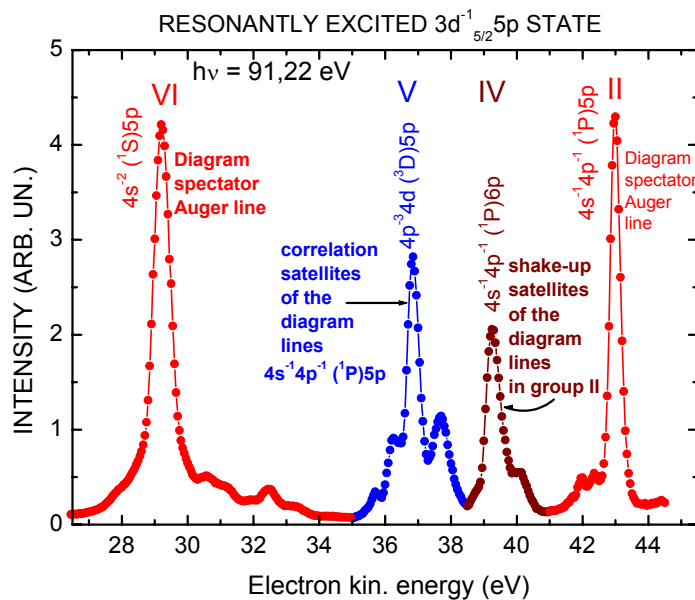


Figure (2-2 2). The resonant Auger electron spectrum of Kr $3d^{-1}_{5/2} 5p$ at photon energy 91.22 eV.

The roman numerals correspond to Kitajima et al [46]. The spectrum is measured at BESSY II, the first part of the spectrum (Peak VI) is measured at constant pass energy $E_p = 40$ eV, the rest of the spectrum is measured at $E_p = 25$ eV.

Kitajima et al [46] have performed a high resolution measurement of angular distribution of the resonant Kr $3d^{-1}5p$ Auger electrons and analyzed the measured data including the correlation satellites theoretically. They used MCDF calculations with FISCO in the configuration space that includes the $4s^24p^{-3}4d5p$ configuration. The calculations have considered the interference effects due to the overlapping of some contributing resonances. The wavefunctions are calculated using the MCDF method for

- the *initial resonances*,
- the *intermediate levels* and
- the *final states* of the two-step Auger cascade.

The three initial resonances with $J = 1$ dipole excitation; the level $3d^{-1}_{5/2} 5p_{3/2}$ and the two coherent excited levels $3d^{-1}_{3/2} 5p_{3/2}$, $3d^{-1}_{3/2} 5p_{1/2}$ are well separated and can be, described in *single non-relativistic configuration approximation*.

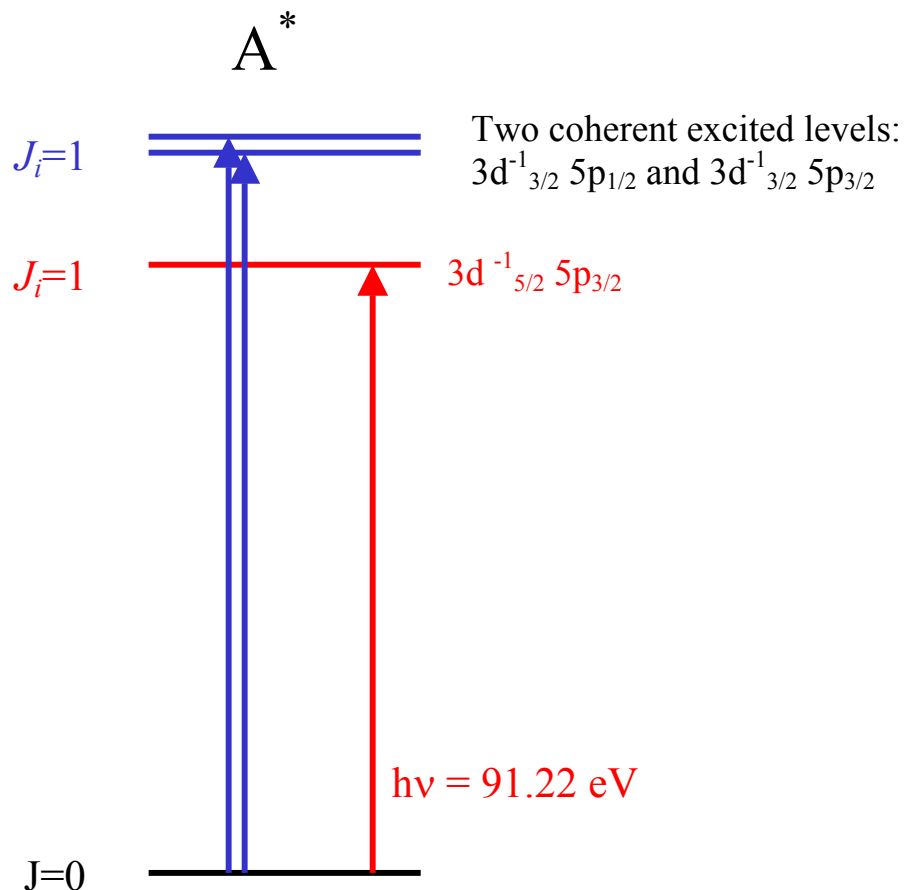


Figure (2-2 3). The dipole excitation of resonantly excited Kr $3d^{-1} 5p$ leads to three initial resonances with $J = 1$.

The wavefunction of these initial resonances has been used for calculating the first step Auger amplitudes and the electric dipole excitation of the two levels $3d^{-1}_{3/2} 5p_{3/2}$, and $3d^{-1}_{3/2} 5p_{1/2}$.

2.2.3 Transferred spin polarization of resonantly excited Kr $3d^{-1}5p$ electrons

The transferred spin polarization component [52] of the resonantly excited Kr $3d^{-1}5p$ electrons was measured in the electron-fixed frame shown in figure (2-2 4).

$$P_x = -(1 + \alpha_2 A_{20} P_2(\cos\Theta))^{-1} \xi_1 A_{10} \sin\Theta, \quad (2-2 7)$$

for $\Theta = 90^\circ$:

$$P_x = -(1 - 1/2 \alpha_2 A_{20})^{-1} \xi_1 A_{10}, \quad (2-2 8)$$

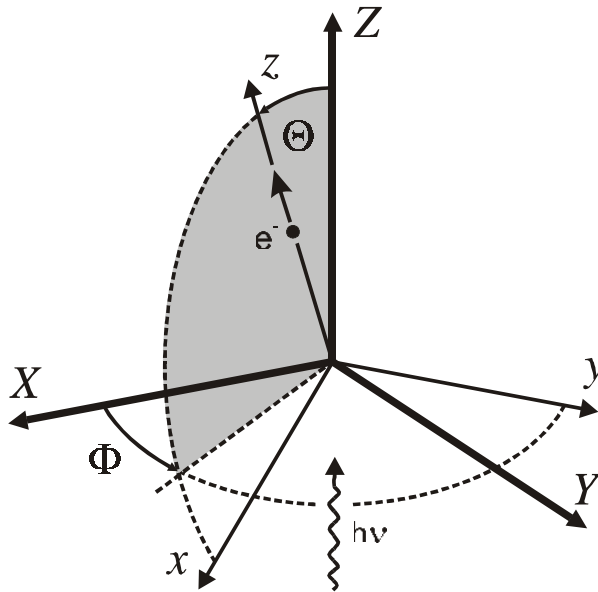
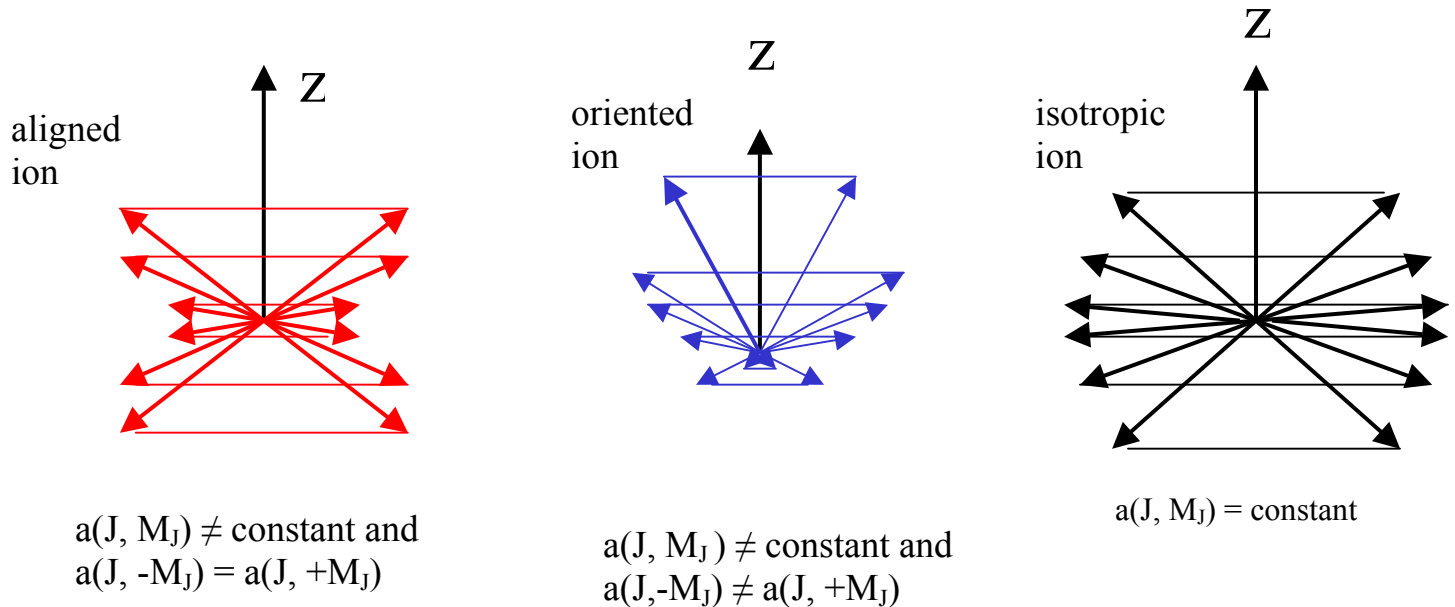


Figure (2-2 4). The Z-axis of the laboratory coordinate frame (X, Y, Z) is oriented along the photon beam whereas the electron-fixed frame (x, y, z) is oriented along the direction of the Auger electron.

where A_{10} and A_{20} are the orientation and alignment of the resonance, $P_2(\cos\Theta)$ is the second Legendre polynomial, α_2 is the intrinsic anisotropy parameter which determines the angular intensity distribution of Auger electrons, the product $\alpha_2 A_{20}$ is the angular distribution parameter β_{Auger} of the Auger electrons. The intrinsic parameter ξ_1 characterizes the spin polarization component P_x .



Figure(2-2 5) Vector model illustration of the concepts of alignment and orientation of an axially symmetric system JM_J , $J = 5/2$.

The orientation A_{10} and the alignment A_{20} are parameters which characterize the probability distribution of magnetic sublevels of the primary hole state (vacancy) induced by the photoionization process [55]. An ensemble of atoms having the total angular momentum J can have different populations $a(J, M_J)$ corresponding to the different substates M_J . When the substates M_J are not isotropic i.e. there is a certain polarization of these substates, we have either an oriented or an aligned state [61]¹. See figure (2-2 5).

- $a(J, M_J) = \text{constant}$:isotropy, (2-2 9)
- $a(J, M_J) \neq \text{constant}$ and $a(J, -M_J) = a(J, +M_J)$:alignment, (2-2 10)
- $a(J, M_J) \neq \text{constant}$ and $a(J, -M_J) \neq a(J, +M_J)$:orientation. (2-2 11)

Only when circularly polarized radiation is used, the ion orientation will be different from zero. The intrinsic parameter ξ_1 is geometrically related to β_1 and γ_1 by the transformation:

$$\xi_1 = \gamma_1/2 - \beta_1. \quad (2-2 12)$$

The intrinsic parameters β_1 and γ_1 describe, in the laboratory frame, the integral transferred spin polarization along the photon beam and its angular dependence [52].

The orientation and the alignment parameters for the resonant excitation from the ground state (1S_0) by circularly polarized light are known [6]² or [39]; their value depends only on the value of J which is 1 for the three transitions we have [46]:

¹ V. Schmidt Electron Spectroscopy of Atoms using Synchrotron Radiation Cambridge University Press 1997 page 91

² V. V. Balashov, A. N. Grum-Grzhimailo and N. M. Kabachnik 2000 Polarization and correlation Phenomena in Atomic Collisions. A Practical Theory Course (New York: Kulwer Academic) page 59

$$A_{10} = \sqrt{3/2}, \quad A_{20} = \sqrt{1/2}, \quad (2-2 13)$$

to calculate the ξ_1 parameter, the following expression may be used[39], [52]

$$\xi_1 = 1/N \sum_{j,j'} c_1(j,j') X_{jj'}^1 M_{J_i(\ell)j} M_{J_i(\ell)j'}^*, \quad (2-2 14)$$

where $M_{J_i(\ell)j}$ is the amplitude (reduced matrix element) of the Auger decay from the well defined atomic state $|\alpha_i J_i\rangle$; J_i is the angular momentum of the state and α_i denotes all other quantum numbers including parity. The final state of the ion is $|\alpha_f J_f\rangle$ and the emitted Auger electron is characterized by the orbital and total angular momenta ℓ, j

$$M_{J_i(\ell)j} \equiv \langle \alpha_f J_f, \ell j : J_i || V || \alpha_i J_i \rangle, \quad (2-2 15)$$

$$\text{where } c_1(j,j') = 1/4 (-1)^\ell [(-1)^{j-1/2} (2j+1) + (-1)^{j'-1/2} (2j'+1)], \quad (2-2 16)$$

$$N = \sum_j |M_{J_i(\ell)j}|^2, \quad (2-2 17)$$

and

$$X_{jj'}^1 = (-1)^{J_i+J_f+1/2} (2j+1) (-1)^{j+j'} (2j+1) (2j'+1) (j+1/2, j-1/2 | 10) \left\{ \begin{matrix} J_i & J_i & 1 \\ j & j & J_f \end{matrix} \right\}, \quad (2-2 18)$$

where the standard notation for the Clebsch-Gordan and 6j coefficients is used.

2.3 Nondipole contributions to the angular intensity distribution of photoelectrons

The assumption that the dipole approximation is sufficient to describe the photoionization process for photon energy below 1 keV is no longer accepted as being exact . For example there are many studies [30], [24]and [48] which manifest nondipole contributions for the angular distribution of photoelectrons. B. Krässig et al [48] have investigated the nondipolar contribution to the angular distribution of Ar photoelectrons in the 3.2 - 5.2 keV photon energy range. In the dipole approximation the differential cross section for photoionization by a linearly polarized light is given by :

$$d\sigma/d\Omega = (\sigma/4\pi)[1+\beta P_2(\cos\theta)], \quad (2-3 1)$$

where σ is the angle integrated cross section, θ is the angle between the photon polarization and the photoelectron momentum vectors, $P_2(\cos\theta)$ is the second Legendre polynomial, $P_2(\cos\theta) = 1/2 (3\cos^2(\theta) - 1)$, β is the photoelectron asymmetry parameter. In the dipole approximation the photoelectron angular distribution depends only on the angle θ .

Cooper [21] has considered the nondipolar contribution (the interference between the electric dipole and electric quadrupole photoionization amplitudes) to the angular distribution of photoelectrons and the following equation for the differential cross section for photoionization with linearly polarized light was given as

$$d\sigma/d\Omega = (\sigma/4\pi)[1+\beta P_2(\cos\theta)+(\delta+\gamma\cos^2\theta)\sin\theta \cos\phi], \quad (2-3 2)$$

where the asymmetry parameters δ and γ characterize the nondipolar contribution. ϕ is the azimuthal angle between the photon propagation vector \mathbf{k} and the projection of photoelectron momentum vector \mathbf{p} in the plane perpendicular to the photon polarization vector $\boldsymbol{\varepsilon}$.

See figure (2-3 1).

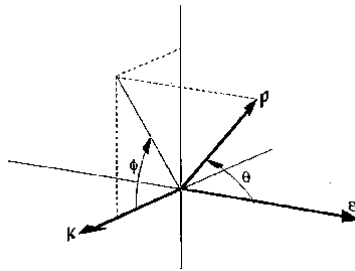


Figure (2-3 1). Coordinates used for the description of photoelectron angular distribution: θ is the polar angle of the photoelectron momentum vector \mathbf{p} with respect to the photon polarization vector $\boldsymbol{\varepsilon}$, and ϕ is the azimuthal angle defined by the projection of \mathbf{p} in the plane perpendicular to $\boldsymbol{\varepsilon}$ and containing the photon propagation vector \mathbf{k}

Equation (2-3 2) can be simplified when the measurement is carried out at the magic angle $\theta = 54.7^\circ$, where $P_2(\cos\theta) = 0$, and by rotating the spectrometer in ϕ . Then equation (2-3 2) becomes:

$$I(\phi) = 1 + (2/3)^{1/2}(\delta+\gamma/3)\cos\phi. \quad (2-3 3)$$

For the Ar 1s photoelectrons we have, due to theory [21], $\beta = 2$ and $\delta = 0$. Then equation (2-3 3) will be :

$$I(\phi) = 1 + (2/27)^{1/2} \gamma \cos\phi. \quad (2-3 4)$$

This ϕ dependence of the cross section of Ar 1s photo electrons due to the asymmetry parameter γ is confirmed experimentally as shown in figure (2-3 2) at a photon energy of 2000 eV

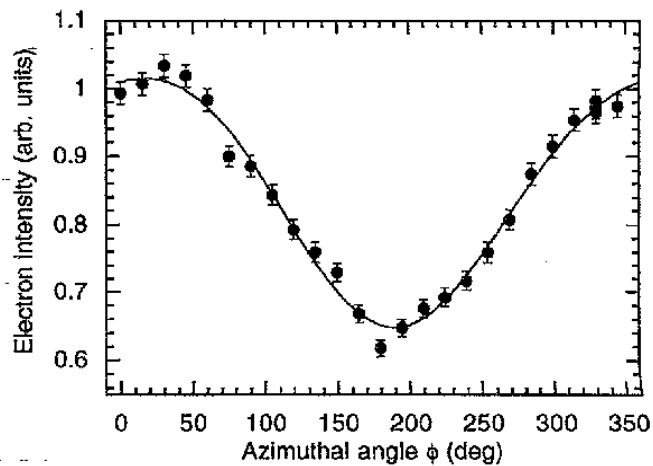


Figure (2-3 2) Dependence on azimuthal angle ϕ of 2000 eV Ar 1s photoelectrons at a fixed polar angle $\theta = 54.7^\circ$. The solid line is a fitted curve used to determine γ Source: B. Krässig et al Phys. Rev. Lett. **75**, 4736 (1995)

The measured γ values for Ar 1s are plotted in figure (2-3 3). The calculated asymmetry γ from Cooper is plotted too in the figure, the γ parameter depends on the kinetic energy of the photoelectrons, and *this asymmetry γ parameter does not vanish for low photoelectron energy.*

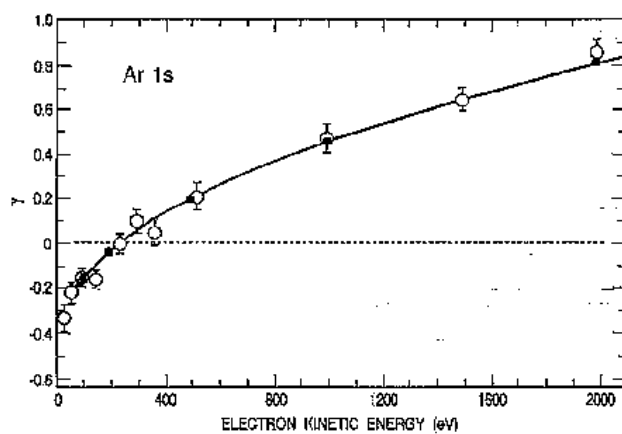


Figure (2-3 3) Dependence on electron kinetic energy of measured values of the Ar 1s nondipolar asymmetry parameter γ compared with Cooper's calculated values(solid circles with spline-fit line) Source: B. Krässig et al Phys. Rev. Lett. **75**, 4736 (1995)

2.4 Contribution of nondipole (Quadrupole –Dipole Interference) terms to photoelectron spin polarization of the Xe 4p shell

Y. S. Kim et al [44] has predicted that for photon-photoelectron polarization correlations in $np_{1/2}$ - and $np_{3/2}$ -subshell photoionization of uranium, deviations from dipole approximation may be visible for spin polarization parameters even at low photon energies. A. Bechler et al [7] have investigated multipole effects in the spin and polarization correlations for 2p photoelectrons in the nonrelativistic framework using the Independent Particle Approximation. They found small corrections to the dipole approximation at low energies and low Z , which increase with energy and atomic number.

N. A. Cherepkov and S. K. Semenov [17] calculated non-relativistically the contribution of electric-dipole-electric-quadrupole interference terms to the spin polarization of Xe 4p photoelectrons in the photon energy range below 350 eV. They investigate the first nondipole corrections of photoelectrons ejected from atomic subshells with $\ell > 0$.

In the dipole approximation the differential photoionization cross section $I_j^\lambda(\kappa, \mathbf{s})$ for the ejection of photoelectrons in some direction κ with spin \mathbf{s} , is given by [16]

$$I_j^\lambda(\kappa, \mathbf{s}) = [\alpha\omega p / (2j+1)] \sum_{\mu_1, \mu_2, m_j} \langle \psi_{n\ell j m_j} | d_\lambda^* | \psi_{p\mu_1}^- \rangle 1/2(1+\sigma\mathbf{s}) \langle \psi_{p\mu_2}^- | d_\lambda | \psi_{n\ell j m_j} \rangle, \quad (2-4 1)$$

where the subscript $\lambda = \pm 1$ is the photon helicity for circularly polarized light, and $\lambda = 0$ for linearly polarized light,

$\psi_{n\ell j m_j}$ is the initial state wave function, the subscripts n, ℓ, j, m_j are the quantum numbers of the initial state, and

$\psi_{p\mu}^-$ is the final state electron wave function. The subscript p denotes the direction of the electron momentum \mathbf{p} , the subscript μ is the spin projection on the quantization axis which is the direction of the photon polarization vector for linearly polarized light and the direction of photon beam for circularly polarized light.

$d_\lambda = (4\pi/3)^{1/2} r Y_{1\lambda}(\theta, \phi)$ is the dipole operator with r being the position operator and $Y_{1\lambda}(\theta, \phi)$ are the spherical harmonics.

$1/2(1+\sigma\mathbf{s})$ is the spin projection operator with σ being the Pauli matrix vector and

α characterizes the direction of \mathbf{s} and ω is the photon energy.

Summation over all projections in (2-4 1) leads to [16], [28] the following expression of the differential photoionization cross section $I_j^\lambda(\kappa, \mathbf{s})$ for the ejection of photoelectrons in some direction κ with spin \mathbf{s} in a vector form independent of the particular choice of coordinate frame:

$$I_j^\lambda(\kappa, \mathbf{s}) = (\sigma_{n\ell j}(\omega)/8\pi) \{ 1 + ((2-3\lambda^2)/2)\beta^j P_2(\mathbf{k}\kappa) + \lambda A^j(\mathbf{s}\mathbf{k}) - \lambda\gamma^j [3/2(\kappa\mathbf{k}) - 1/2(\mathbf{s}\mathbf{k})] + 2(2-3\lambda^2)\eta^j(\mathbf{s}\kappa\mathbf{k})(\kappa\mathbf{k}) \} \quad (2-4 2)$$

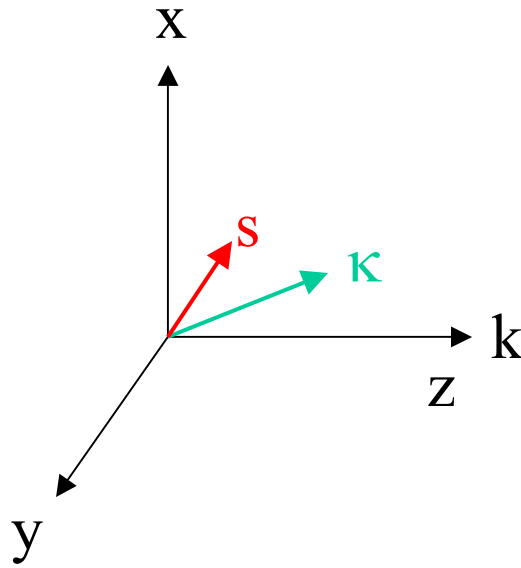


Figure (2-4 1). The direction of the circularly polarized photon \mathbf{k} , the photoelectron $\boldsymbol{\kappa}$ and the spin polarization \mathbf{s} .

$\boldsymbol{\kappa}$, \mathbf{s} and \mathbf{k} are unit vectors in the directions of the photoelectron, the spin polarization and the photon beam. See figure (2-4 1).

$\sigma_{n\ell j}(\omega)$ is the partial photoionization cross section of the subshell with quantum numbers n , ℓ and j .

β^j is the angular asymmetry parameter.

A^j , γ^j and η^j are the polarization parameters defining the polarization of the photoelectrons. They are derived in [16].

To investigate the nondipole contribution [17], the next term in the operator for photon electron interaction (see section 2.1) must be considered :

$$H_{\text{int}}(\mathbf{r}) \sim \mathbf{e}\mathbf{p}[1+i\mathbf{k}\mathbf{r}]. \quad (2-4 3)$$

This leads to the correction of the dipole operator d_λ in (2-4 1) :

$$d_\lambda \rightarrow d_\lambda + ikq_\lambda, \quad (2-4 4)$$

where $q_\lambda = (4\pi/15)^{1/2} (r^2/2) Y_{2\lambda}(\theta, \phi)$.

The electric-quadrupole correction ikq_λ to the electric-dipole approximation is of the order $Z\alpha$, where α is the fine structure constant, while the first relativistic corrections are of the

order of $(Z\alpha)^2$. Therefore the electric-dipole-electric-quadrupole interference terms are calculated using non-relativistic wavefunctions.

Taking the quadrupole corrections into account, then equation (2-4 2) will be for circularly polarized light:

$$\begin{aligned} I_{\pm}^{\pm}(\kappa, \mathbf{s}) = & 1/2 \sigma_{nlj}(\omega) [B_{000}^j Y_{00}^{00}(\kappa, \mathbf{s}) + B_{220}^j Y_{20}^{20*}(\kappa, \mathbf{s}) + B_{110}^j Y_{10}^{10*}(\kappa, \mathbf{s}) \\ & + B_{330}^j Y_{30}^{30*}(\kappa, \mathbf{s}) \pm B_{101}^j Y_{01}^{01*}(\kappa, \mathbf{s}) \pm B_{121}^j Y_{10}^{21*}(\kappa, \mathbf{s}) + B_{221}^j Y_{20}^{21*}(\kappa, \mathbf{s}) \\ & + B_{111}^j Y_{10}^{11*}(\kappa, \mathbf{s}) \pm B_{211}^j Y_{20}^{11*}(\kappa, \mathbf{s}) \pm B_{231}^j Y_{20}^{31*}(\kappa, \mathbf{s}) + B_{331}^j Y_{30}^{31*}(\kappa, \mathbf{s})], \end{aligned} \quad (2-4 5)$$

where the $Y_{y_0}^{Lx}$ are the bipolar spherical harmonics, some of the parameters B_{yLX}^j are the polarization parameters in the electric-dipole approximation and the rest are new parameters defining the nondipole corrections. See Appendix 2.

2.5 Separation of dipole and nondipole terms in particular geometries

To observe the contribution of the nondipole terms in photoelectron spin polarization we can measure the spin polarization in a definite experimental geometry in which the electric-dipole approximation vanishes at the photoelectron ejection direction κ .

The electric-dipole approximation will be zero when both unit vectors κ and \mathbf{s} are perpendicular to \mathbf{k} [17].

In the geometry where all three unit vectors are mutually perpendicular, $\kappa \perp \mathbf{k}$, $\mathbf{s} \perp \mathbf{k}$ and $\kappa \perp \mathbf{s}$, the transverse polarization $P_{\text{perp}}^{\pm 1}$ is:

$$P_{\text{perp}}^{\pm 1} = (1 + 1/4 \beta)^{-1} (-3i/\sqrt{2} (B_{111}^{1/2} - \sqrt{7/2} \sqrt{2} B_{331}^{1/2})). \quad (2-5 1)^1$$

In the geometry where: $\kappa \perp \mathbf{k}$ and $\mathbf{s} \parallel \kappa$, the longitudinal polarization $P_{\text{long}}^{\pm 1}$ will have no electric-dipole contribution:

$$P_{\text{long}}^{\pm 1} = \pm (1 + 1/4 \beta)^{-1} (\sqrt{6/2} (B_{211}^{1/2} + \sqrt{3/2} B_{231}^{1/2}) = \pm (2 + \beta/2)^{-1} (-\delta) \quad (2-5 2)$$

¹ In this expression the symbol i is the imaginary number $\sqrt{-1}$. The whole expression is real because $B_{111}^{1/2}$ and $B_{331}^{1/2}$ are complex numbers, see Appendix 2.

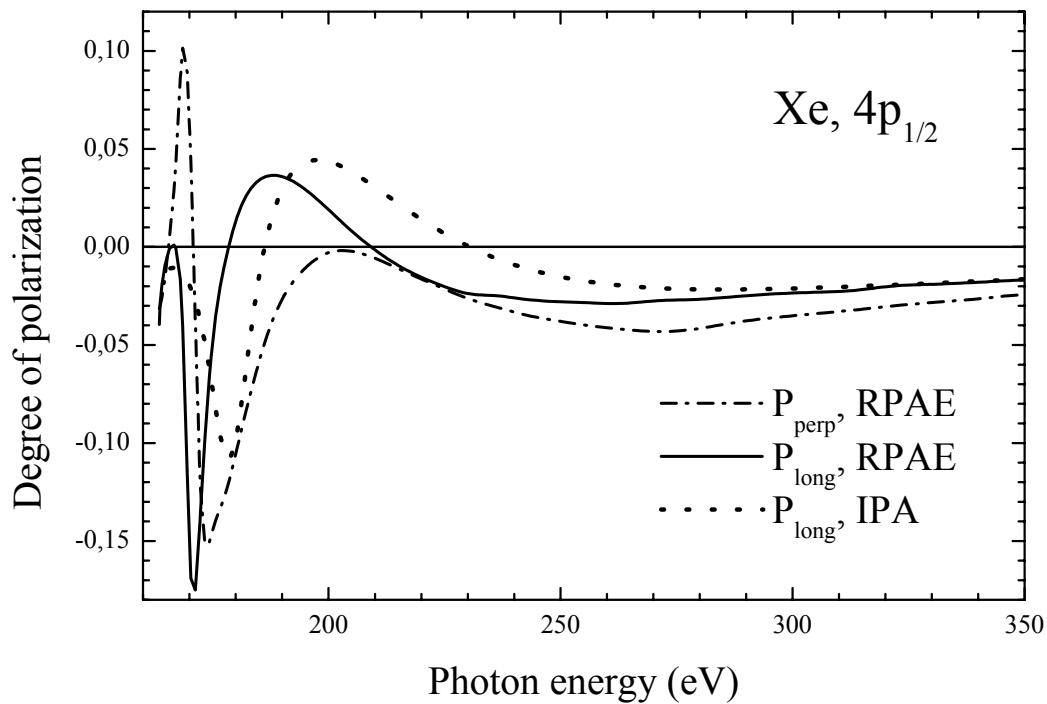


Figure (2-5 1). The two spin polarization components of Xe $4p_{1/2}$ P_{perp} (equation (2-5 1)) and P_{long} (equation (2-5 2)) as a function of photon energy calculated in RPAE. The result of the IPA calculation of Derevianko is also shown. Source : N. A. Cherepkov and S. K. Semenov J. Phys. B **34**, L211(2001).

Figure (2-5 1) shows the calculated P_{perp} (equation 2-5 1) and P_{long} (equation 2-5 2) degrees of spin polarization of Xe $4p_{1/2}$ as a function of photon energy, the dipole matrix elements were first calculated in the Hartree-Fock approximation and then many-electron correlations in the Random Phase Approximation with Exchange RPAE have been included [2]. The second part of equation (2-5 2) is expressed in terms of the anisotropy parameter β and the non dipole anisotropy parameter γ calculated in the relativistic Independent Particle Approximation IPA calculation of Derevianko [23]. The two theories RPAE and IPA predict a resonance of $\sim 10\%$ in the degree of polarization near the ionization threshold as shown in figure (2-5 1).

The dipole polarization parameters and the angular asymmetry parameter β and the spin polarization parameters calculated [17] in RPAE for Xe $4p_{1/2}$ are shown in figure (2-5 2)

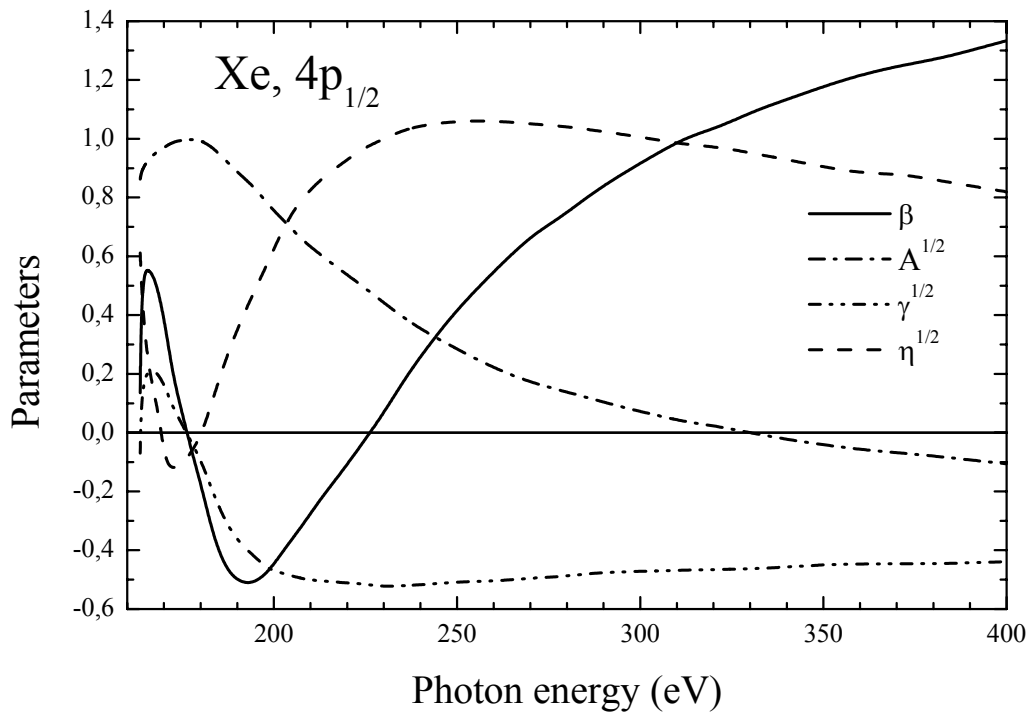


Figure (2-5 2). The angular asymmetry parameter β and the spin polarization parameters calculated in RPAE for Xe $4p_{1/2}$ source : source : N. A. Cherepkov and S. K. Semenov J. Phys. B **34**, L211(2001).

The spin polarization parameters γ^j and η^j go through zero near the ionization threshold. Due to this behaviour the contribution of the nondipole terms can be of the same magnitude as that of the dipole terms.

2.6 Nondipole spin polarization angular distribution near ionization threshold

The angular distribution of the spin polarization resulting from both dipole and nondipole contributions for $\kappa \perp \mathbf{s}$, $\mathbf{s} \perp \mathbf{k}$ and $(\kappa \cdot \mathbf{k}) = \cos(\theta)$ is :

$$P^{\pm 1}_{\perp}(\cos\theta) = \frac{(\eta^{1/2} \sin\theta \cos\theta - 3i/\sqrt{2} [B^{1/2}_{111} - \sqrt{7/2}\sqrt{2} B^{1/2}_{331}(5 \cos^2\theta - 1)] \sin\theta)}{(1 - 1/2\beta^{1/2}P_2(\cos\theta) + \sqrt{3}B^{1/2}_{110}\cos\theta + \sqrt{7}B^{1/2}_{330}P_3(\cos\theta))}. \quad (2-6 1)$$

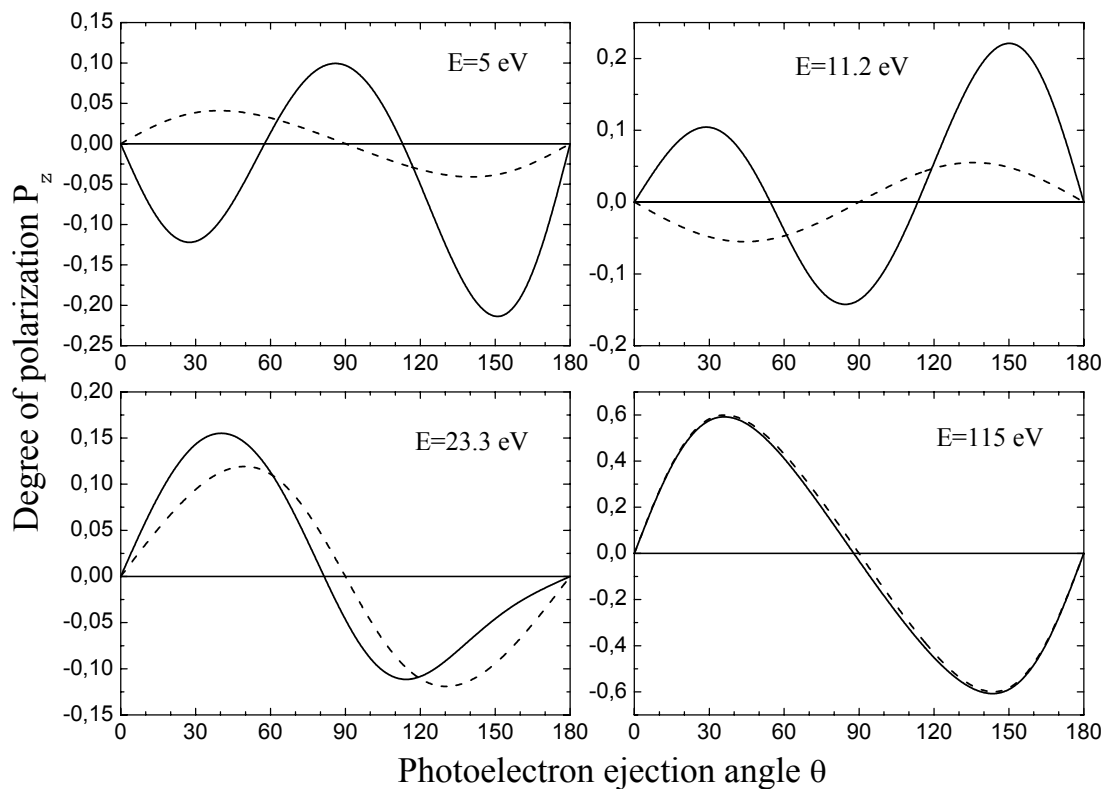


Figure (2-6 1). The angular dependence, θ is the angle between photoelectron direction κ and photon direction κ , of the degree of polarization of Xe $4p_{1/2}$ photoelectrons for circularly polarized light for several photoelectron energies calculated in RPAE in the pure electric-dipole approximation (dashed lines) and with nondipole corrections (solid lines) Source : N. A. Cherepkov and S. K. Semenov J. Phys. B **34**, L211(2001).

Figure(2-6 1) shows the dependence of the degree of polarization of Xe $4p_{1/2}$ photoelectrons for circularly polarized light calculated by equation (2-6 1) on the angle of electron ejection for several photoelectron energies calculated in the RPAE in the pure electric dipole approximation (dashed lines) and with nondipole approximation (solid line). We note that at low photoelectron energies the contribution of the electric-quadrupole corrections change the shape of the angular dependency. With increasing photon energy the contribution of the electric-quadrupole corrections becomes smaller.

Figure (2-6 2) shows the angular distribution of the Xe $4p$ photoelectrons at the expected resonance energy of 6.6 eV.

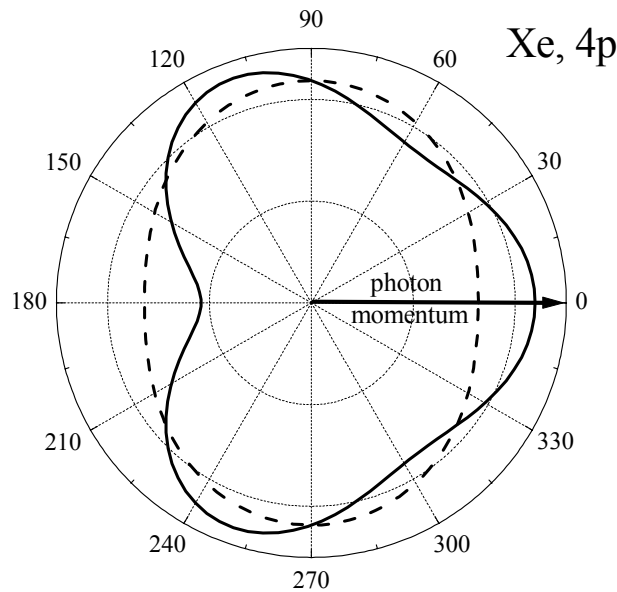


Figure (2-6 2). Angular distribution for the Xe 4p photoelectrons in RPAE for circularly polarized light at kinetic energy 6.8 eV in electric dipole approximation (dashed line) and with nondipole corrections(full curve). The direction of the photon momentum is at angle 0° .

2.7 The Quadrupole resonances in the Xe 4p photoionization¹

Cherepkov [18] accounted for the resonance in the degree of polarization near the ionization threshold for the quadrupole resonances in Xe 4p photoionizations in analogy with the well-known dipole resonance in Xe 4d photoionizations. There are two alternative ways to describe the giant dipole resonances; one in terms of the collective motion of all electrons in the atomic shell and the other in terms of a single electron excitation dependent effective potential [13]. This double-well effective potential has two contributions, the attractive Coulomb potential of the nucleus and other electrons and the repulsive ℓ centrifugal barrier. For sufficiently large orbital angular momentum ℓ when the electron is at a distance of the order of a_0 ; the Bohr radius, the sum of the two potential contributions can become positive. At large distances on the other hand the attractive Coulomb field dominates resulting in a negative effective potential. As a result we get this double-well potential:

$$V_{\text{eff}} = V_{\text{Coul}}(r) + \ell(\ell+1)(h/2\pi)^2 / 2mr^2. \quad (2-7 1)$$

In the ionization continuum, penetration of the Centrifugal barrier becomes possible and as the kinetic energy of the photoelectron reaches a certain resonance energy the spatial overlap

¹ This section is discussed in detail in N. A. Cherepkov and S. K. Semenov J. Phys. B **34** (2001) L211-L217.

of the wave function of both bound and continuum electrons will cause the rise in the photoionization cross section.

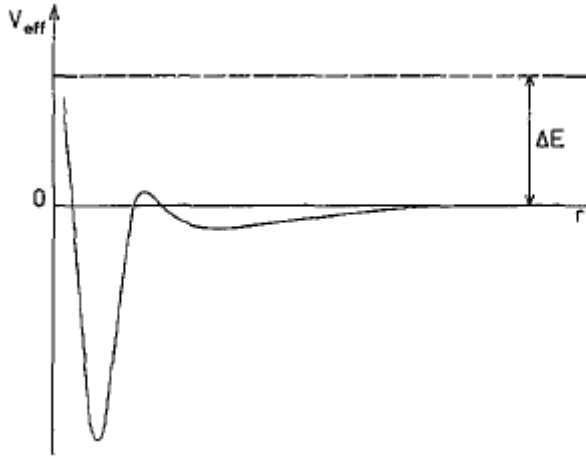


Figure (2-7 1). The double-well effective radial potential as seen by an emerging electron, against the radial distance r from the centre of the atomic core. The electron escapes from the atom with an angular momentum ℓ and a kinetic energy ΔE (not to a scale). Source C. Brechignac and J. P. Connerad *J. Phys. B: At. Mol. Opt. Phys.* **27**, 3795(1994)

In analogy to the giant resonances in the photoionization cross section due to the $nd \rightarrow \epsilon f$ dipole transitions of Xe which can be explained by virtue of the double-well shape of the effective potential, the quadrupole resonances in the Xe 4p photoionization can be explained with the $np \rightarrow \epsilon f$ transitions.

The matrix elements of the dipole and the quadrupole operators, see section 2.1, calculated in the Hartree-Fock approximation [18] are

$$\langle \epsilon \ell_1 | q | n \ell \rangle \sim f_q(\ell, \ell_1) \int dr r^4 R_{\epsilon \ell_1}(r) R_{n \ell}(r), \quad (2-7 2)$$

$$\langle \epsilon \ell_1 | d | n \ell \rangle \sim f_d(\ell, \ell_1) \int dr r^3 R_{\epsilon \ell_1}(r) R_{n \ell}(r), \quad (2-7 3)$$

where ϵ is the photoelectron energy, $f_q(\ell, \ell_1)$ and $f_d(\ell, \ell_1)$ are functions depending on the orbital angular momentum of both bound and continuum states, and R is the radial part of the electron wavefunction of bound and continuum states.

The asymptotic behaviour of the continuous spectrum wavefunction with orbital angular momentum ℓ is proportional to

$$R_{\epsilon \ell} \sim \sin(\pi r - \ell\pi/2 + 1/p \ln 2\pi r + \sigma_\ell + \delta_\ell), \quad (2-7 4)$$

where σ_ℓ is the Coulomb phase shift and δ_ℓ is an additional phase shift due to a short range part of the HF potential.

The dipole and quadrupole matrix elements calculated in RPAE for all allowed transitions from Xe 4p and 4d shells are shown in figure (2-7 2). The figure shows that *the dipole and quadrupole matrix elements for transitions to ϵf continuum states have a similar behaviour, viz. both are significantly larger in the extrema.*

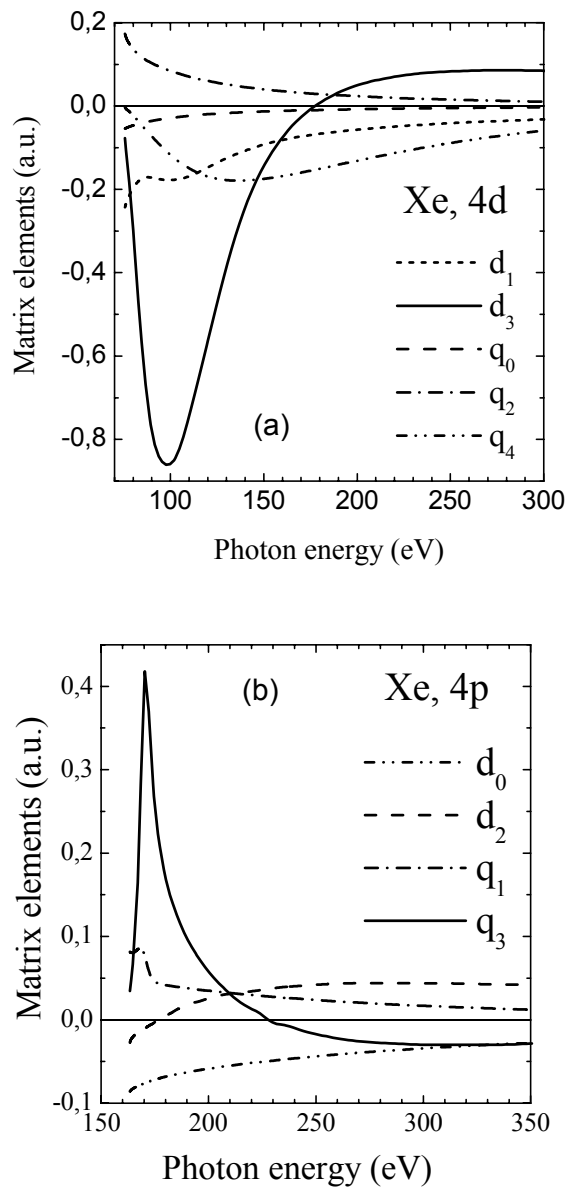


Figure (2-7 2). Dipole (a) and quadrupole (b) matrix elements calculated in RPAE. Source: N. A. Cherepkov and S. K. Semenov J. Phys. B **34**, L211 (2001).

The matrix elements and the corresponding short range phase shifts δ_3 for both transitions $4d \rightarrow \epsilon f$ and $4p \rightarrow \epsilon f$ are shown in figure (2-7 3). The phase shifts δ_3 in both transitions $4d \rightarrow \epsilon f$ and $4p \rightarrow \epsilon f$ are increasing by approximately π within the resonance. This behaviour shows the similarity of both transitions.

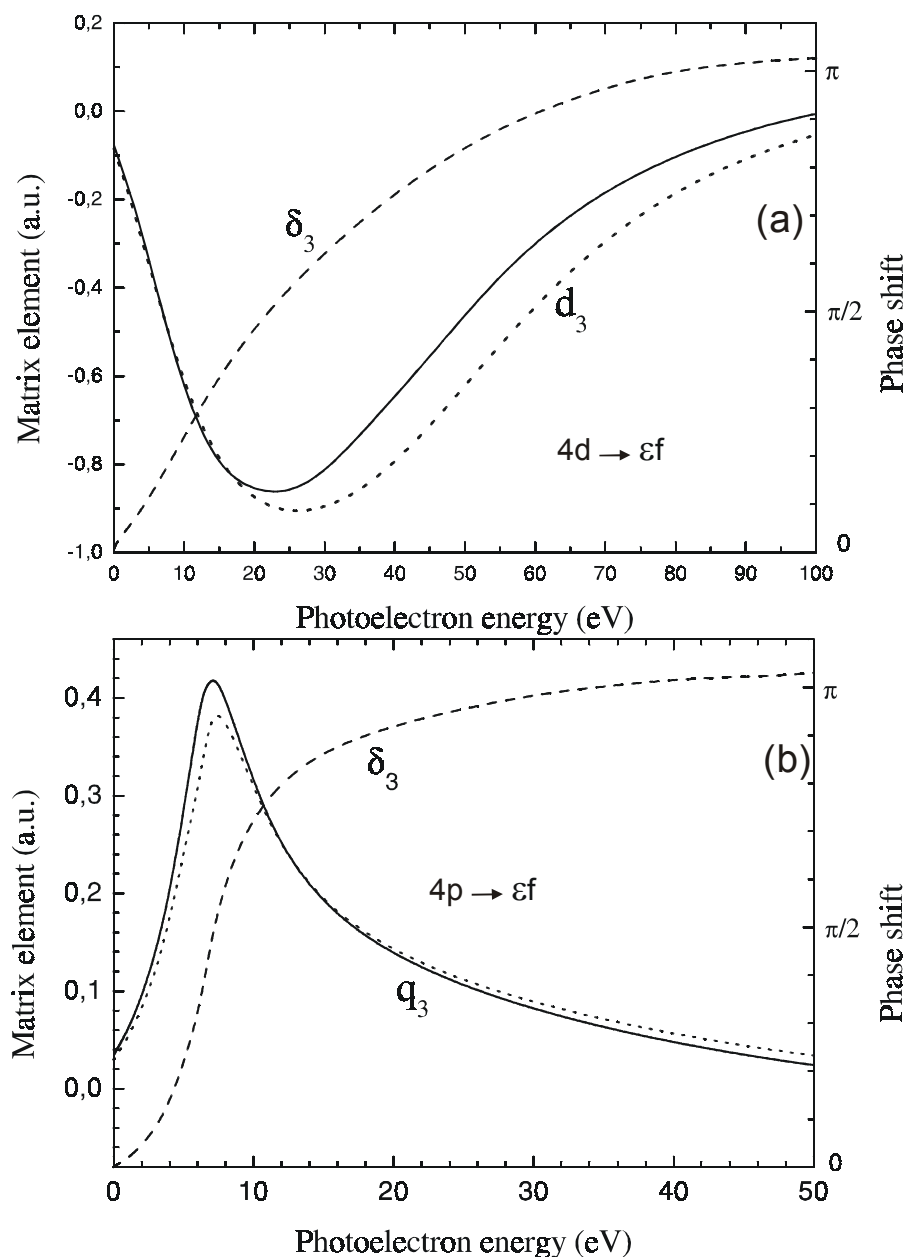


Figure (2-7 3). Dipole (a) and quadrupole (b) matrix elements and the corresponding short range phase shift. Source: N. A. Cherepkov and S. K. Semenov J. Phys. B **34**, L211 (2001).

The penetration of the wave function of the ϵf photoelectron at resonance energy into the inner well of the effective double-well potential which explain the resonance in photoionization closely above threshold is shown in figure (2-7 4).

In this figure (2-7 4) the calculations of the HF wave functions for the $4p \rightarrow \epsilon f$ quadrupole transition for several photoelectron energies and the wave function of the initial $4p$ state are shown. We see that at low energies the ϵf electrons are pushed out of the atom and there is very little overlapping of both bound and free electron wave functions. At the expected resonance energy of $\epsilon = 6.6$ eV the free electron wave functions have a great overlapping with the $4p$ wave function and the largest amplitude at the maximum of the $4p$ wave function. At higher energies there is still an overlap but with a clear oscillatory behaviour and the amplitude goes down, which leads together with the shift of the first node to a smaller distance and to a decrease of the quadrupole matrix element.

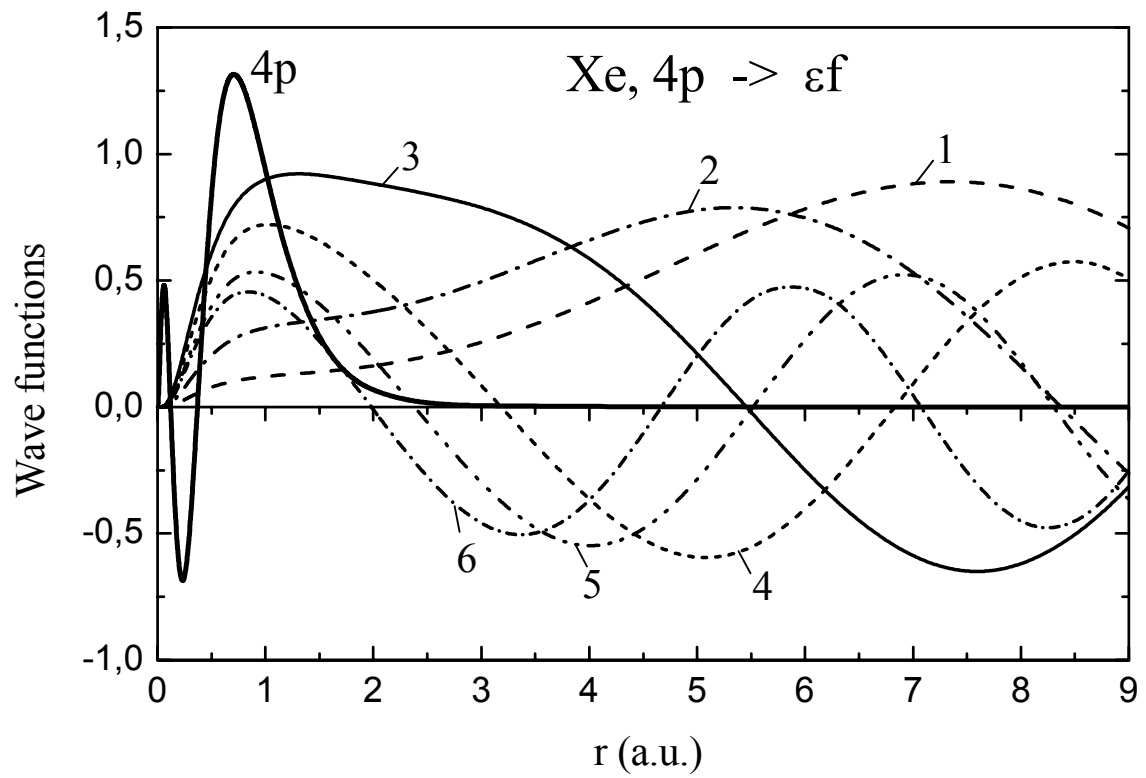


Figure (2-7 4). The wave functions of the 4p bound state and the ϵ f state at different energies. Source: N. A. Cherepkov and S. K. Semenov *J. Phys. B* **34**, L211 (2001).

3 Experimental Setup

3.1 Synchrotron Radiation

The synchrotron radiation is our tool to photoionize atoms in order to study their structure. This radiation is the only radiation which has a spectral range from infra red to hard X-rays. We can select the energy freely in this range and in the modern 3rd generation synchrotron rings like BESSY II we can get linearly or circularly polarized radiation with almost 100% degree of polarization.

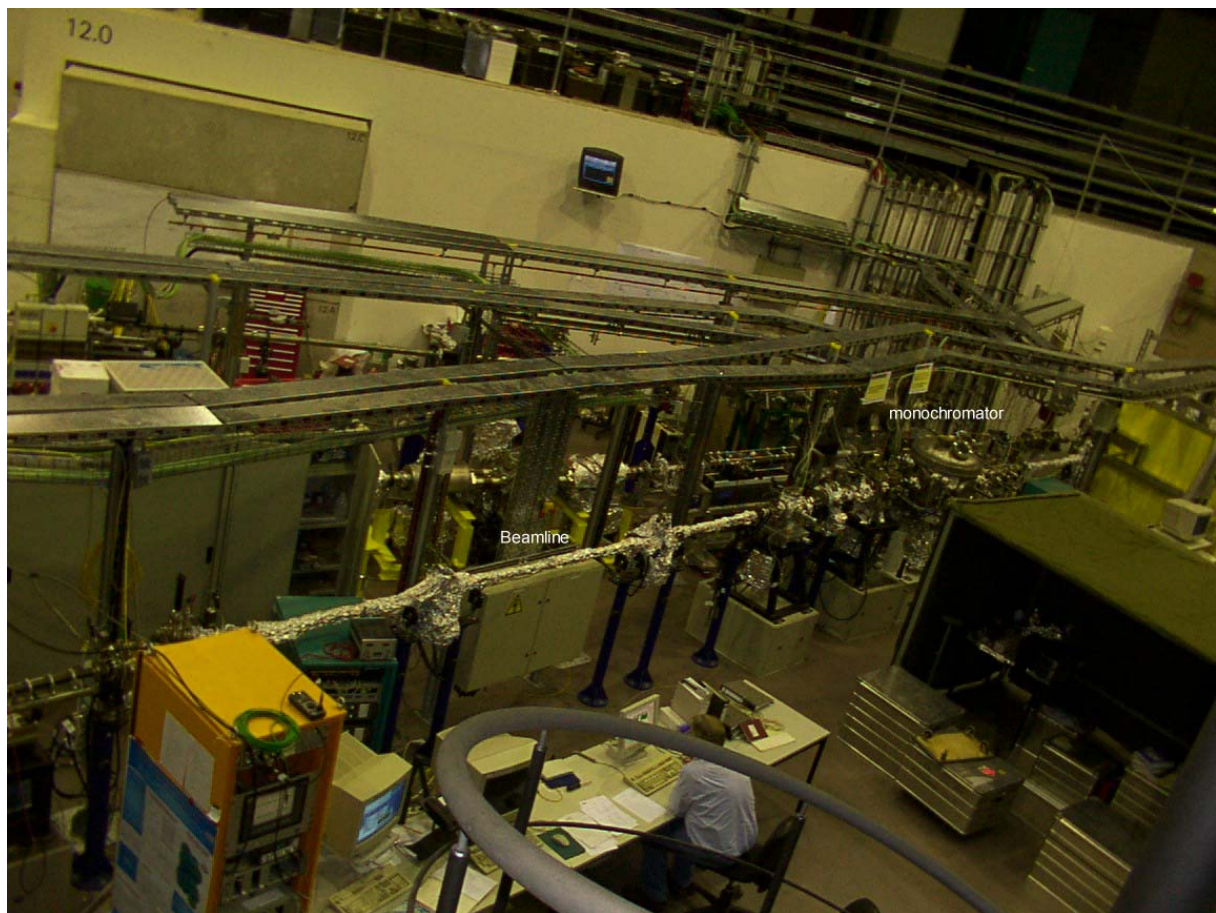


Figure (3-1 1). A panoramic photo of the beamline UE56 2.

Synchrotron Radiation¹ is produced when a relativistically charged particle experiences a radial acceleration as it travels around a circle. Bending magnets figure (3-1 2 a), Wigglers figure (3-1 2 b) and Undulators figure (3-1 2 c) are commonly used to produce Synchrotron Radiation.

¹ The discussion of Synchrotron Radiation here can be read in detail in David Attwood: Soft X-Rays and extreme Ultraviolet Radiation, Cambridge University Press 1999: Chapter 5

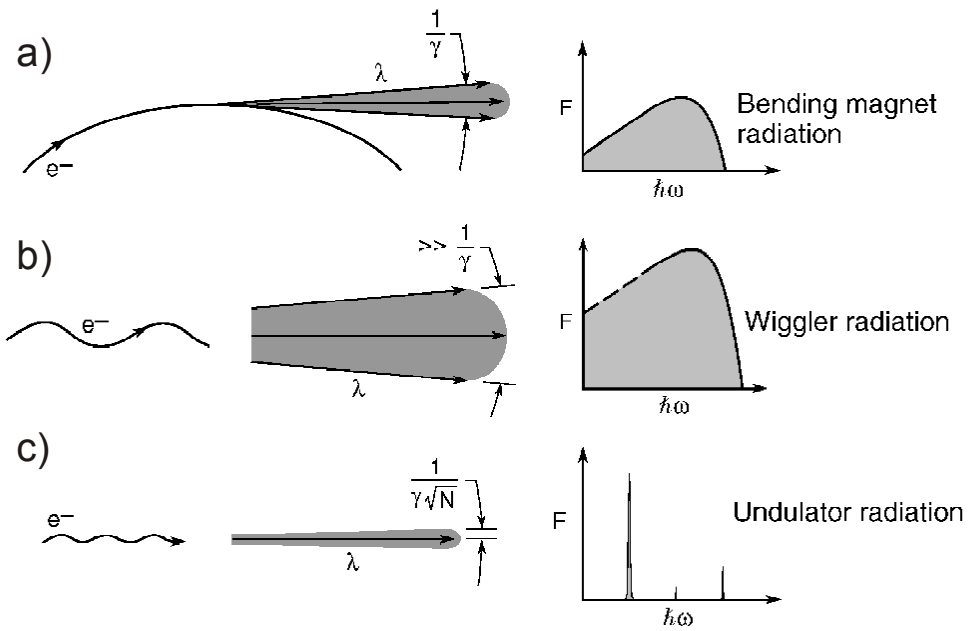


Figure (3-1 2). Synchrotron Radiation from a bending magnet(a), Wigglers (b) and Undulators (c) . Source : David Attwood Soft X-Rays and extreme Ultraviolet Radiation Cambridge University Press 1999.

The Bending magnets cause a single curved trajectory. The resulting synchrotron radiation is directed tangentially outward in a narrow radiation cone with a relatively wide spread of photon energy range. The emission angle is $1/\gamma$, where γ is the Lorentz factor [5].

$$\gamma \equiv (1 - v^2/c^2)^{-1/2} = E_e / m_0c^2, \quad (3-1 1)$$

v is the electron speed, E_e is the electron energy (1.7 GeV in BESSY II) and m_0c^2 is the rest energy of the electron.

The Undulators are periodic magnetic structures with relatively weak magnetic fields. The periodicity causes the electron to experience a harmonic oscillation with a small amplitude in the radial direction resulting in a narrow radiation cone, which is narrowed by a factor \sqrt{N} , where N is the number of magnetic periods. The spread of photon energy range is very narrow.

The Wigglers are a strong magnetic field version of undulators. As a result of this strong field, the harmonic oscillations are greater than the natural $(1/\gamma)$ radiation cone and hence the radiated power is larger.

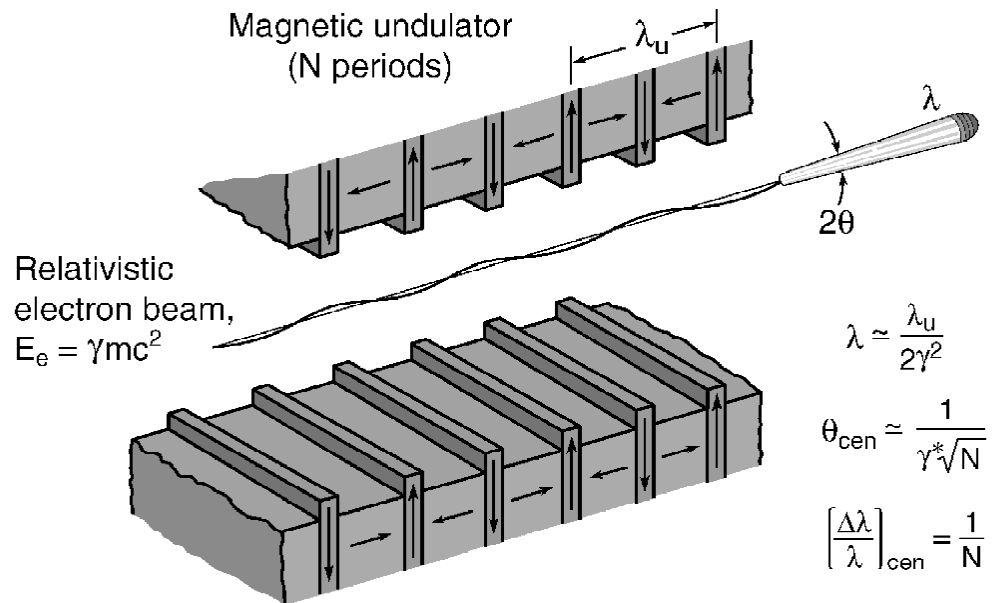


Figure (3-1 3). The electrons traverse a periodic magnet structure in an Undulator and generate a narrow cone undulator radiation. Source : David Attwood Soft X-Rays and extreme Ultraviolet Radiation, Cambridge University Press 1999.

An Undulator is a periodic magnetic structure with N periods of length λ_u , the transverse magnetic field produces an oscillatory path for the electrons; undulations, see Fig (3-1 3). In the inertial frame moving with the relativistic electron with constant speed v (not accelerated !), the electron *sees* a periodic magnet structure moving toward it with a Lorentz contracted period, λ'^1 given by :

$$\lambda' = \lambda_u / \gamma. \tag{3-1 2}$$

In the frame moving with the electron, the electron radiates as a classical radiating dipole. The frequency of the radiation in the laboratory frame is further reduced by *Doppler shifting*. The observed frequency on the axis ($\theta = 0$) will be for $\beta = v/c \approx 1$:

$$f = 2\gamma^2 c / \lambda_u, \tag{3-1 3}$$

and the corresponding wavelength λ on the axis ($\theta = 0$) will be :

$$\lambda = c / f = \lambda_u / 2\gamma^2 \tag{3-1 4}$$

At small angles off axis ($\theta \neq 0$) the observed wavelength λ will be :

$$\lambda = c / f = \lambda_u / 2\gamma^2 (1 + \gamma^2 \theta^2). \tag{3-1 5}$$

From both equations we see, taking the wavelength λ as on axis ($\theta = 0$), $\lambda = \lambda + \Delta\lambda$ as off axis at angle θ that:

¹ The primed frame of reference is the frame moving with the electron at the constant speed v. The unprimed frame of reference is the laboratory frame.

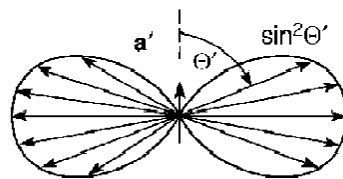
$$\Delta\lambda / \lambda = \gamma^2\theta^2. \quad (3-1 6)$$

The radiation pattern of the undulator, observed in the laboratory frame is relativistically contracted into a narrow radiation cone, its opening half-angle θ is:

$$\theta = 1 / 2\gamma. \quad (3-1 7)$$

For BESSY II: $\gamma = E_e / m_0c^2 = 1.7 \text{ GeV} / 0.511 \text{ MeV} = 3327 \Rightarrow$ the opening half-angle θ will be $\sim 150 \mu\text{rad}$.

Frame moving with electron



Laboratory frame of reference

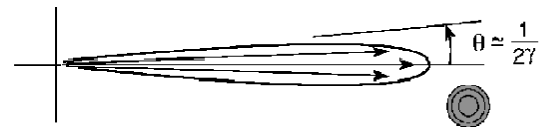


Figure (3-1 4). The radiation pattern of an oscillating relativistic charge in the frame of reference moving with the average electron speed and in the laboratory frame of reference. Source : David Attwood Soft X-Rays and extreme Ultraviolet Radiation, Cambridge University Press 1999.

Figure (3-1 4) shows the oscillating electron and its radiation pattern in the electron inertial frame of reference and the oscillating electron and its radiation pattern in the laboratory inertial frame of reference.

Undulator Bandwidth

The periodic array of magnets including N periods acts as a diffraction grating. The relative bandwidth is then given by the well-known diffraction-grating equation. For the first harmonic :

$$\Delta\lambda/\lambda = 1/N. \quad (3-1 8)$$

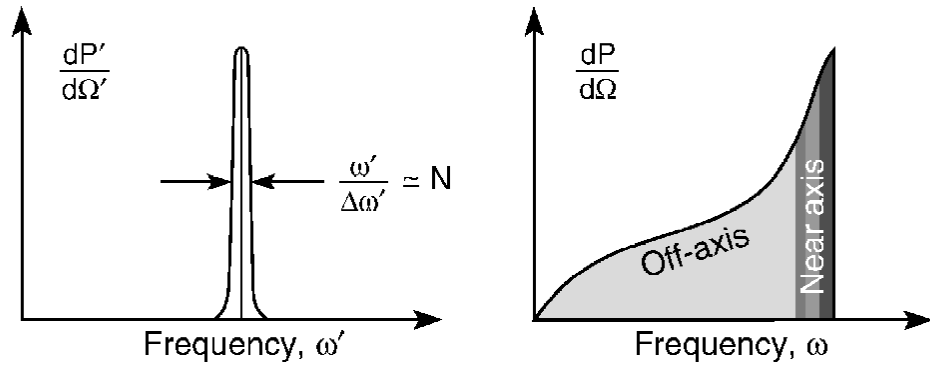


Figure (3-1 5). (left) The spectrum of radiation as seen in the electron frame with a narrow spectral width of order $1/N$, where N is the number of oscillation periods, (right) in the laboratory frame, the wavelengths are shorter, but the spectrum is broader due to off-axis Doppler effects Source : David Attwood Soft X-Rays and extreme Ultraviolet Radiation, Cambridge University Press 1999.

According to equation (3-1 6) and equation (3-1 8), at an angle θ with respect to the x-axis there is a relative shift in the radiated wavelength:

$$\Delta\lambda/\lambda = 1/N \approx \gamma^2\theta^2. \tag{3-1 9}$$

Thus, the maximum deviation (angular spread) is given by:

$$\theta \approx 1 / \gamma\sqrt{N}. \tag{3-1 10}$$

From equation (3-1 7) we see that within the cone of half angle $\theta \approx 1/2\gamma$ the relative spectral bandwidth is $\Delta\lambda/\lambda = \gamma^2(1/2\gamma)^2 = 1/4$; thus the cone of half-intensity and half-angle encloses a relative spectral bandwidth of about 25%. See figure (3-1 5).

For selecting a certain wavelength from the undulator synchrotron radiation, a monochromator is used as a narrow bandpass filter.

Figure (3-1 6) shows a grating monochromator used to filter undulator radiation to the spectral width $1/N$, and then the further cone narrowing to $1 / \gamma\sqrt{N}$, assuming the radiation from a single electron or a tightly constrained bunch of electrons.

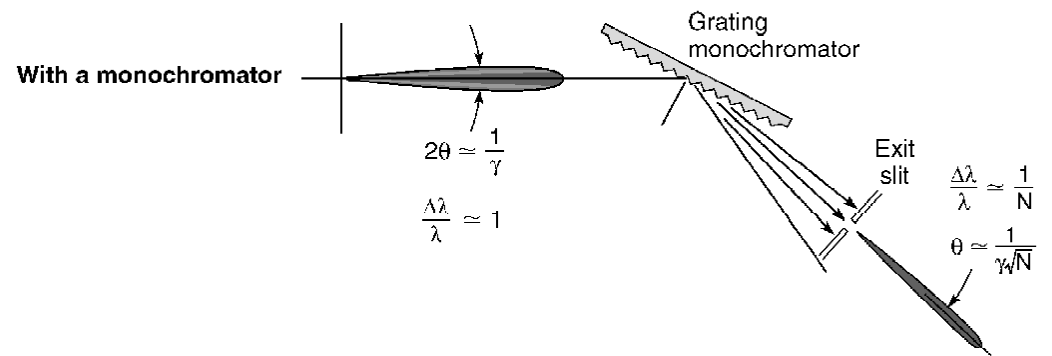


Figure (3-1 6). Illustration of a grating monochromator as used to filter undulator radiation to a natural spectral width $1/N$, and the concomitant cone narrowing to $1/\gamma\sqrt{N}$ when the electron beam is tightly constrained. Source : David Attwood Soft X-Rays and extreme Ultraviolet Radiation, Cambridge University Press 1999.

The UE56 double helical Undulator at BESSY II

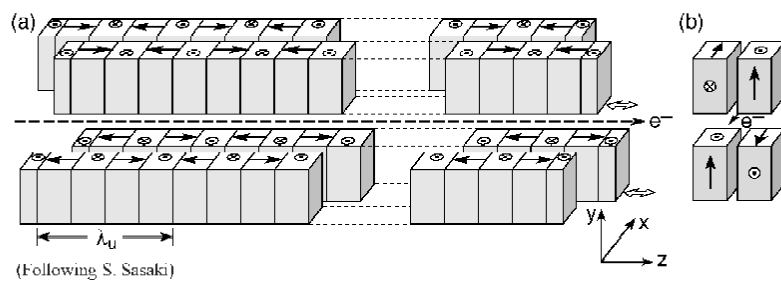
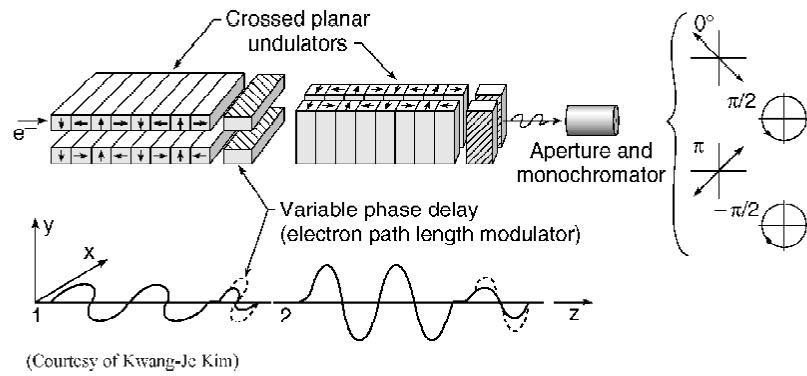


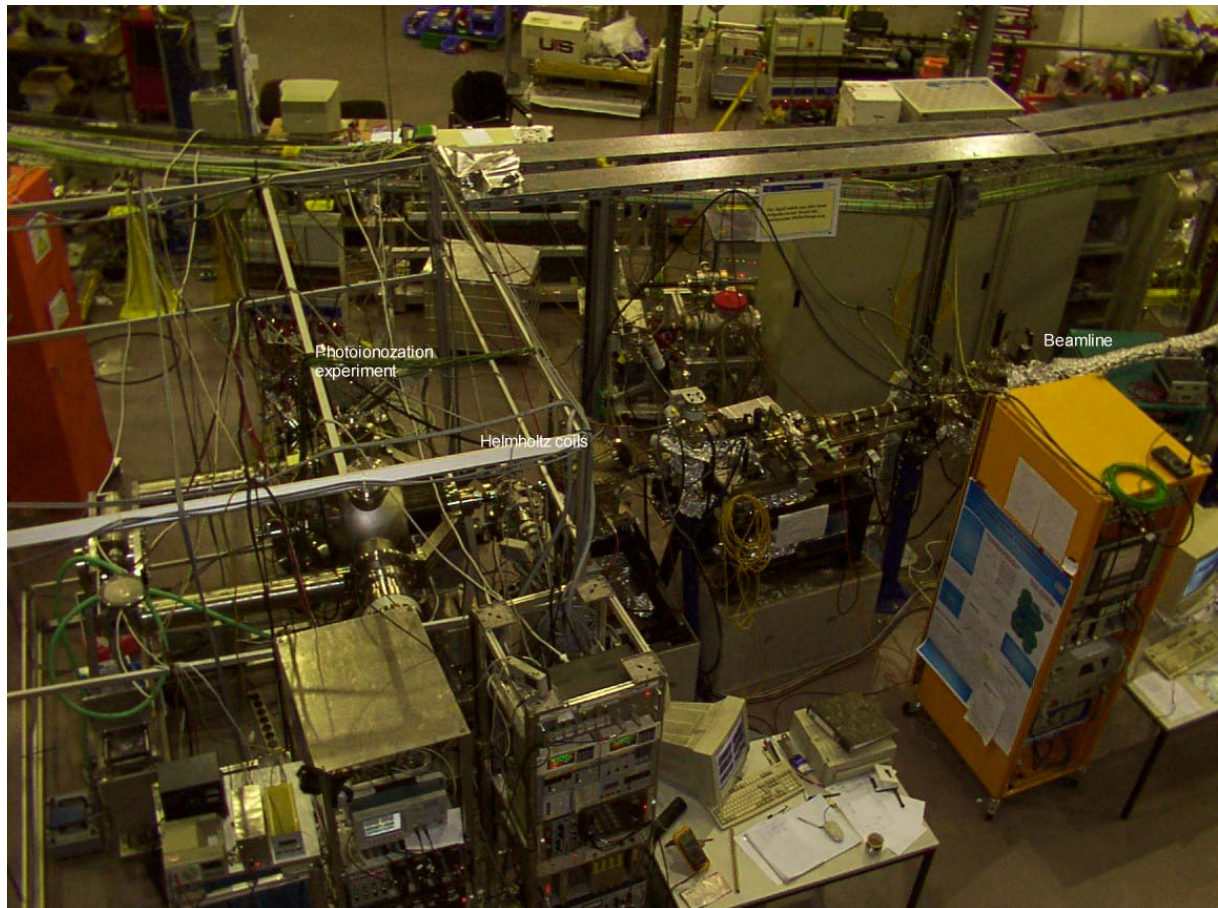
Figure (3-1 7). The production of linearly and circularly polarized light using undulators. Source : David Attwood Soft X-Rays and extreme Ultraviolet Radiation, Cambridge University Press 1999.

The UE56 Undulator of Sasaki type [60] emit simultaneously two angularly separated circularly polarized beams of opposite helicities. The Undulator provides circularly polarized radiation in the energy range 89 – 1328 eV. This Undulator has four magnet rows. The horizontal shifting of the magnet rows produces a helical field forcing the electrons on an elliptical or a circular path, which leads to the emission of elliptically polarized radiation. Indeed there are two Undulators, one called upstream and the other downstream. We have used both Undulators simultaneously using the beamline facility called Modulator to gain the maximum possible photon flux. This big photon flux compensates for the very low cross section for photoionization σ of Xe 4p photoelectrons.

The beamline has a plane grating monochromator. The degree of circular polarization is almost 100%.

3.2 Photoionization Apparatus

The experimental setup consists mainly of a new rotatable vacuum apparatus. The apparatus is suitable for angle resolved spectroscopy, it can be rotated about two orthogonal axes. It has been constructed from Schmidtke, for more details see the dissertation of Schmidtke [66].



Figure(3-2 1). The whole experimental setup, connected to the UE56 beamline.

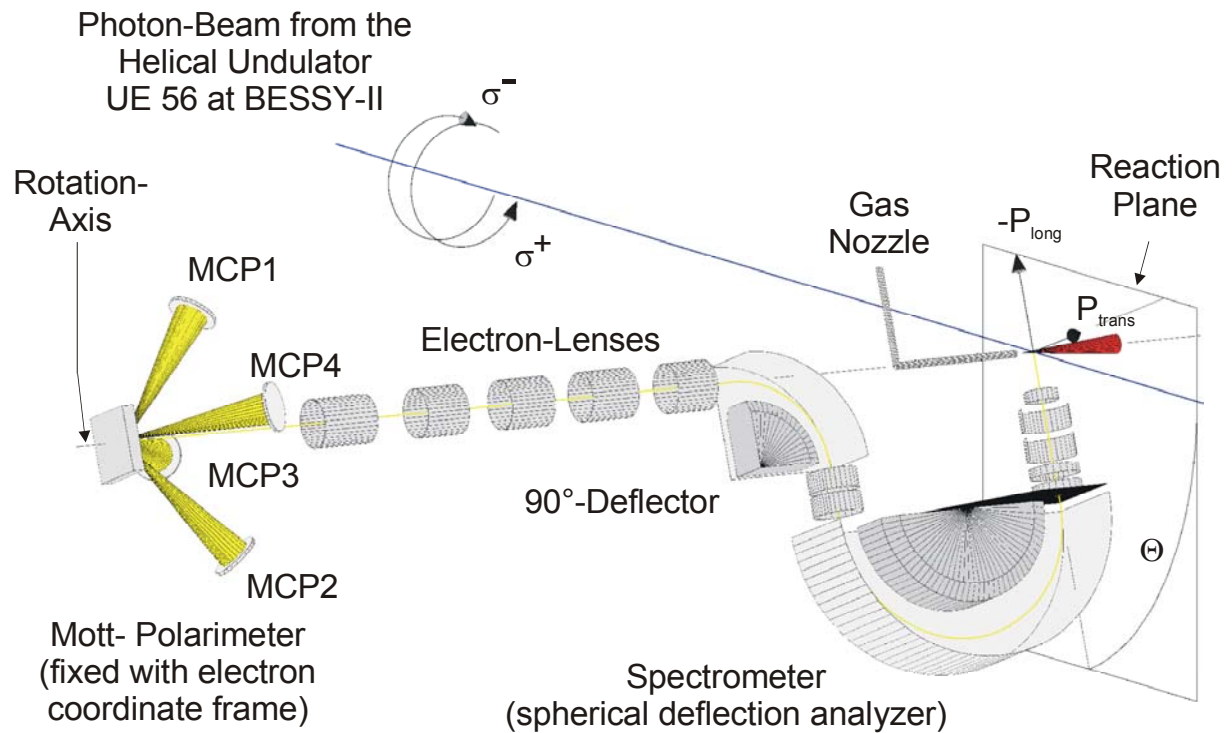


Figure (3-2 2). Diagram of the experimental setup shows the measurement geometry to measure two components of the spin polarization P_{long} along the direction of photoelectron momentum κ and P_{trans} along the direction of the photon momentum k .

The experimental setup is shown in figure (3-2 2). The synchrotron radiation crosses the rare gas atoms in the centre of the UHV chamber, the photoelectrons are monochromatized by a spherical deflection analyzer and then transported by the 90°-deflector and electron lens system to the Mott-Polarimeter to measure the electron spin polarization.

In this measurement geometry we measure the two spin components P_{long} and P_{trans} simultaneously.

3.2.1 Electron optics

It is necessary to extract the photoelectrons or the Auger electrons with selected energy from the region of atom-photon interaction and to transfer them to the Mott polarimeter to analyze their spin polarization. Figure (3-2 3) shows the electron optical system and the voltages for the different electrodes are listed in table (3-2 1).

There are many types of electron spectrometers, the conventional type of electron spectrometers is the ‘Spherical Deflection Analyzer’ [67] which we have used in this experiment.

The Spherical Deflection Analyzer used in the experiment has a simulated spherical field i.e the electric field is not due to full concentric hemispheres, but two cylindrical elements and two correcting electrodes create spherical equipotentials in the region of the electron beam trajectories [34], [53].

For the electrons in the central ray, the ratio of the spectrometer potential energy eU to its pass energy E_p is constant [67]

$$C = eU / E_p. \quad (3-2 1)$$

The radial field $E_r(r)$ is:

$$E_r(r) = (U/r^2)ab/(b-a), \quad (3-2 2)$$

where a and b are the inner and outer radii of the spectrometer hemispheres. Then the spectrometer constant C is:

$$C = (b/a) - (a/b) (= 0.956 \text{ in our case}).$$

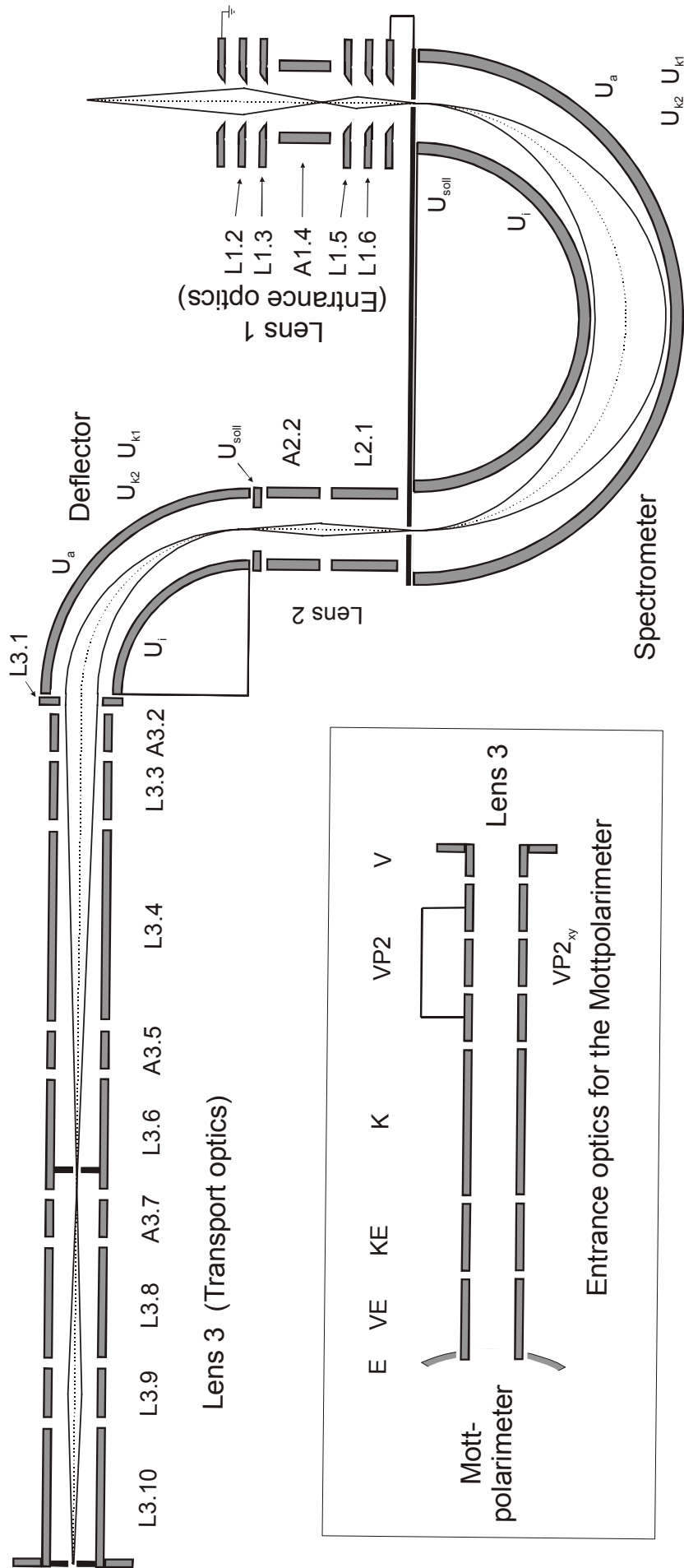
The inverse resolving power of the spectrometer is:

$$\Delta E/E \approx d / D + 0.5(\Delta\alpha)^2, \quad (3-2 3)$$

where d is the width of the exit slit =2.5 mm, $D = a + b = 150$ mm and $\Delta\alpha$ is the acceptance angle. $\Delta\alpha \approx \pm 4^\circ$.

Behind the spectrometer, the monochromatized electron beam is deflected by a 90° deflector to the rotation axis of the vacuum apparatus. Then the electrons are guided through the transport optics; lens 3, Fig (3-2 3), to the Mott polarimeter.

To trace one electron signal we utilized two channeltron electron detectors (see section 3.2.4) as monitors, the first is direct at the spectrometer exit, the second one at the exit of lens 3.



Figure(3-2 3). Trajectory of the photoelectrons from the photoionization region to the entrance of the Mott-polarimeter.

3.2.2 Voltage supply and control of the electron optics

The electron optics consist of about 40 electrodes which must be supplied with different values of high voltage. It is not practical to use passive voltage dividers to do this task. The voltage supply and control of the different electron optics electrodes is a computer-based system. The central component of this system, which was developed by Drescher [22] and further developed by Schmidtke [64], [66], is an active voltage divider. This active voltage divider has a fixed ohmic resistance and a high voltage MOSFET BFC60 transistor as a variable resistance, which is able to control high voltage outputs from -1000 V to 1000 V.

Table (3-2 1). The electrode voltages of the electron optics system from figure (3-2 3) for $E_{\text{kin}} = 35$ eV and pass energy $E_p = 70$ eV

Type	Electrode	Voltage (Volt)
Lens 1	L1.2	86
	L1.3	23
	A1.4	23
	L1.5	23
	L1.6	343
Spectrometer	U_{soll}	35
	U_i	76
	U_a	9.1
	U_k	22.5
Lens 2	L2.1	7
	L2.2	288
Deflector	U_{soll}	288
	U_i	477
	U_a	168.5
	U_k	230
Transport optics	L3.1	230
	A3.2	412
	L3.3	131
	L3.4	375
	L3.5	375
	L3.6	400
	L3.7	400
	L3.8	400
	L3.9	125
	L3.10	375

3.2.3 Mott polarimeter

The fact that Mott scattering is an elastic scattering depending on the spin of participating particles is used to measure the spin polarization of photoelectrons and Auger electrons. The Mott polarimeter and the underlying physics are discussed in T. J Gay et. al. [26] The physical principle of the Mott scattering is based on the **LS** coupling of high energetic electrons in the Coulomb field of a high-Z atomic nucleus and the resulting interaction energy; $V_{so} = (Ze^2/2m^2c^2r^3) \mathbf{L} \cdot \mathbf{S}$ results in a left/right scattering asymmetry¹. Here **L** is the orbital angular momentum of the electron, **S** is the electron's spin.

A high energetic electron with velocity **v** in electric field **E** of a high-Z nucleus sees in its rest frame a magnetic field **B** given by :

$$\mathbf{B} = -(1/c) \mathbf{v} \times \mathbf{E}, \quad (3-2 4),$$

$$\mathbf{E} = (Ze/r^3) \mathbf{r}, \quad (3-2 5)$$

(**r** is the nucleus-electron separation)

$$\mathbf{B} = (Ze/cr^3) \mathbf{r} \times \mathbf{v} = (Ze/mcr^3) \mathbf{L}. \quad (3-2 6)$$

($\mathbf{L} = m \mathbf{r} \times \mathbf{v}$)

The LS coupling interaction term is:

$$V_{so} = -\mu_s \mathbf{B}, \quad (3-2 7)$$

where

$$\mu_s = -(ge/2mc)\mathbf{S}, \quad (3-2 8)$$

μ_s is the magnetic moment of of the electron due to its spin, *g* is the spin *g* factor, the interaction term V_{so} is then given by :

$$V_{so} = (Ze^2/2m^2c^2r^3) \mathbf{L} \cdot \mathbf{S}. \quad (3-2 9)$$

The interaction term V_{so} adds to the Coulomb potential:

$$V_{total} = (1/4\pi\epsilon_0)Ze^2/r + (Ze^2/2m^2c^2r^3) \mathbf{L} \cdot \mathbf{S}. \quad (3-2 10)$$

Due to the *dot product* in the V_{so} term the only measured quantity is the transverse component of the electron spin, i.e we measure only the component of spin which is parallel (spin up !) or antiparallel (spin down !) to the orbital angular momentum of the electron **L**. **L** is always perpendicular to the scattering plane, so depending on the spin direction up or down, the interaction term V_{so} weakens or increases the total interaction potential. This causes a left/right scattering asymmetry in the scattering angles.

¹ Left right asymmetry means the measured spin component is vertical due to the **LS** coupling term. Hence vertical spin component is to be understood everywhere when left/right asymmetry is mentioned.

In other words the scattering potential V_{so} introduces a spin dependence in the scattering cross section $\sigma(\theta)$:

$$\sigma(\theta) = I(\theta) [1 + S_{\text{eff}}(\theta)\mathbf{P}\cdot\mathbf{n}], \quad (3-2 11)$$

$S(\theta)$ is the polarimeter efficiency known as the Sherman function [41]¹, $I(\theta)$ is the spin averaged scattered intensity, and \mathbf{P} is the incident electron spin polarization.

The unit vector \mathbf{n} is normal to the scattering plane:

$$\mathbf{n} \equiv \mathbf{k} \times \mathbf{k}' / (k \times k'), \quad (3-2 12)$$

where \mathbf{k} and \mathbf{k}' are the wave vectors of the incident and scattered electrons. The direction of \mathbf{n} , which is parallel to \mathbf{L} , determines whether scattering is to the left or to the right.

The Sherman function relates the scattering asymmetry and the spin polarization through:

$$\boxed{A(\theta) = P(\theta) S_{\text{eff}}(\theta)} \quad (3-2 13)$$

This relation is the basis of the Mott electron polarimetry.

The Mott polarimeter used in this experiment is a retarding potential Mott polarimeter. In this polarimeter, the incident electrons are accelerated by a radial electric field established between an inner and outer hemisphere. The inner hemisphere is operated at a high positive voltage = 45 kV, the outer electrode is held close to ground potential . Inside the inner hemisphere there is the scattering target which consists of ²³⁸U-lamella (around 4 x 6 mm²) . The scattered electrons leave the inner hemisphere through $\pm 120^\circ$ slits and are decelerated in the high voltage spherical field as they pass to the outer hemisphere, they are detected by two symmetrically positioned Multichannelplates (see next section) near ground potential. A major advantage of the retarding potential Mott polarimeter is that the inelastically scattered electrons will be discriminated in the retarding potential. Additionally the spherical field provides a two-dimensional focusing of the incident electron beam.

¹ See J. Kessler: Polarized Electrons Springer-Verlag 2nd Edition, page 218.

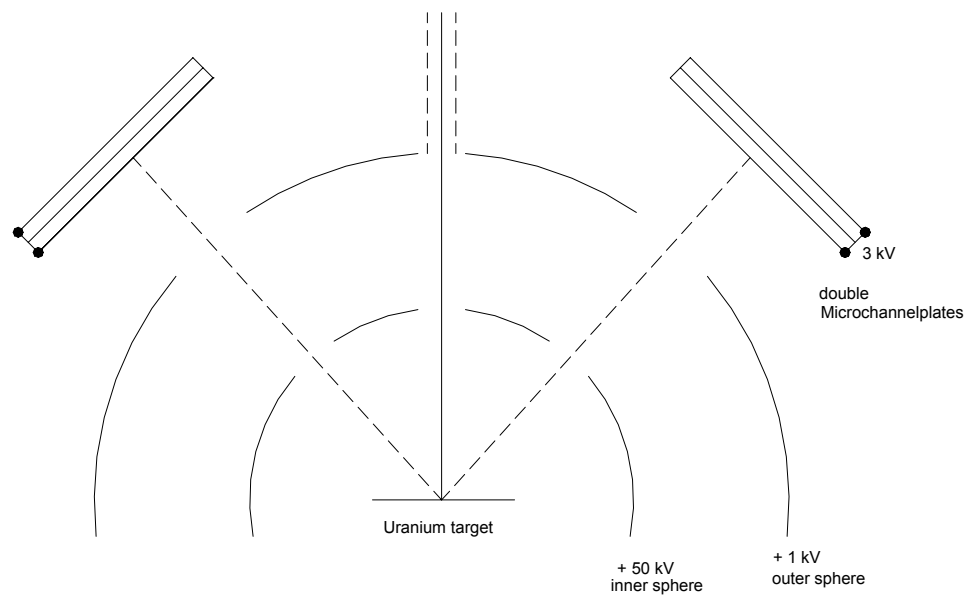


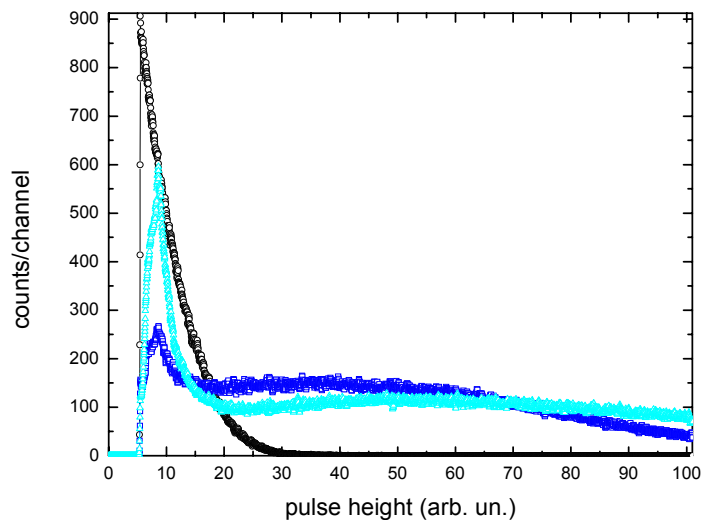
Figure (3-2 4). Schematic diagram of the main features of a spherical retarding potential Mott polarimeter. The major components are symmetrical about the vertical axis. The electrons are accelerated along this vertical axis, then the elastically scattered electrons at the Uranium target are decelerated in the spherical retarding field and detected by the double microchannelplates.

3.2.4 Channeltrons and microchannelplates as electron detectors

To detect the electrons scattered in the Mott polarimeter we used microchannelplates while Channeltrons were used for monitoring the monochromatized electrons behind the spectrometer.

Both channeltrons and microchannelplates [61]¹, MCP ($10^4 - 10^7$ microchannels) are principally channels which act as continuous dynode electron multipliers. When a positive voltage is applied at the channel exit, a single electron at the channel entrance has a certain probability for starting an avalanche of electrons. The electron avalanche leads to a charging of the inherent collector's capacitance C_D , and this process stop when the total charge Q of the avalanche has been deposited. The transit time that the electrons need for their passage through the channel is called the collection time t_{coll} . It is approximately 100 ns for a channeltron and 1 ns for a channelplate. Subsequent processes add more and more charges to the collector. Hence in order to allow the counting of single events, discharging of the collector through a load resistor R_a is necessary. The maximum amplitude U_{max} of the voltage pulse sent to the preamplifier is given by:

$$U_{max} = Q / C_D. \quad (3-2 14)$$



Figure(3-2 5). Distribution of the pulse height for one of the double microchannelplates of the Mott detector. The circles correspond to 700V per plate, the squares correspond to 780V per plate and the triangles correspond to 800V per plate

Figure (3-2 5) shows the distribution of the pulse height for one of the double microchannelplates we use in the Mott detector for three values of operating voltage per plate to find the optimal operation parameters of the microchannelplates.

¹ V. Schmidt Electron Spectroscopy of Atoms using Synchrotron Radiation, Cambridge University Press 1997, page 117.

3.2.5 Earth's magnetic field compensation

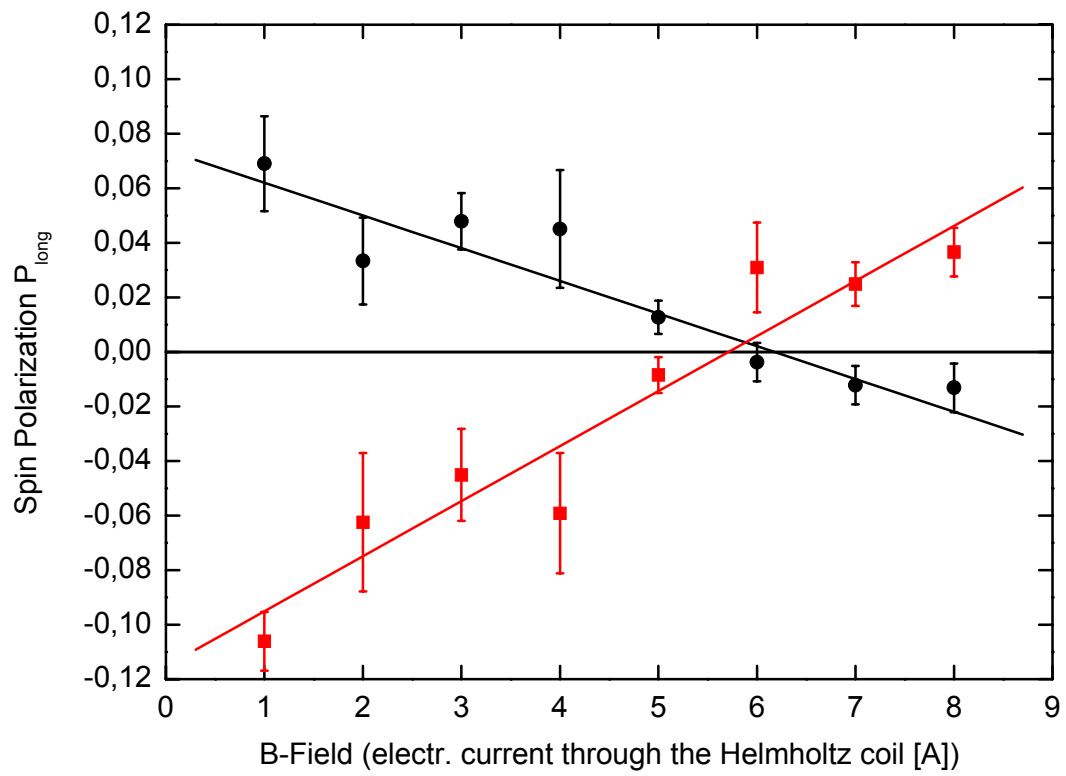
The earth's magnetic field is a disturbing factor in the electron spectroscopy especially due to the relatively long way from the photoionization region to the Mott polarimeter. The first effective procedure to shield the magnetic field is the use of a μ -metal shielding around the whole electron optical system. We use in addition Helmholtz coils to compensate actively the earth's magnetic field. Especially when the sensitive nondipole contributions to the electron spin polarization was measured, the residual magnetic fields was compensated with Helmholtz coils by referring to the Xe $4d_{3/2}$ photoelectron. The theory [18] expects these Xe $4d_{3/2}$ photoelectrons to have no nondipole contribution to the electron spin polarization. For each investigated kinetic energy of the Xe $4p$ photoelectrons, the Xe $4d$ photoelectrons of the same kinetic energy were observed by tuning the photon energy. Then the current through the Helmholtz coils was adjusted such that the component of the spin polarization P_{long} vanished, see figure (3-2 6).

The time required to transport the electrons from the photon-atom interaction region to the Mott polarimeter is about 200 ns. During this time the residual magnetic fields affects the electron spin polarization vector and rotates the dipole sensitive component P_{trans} . The angle ζ of rotation of the dipole sensitive component P_{trans} was estimated for our apparatus [66] to be about 6° ($\zeta = \arctan P_{\text{long}}/P_{\text{trans}}$).

The residual magnetic field B causes the precession of the spin polarization vector with the Larmor frequency :

$$v_L = (\mu_B/h) B, \quad (3-2 15)$$

where μ_B is the Bohr magneton. A residual magnetic field of ca. $6 \mu\text{T}$ causes the spin polarization vector to (rotate!) about B with the estimated angle of 6° . The residual magnetic field is compensated by the Helmholtz coils to suppress the rotation of the spin polarization vector.



Figure(3-2 6). The spin polarization component P_{long} of Xe $4d_{3/2}$ solid squares and Xe $4d_{5/2}$ solid circles for different values of the electric current in the Helmholtz coils determine the right B field at which $P_{\text{long}} = 0$.

4 Measurement of the Electron Spin Polarization

The measurement of the electron spin polarization goes back to a measurement of a left/right asymmetry resulting from the scattering of the high energetic electrons from a high Z target. In many cases the spectral line of interest (Signal) is not isolated, but has neighbouring lines (Spectral Background) which would be detected too. Then we will have to subtract the spectral background from the signal to get the net counts of the line of interest. We must subtract the additional electronic background, which is the intensity the detector measures independently of the real signal + spectral background. This can be due to apparatus asymmetry and due to the so called dark counts i.e. the counts not resulting from photoionization or the subsequent Auger process. To measure the asymmetry resulting from the signal and from the background (spectral and electronic) we perform the following routine:

- 1) The spectrometer is adjusted to the kinetic energy of the line of interest for a certain time interval of 10 seconds and the intensities in both left and right counters S_L and S_R are measured.
- 2) Then the spectrometer is adjusted to an arbitrary kinetic energy which is very far from the kinetic energy of our interest and we know with certainty that there are no electrons at that kinetic energy and measure both left and right intensities to determine the electronic background of the Signal for the same time interval of 10 seconds $B_{\text{electronic L}}(S)$ and $B_{\text{electronic R}}(S)$.
- 3) The measuring program then calculates the net counts: $N_L(S) = S_L - B_{\text{electronic L}}(S)$,
 $N_R(S) = S_R - B_{\text{electronic R}}(S)$.
- 4) Then the spectrometer is adjusted to the kinetic energy of the spectral background and both left and right detectors *measure* intensities for the same time interval of 10 seconds and determine the intensities $B_{\text{spectral L}}$ and $B_{\text{spectral R}}$.
- 5) We repeat step (2) in order to determine the electronic background of the spectral back-ground for the same time interval of 10 seconds $B_{\text{electronic L}}(B_{\text{spectral L}})$ and $B_{\text{electronic R}}(B_{\text{spectral R}})$.
- 6) As in steps (3) the measuring program then calculates the net counts:

$$N_L(B_{\text{spectral}}) = B_{\text{spectral L}} - B_{\text{electronic L}}(B_{\text{spectral L}}) \quad (4-1 \ 1),$$

$$N_R(B_{\text{spectral}}) = B_{\text{spectral R}} - B_{\text{electronic R}}(B_{\text{spectral R}}) \quad (4-1 \ 2).$$

- 7) The total measuring time until now is 40 seconds: 10 seconds for signal, 10 seconds for its electronic background, 10 seconds for the spectral background and 10 seconds for its electronic background. This 40 second sequence is then repeated 5 times ($5 \times 40 = 200$ seconds) to acquire more counts. The relative statistical error of the count N is $\sim (1/N)^{-1/2}$.

From this 200 second measuring time we get the four counts $N^+_L(S)$, $N^+_R(S)$, $N^+_L(B_{\text{spectral}})$ and $N^+_R(B_{\text{spectral}})$ for the positive light helicity. We then change the light helicity and do the same 200 second measuring sequence to obtain $N^-_L(S)$, $N^-_R(S)$, $N^-_L(B_{\text{spectral}})$ and $N^-_R(B_{\text{spectral}})$.

Now we can calculate the asymmetry of the signal A_S and the Asymmetry of the spectral background A_B from the 8 counts : $N^+_L(S)$, $N^-_L(S)$, ... which we have gained. Then the left and right scattered asymmetries are measured for both light helicities to get rid of the apparative asymmetry to the first order as will be discussed in chapter 5.

The Sherman function S_{eff} , is then measured as discussed below, to calculate the spin polarisation of both signal and spectral background. When the relative intensity of spectral background to signal is determined then the spin polarization of the net signal can be determined as will be discussed in chapter 5.

4.1 Determination of the Sherman function

To determine the Sherman function the asymmetry of well-known polarized electrons, the Xe $4d_{3/2}$ and Xe $4d_{5/2}$ [68], were measured.

line	polarization	statistical error	measured asymmetry	statistical error	Sherman function	statistical error
Xe $4d_{3/2}$	-0.83	0.09	-0.184	0.002	0.22	0.02
Xe $4d_{5/2}$	0.57	0.07	0.121	0.001	0.21	0.03

The weighted average of both values of the Sherman function is 0.22 ± 0.02 .

5 Discussion of the statistical and instrumental errors and the uncertainties in the measurements due to background subtraction

5.1 Errors resulting from instrumental asymmetries and external fields

As shown in sec. 3.2.3 an electron beam with spin polarization P normal to the scattering plane of a high Z target will result in a left-right asymmetry of the scattered intensities N_1 and N_2 through the same angle θ to the left and right.

$$A = (N_1 - N_2) / (N_1 + N_2), \quad (5-1 1)$$

where

$$P = A / S_{\text{eff}} \quad (5-1 2)$$

This left-right asymmetry can arise from a non spin polarized electron beam due to some apparatusive asymmetry A_f like an oblique incidence of the electron beam (the beam is not exactly normal to the target), which will cause one of the two detectors to see more electrons than the other detector.

If we can reverse the spin polarization of the incident beam without shifting the beam then, as is shown[27], the instrumental asymmetry can be eliminated to the first order .

The special helical undulator UE56 in the third generation storage ring (BESSY II) allows easy reverse of the transferred spin polarization of the incident beam without shifting the beam by reversing the light helicity.

If we denote the efficiencies of the left and the right detectors by L and R and we assume that one detector will see more electrons than the other due to oblique incidence of the electron beam, then we will have a resulting apparatusive asymmetry A_f :

$$N_1^+ = L(1+P S_{\text{eff}})(1+A_f), \quad (5-1 3)$$

$$N_1^- = L(1-P S_{\text{eff}})(1+A_f) , \quad (5-1 4)$$

$$N_2^+ = R(1-P S_{\text{eff}})(1-A_f) , \quad (5-1 5)$$

and

$$N_2^- = R(1+P S_{\text{eff}})(1-A_f). \quad (5-1 6)$$

The superscripts $+$ and $-$ in N_1^+ , N_1^- denote the counts in left detector for positive and negative light helicities respectively.

The symmetry of the last four equations arises from the geometrical symmetry of the arrangement; when one detector sees more electrons due to oblique incidence, the other detector will see less electrons, the same arises when we reverse the spin polarization of incident electrons through change of light helicity.

Now when we substitute

$$N_1^{\text{new}} = (N_1^+ N_2^-)^{1/2}, \quad (5-1 7)$$

and

$$N_2^{\text{new}} = (N_2^+ N_1^-)^{1/2}, \quad (5-1 8)$$

in the equation (5-1 1)

we get

$$\boxed{A = (N_1^{\text{new}} - N_2^{\text{new}}) / (N_1^{\text{new}} + N_2^{\text{new}}) = P S_{\text{eff}}} \quad (5-1 9)$$

The apparatus asymmetry and the different counter efficiencies are then eliminated to the first order through the substitutions (5-1 7) and (5-1 8).

5.2 Calculation of the Error in the Asymmetry

To calculate the error in the asymmetry $A(N_i^\lambda)$ equation (5-1 1) resulting from the statistical uncertainties in measuring the different scattered intensities in the left and the right detectors for both light helicities N_i^λ , $i=1, 2$ and $\lambda = +, -$. The error in the asymmetry $\delta A(N_i^\lambda)$ then is:

$$\delta A(N_i^\lambda) = [\sum_{i,\lambda} (\partial A / \partial N_i^\lambda)^2 (\delta N_i^\lambda)^2]^{1/2} \quad (5-2- 1)$$

where we have used the known formula for the combination of errors for the function $A(N_i^\lambda)$ [70]¹.

To simplify the calculation of δA we write equation (5-1 9) in the form:

$$A = (q - 1) / (q + 1), \quad (5-2- 2)$$

where

$$q = (N_1^+ N_2^- / N_2^+ N_1^-)^{1/2}, \quad (5-2- 3)$$

and the error in A is

$$\delta A = [(\partial A / \partial q)^2 (\delta q)^2]^{1/2}, \quad (5-2 4)$$

$$\delta A = q / (q+1)^2 [\sum_{i,\lambda} 1 / N_i^\lambda]^{1/2}, \quad (5-2 5)$$

where we have used:

$$\delta q = [\sum_{i,\lambda} (\partial q / \partial N_i^\lambda)^2 (\delta N_i^\lambda)^2]^{1/2} = [(q/2)^2 \sum_{i,\lambda} 1 / N_i^\lambda]^{1/2}, \quad (5-2 6)$$

and the fact that

$$(\delta N_i^\lambda)^2 = [(N_i^\lambda)^{1/2}]^2 = N_i^\lambda. \quad (5-2 7)$$

That is the Poisson distribution applied to the numbers N_i^λ 's [70]².

At BESSY II we have usually 12 hours a day to measure spin polarization, this period is mostly divided into two intervals separated by an electron injection in the storage ring.

As we have shown in section 4, we need approx. 2×200 sec + (ca. 120 sec for light helicity change through the UE56 Undulator) i.e. ca. 8 minutes to measure one asymmetry point.

When we have low counts N_i^λ as usually the case due to:

- the low density of the gas phase target and
- the loss of ca. a factor 1000 of the signal intensity on account of the scattering and the retarding in the high voltage field in the Mott detector.

¹ G. L. Squires: Practical Physics - revised edition 1976 McGraw-Hill page 36

² G. L. Squires: Practical Physics - revised edition 1976 McGraw-Hill pages 200 – 204

- the storage ring current i.e. the number of emitting electrons decreases exponentially with time.

On account of equation (5-2 5) the uncertainty in the asymmetry δA is $\sim 1/\sqrt{N_i}^\lambda$. As a result the greater the N_i^λ , the more precise is the asymmetry measurement.

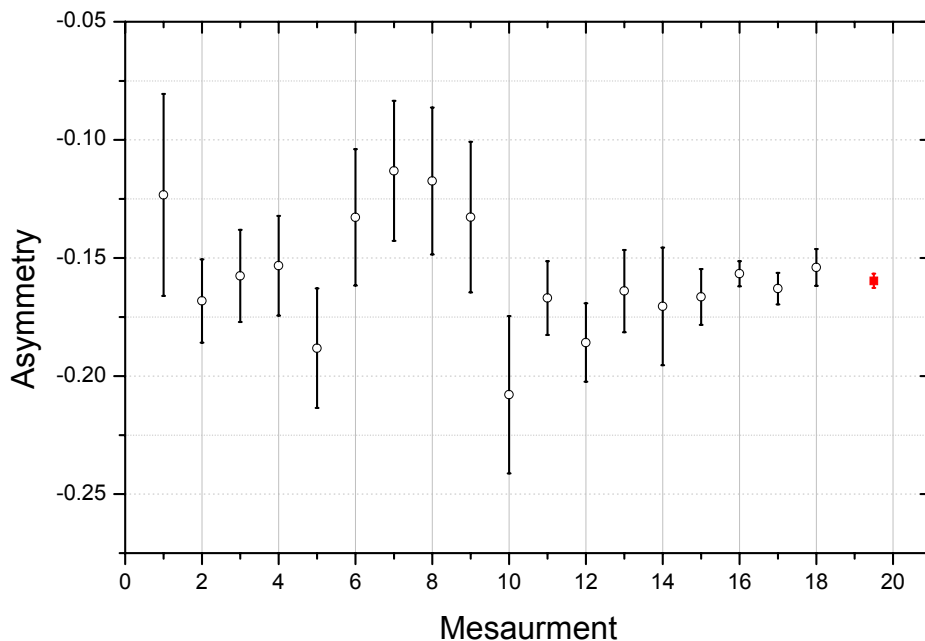
Accordingly we repeat the above described 8 minute routine as often as possible to improve the statistical significance. Then there will be n independent asymmetry measurements. These independent Asymmetry measurements are summed together by weighting every individual asymmetry measurement A_i with the square of $(1/\delta A_i)$ to get their weighted average A_w [70]¹

$$A_w = \sum_k w_k A_k / \sum_k w_k, \quad (5-2 8)$$

where $w_k = 1 / \delta A^2,$ (5-2 9)

and $\delta A_w = 1/ \sum_k (1/\delta A_k^2).$ (5-2 10)

The individual A_i values with a great error δA will have, through the value of the weight $w_i = 1/\delta A^2$, a lower contribution to the weighted average A_w while the A_i values with a small error δA will have a greater contribution to A_w .

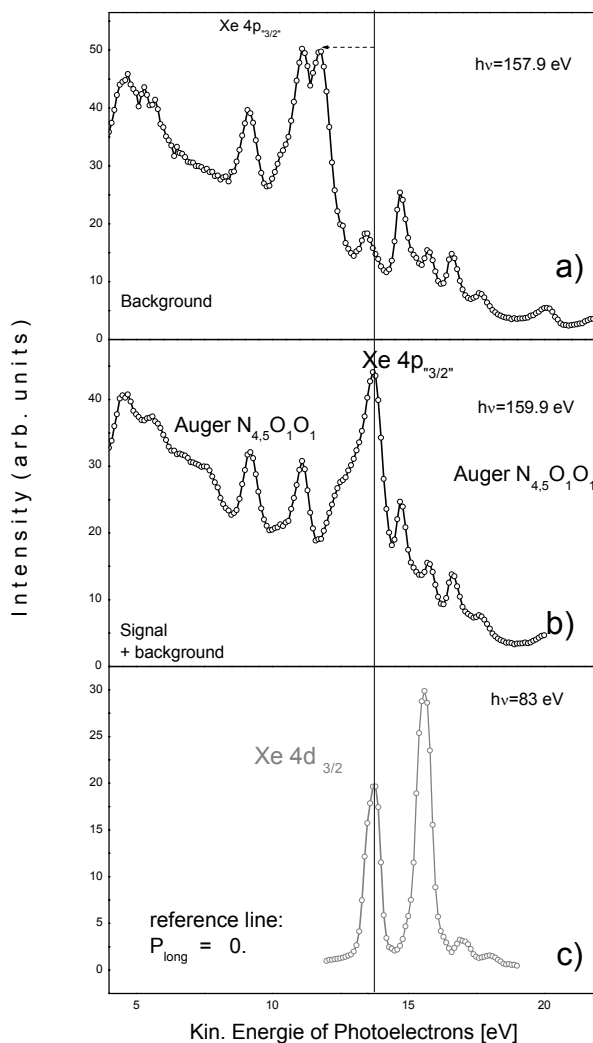


Figure(5-2 1). An example of an asymmetry measurement, the 18 open circles denoting individual measurements are summed up according to equation (5-2 8) to get the weighted average; the solid square.

¹ G. L. Squires: Practical Physics - revised edition 1976 McGraw-Hill page 41

5.3 Subtraction of spectral background in Xe 4p

The Xe 4p photoelectron line near ionization threshold is experimentally not easy to measure not only due to the low cross section for photoionization, but also the NOO Auger lines, multiple ionization, and cascade processes create an unavoidable spectral background. For the spectral background subtraction two different approaches were used. In May 2001 the spin polarization was measured at the Xe 4p peak and at 1-2 eV higher kinetic energies; and in October 2001 the photon energy was instead lowered by 2 eV to access the spectral background at constant kinetic energy; figure(5-3 1) (a) and (b). As discussed in section 3.2.5 the Helmholtz magnetic field has always been tuned such that the component of spin polarization of Xe 4d_{3/2} vanishes to minimize the effect of the external B-fields on the sensitive P_{long} spin component. The spin polarization of the spectral background has a vanishing component P_{long} according to the theoretical expectation, and the Auger and higher process have extremely small nondipole effects.



Figure(5-3 1). Subtraction of spectral background is accomplished by shifting the Xe 4p_{3/2} photoline (b) to lower kinetic energies (a) while keeping the spectrometer bandpass fixed. (c) The Xe-4d_{3/2} photoline is shifted to the same energetic position for control of the residual magnetic field.(see section 3.2.5)

5.3.1 Determination of the spin polarization of the net Signal

To get the spin polarization of the net signal $N = S - B$ from the measured spin polarization of both signal S and spectral background B ;

The net signal N_i is denoted by:

$$N_i = S_i - B_i, \quad i=1,2 \quad (5-3 1)$$

$$S := S_1+S_2, \quad B:=B_1+B_2. \quad (5-3 2)$$

The asymmetry of the net signal A_N is:

$$A_N = (N_1-N_2)/(N_1+N_2) = [(S_1-S_2)-(B_1-B_2)]/[(S_1+S_2)-(B_1+B_2)] \quad (5-3 3)$$

Dividing both numerator and denominator by S , we get:

$$A_N = (1 - B/S)^{-1} [A_S - (B/S)A_B], \quad (5-3 4)$$

where A_S and A_B are the Asymmetries of the signal and the spectral background which we have measured as explained above.

When there is more than one spectral background, then equation (5-3 4) can be generalised as follows :

$$N = S - \sum_i B_i, \quad (5-3 5)$$

$$N' = S' - \sum_i B'_i. \quad (5-3 6)$$

Where N and N' are the left and right scattered net intensities, B_i is the individual spectral background and

$$S^t := S+S', \quad B_i^t := B_i+B'_i, \quad (5-3 7)$$

then the asymmetry of the net signal A_N is:

$$A_N = (1 - \sum_i B_i^t / S^t)^{-1} [A_S - \sum_i B_i^t / S^t A_{Bi}], \quad (5-3 8)$$

A_{Bi} is the individual asymmetry of the individual spectral background.

When the relative intensity ratio of background/signal B/S or B_i^t / S^t is known, then the asymmetry of the net signal A_N . can be calculated.

To determine the relative intensity ratio of background/signal B/S we fit the spectrum using a Voigt function. The Voigt function is a convolution of the natural Lorentz line profile with the Gauss profile of the detector [33] . The intensity of the spectral background electrons which the spectrometer sees when its kinetic energy is at the signal position, is the area of the product of the Voigt profile of the spectral background line and the spectrometer function which is a gauss function at the kinetic energy of the signal.

5.4 Subtraction of Background due to neighbouring resonant Kr $3d^{-1}_{3/2}$ transitions

The lower part of figure (5-4 1) shows the ‘hv’- electron spectra of resonantly excited Kr $3d$, where the electron spectrometer was set at a constant kinetic energy [at 43.2 eV in (a) and at 44.3 eV in (b) as shown in the upper part] and the photon energy was scanned to find the exact resonance energy. The hv-spectra were taken at different slit widths of the beam-line exit to determine the appropriate resolution; the narrower the slit the better is the resolution.

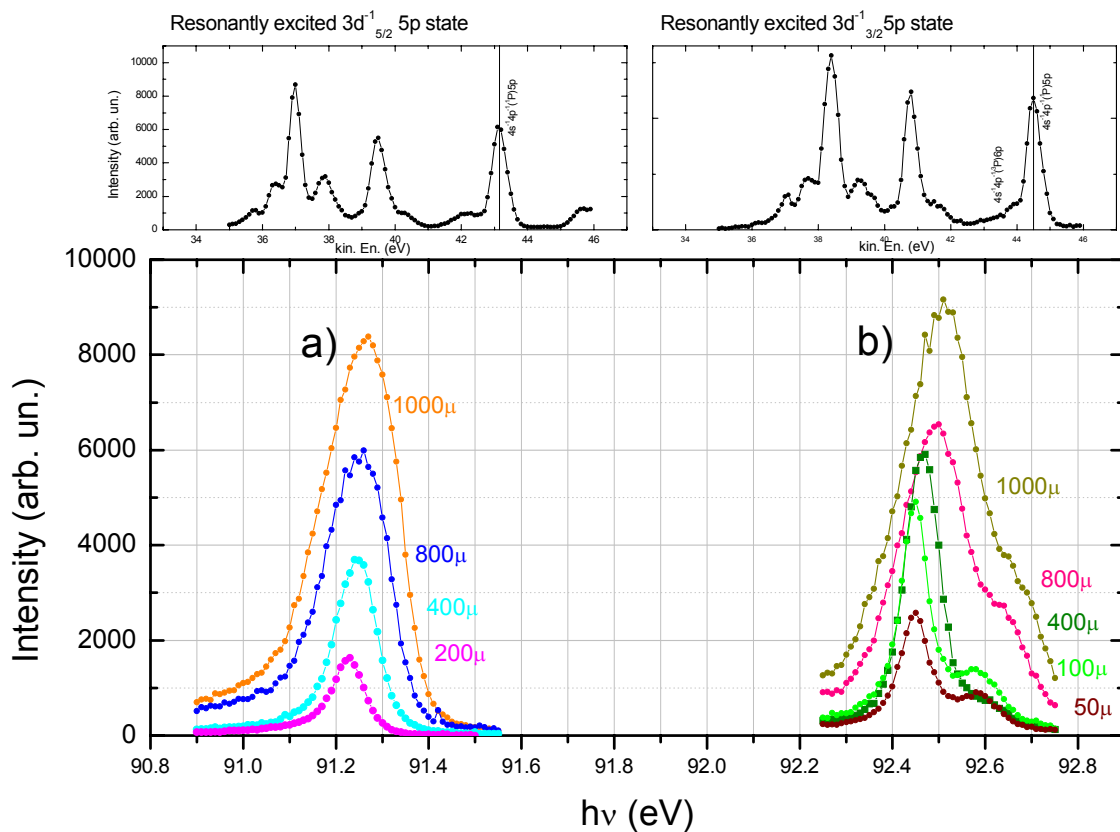


Figure (5-4 1). The hv spectra of the resonantly excited Kr $3d^{-1}_{5/2}5p$ and Kr $3d^{-1}_{3/2}5p$ spectra

When the spin polarization of the Kr $3d_{3/2}^{-1}5p \rightarrow 4s^{-1}4p^{-1}5,6p$ resonant Auger electrons is measured where the resonance takes place at photon energy 92.245 eV the electrons of the Kr $3d_{5/2} 6p^{-1} \rightarrow 4s^{-1}4p^{-1}6p$ resonant Auger electrons have to be measured because their resonance takes place at the very near photon energy 92.560 eV [45].

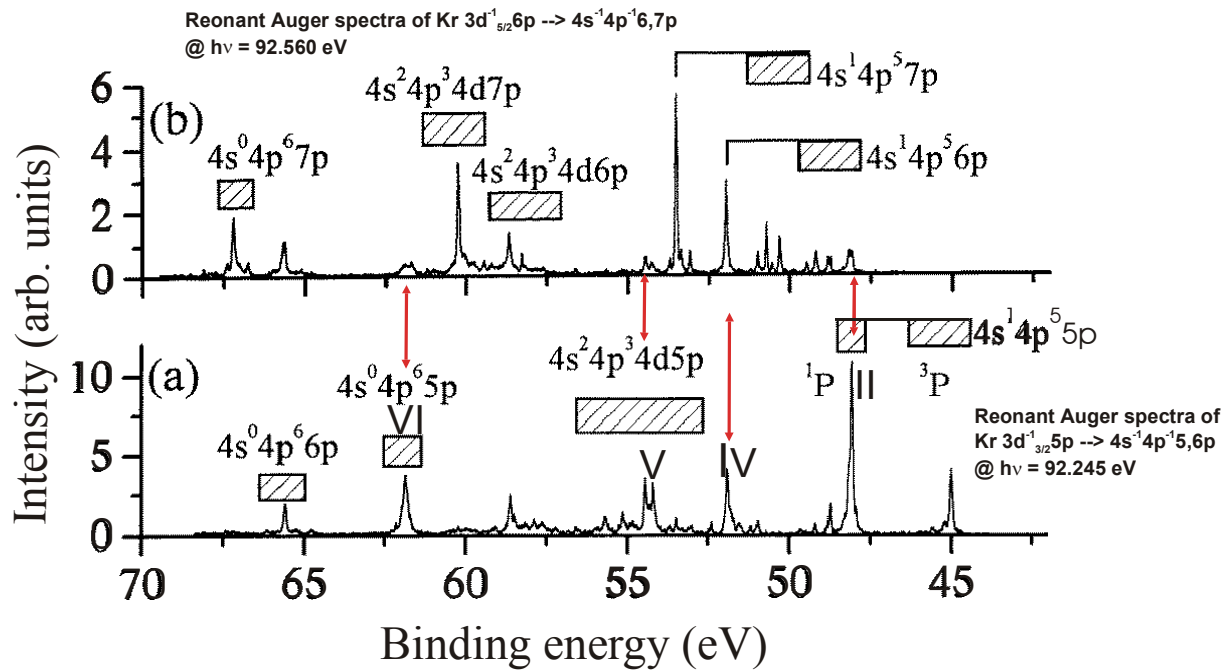


Figure (5-4 2) left (a): the Kr $3d_{3/2}^{-1}5p \rightarrow 4s^{-1}4p^{-1}mp$ resonant Auger spectrum taken at $h\nu=92.425$ eV; right (b): the Kr $3d_{5/2}^{-1}6p \rightarrow 4s^{-1}4p^{-1}mp$ resonant Auger spectrum taken at $h\nu=92.560$ eV. The roman numerrals correspond to Kitajima et al [45]. Source: J. Mursu, J Jauhainen, H Aksela and S Aksela J. Phys. B: At. Mol. Opt. Phys. **31** 1973 (1998).

Figure (5-4 2);left (a) and right(a) shows that the Kr $3d_{5/2}^{-1}6p \rightarrow 4s^{-1}4p^{-1}6p$ resonant Auger transition takes place almost at the same excitation energy as the Kr $3d_{3/2}^{-1}5p \rightarrow 4s^{-1}4p^{-1}5p$ resonant Auger transition. This situation is confirmed by our measurement, see figure(5-4 3).

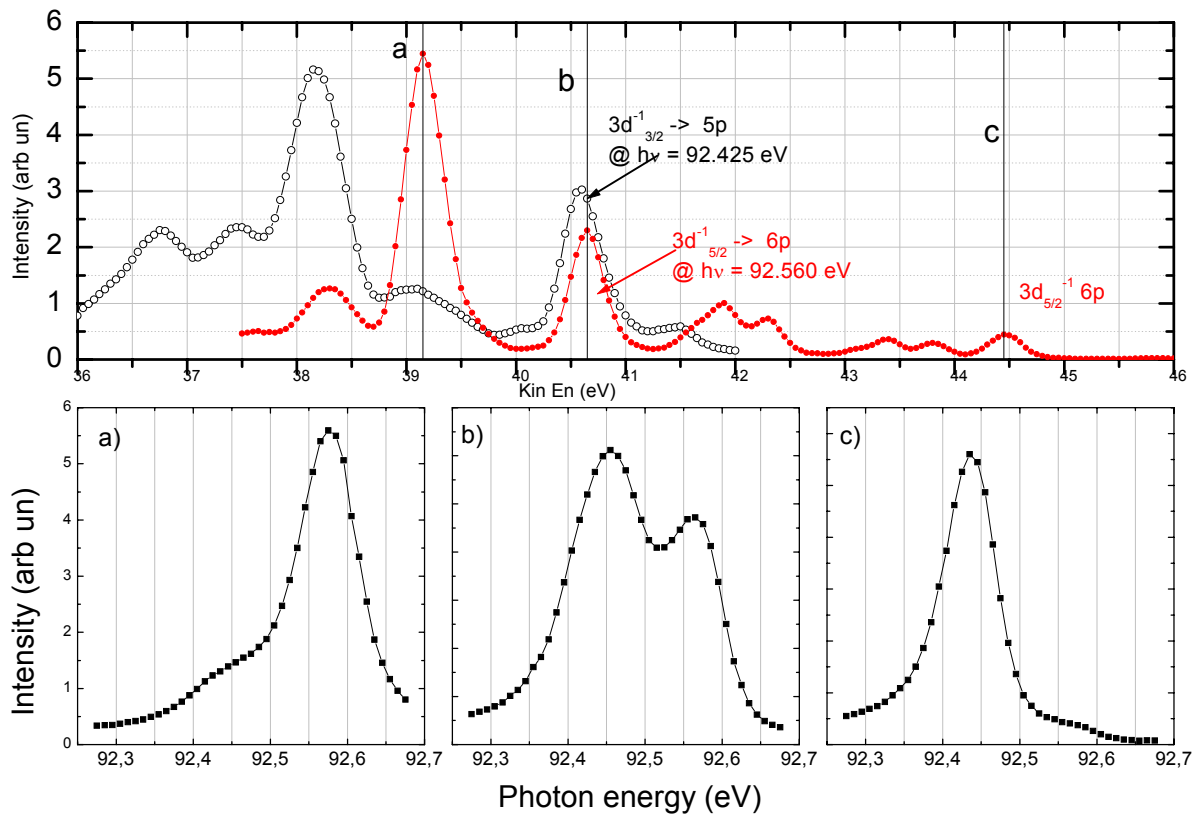


Figure (5-4 3). The upper panel shows two electron spectra, the open circle spectrum is taken at $h\nu = 92.425$ eV and the solid circle spectrum is taken at $h\nu = 92.56$ eV. The lower panel shows three $h\nu$ spectra measured at three different kinetic energies denoted by the three vertical lines a), b) and c). Interesting is the measurement (b) where both neighboring resonances overlap.

The upper panel of figure (5-4 3) shows two electron spectra of the resonant Auger for both transitions : $3d_{3/2}^{-1}5p \rightarrow 4s^{-1}4p^{-1}5p$ and $3d_{5/2}^{-1}6p \rightarrow 4s^{-1}4p^{-1}6p$.

In the lower panel there are three $h\nu$ scans . The kinetic energy in each of the 3 $h\nu$ scans a, b and c are shown in the electron spectrum above by the vertical lines a, b and c. This shows that the Kr $3d_{5/2}^{-1}6p \rightarrow 4s^{-1}4p^{-1}6p$ resonant Auger transition and the Kr $3d_{3/2}^{-1}5p \rightarrow 4s^{-1}4p^{-1}5p$ resonant Auger transition are very close to each other.

In figure (5-4 4) the transferred spin polarization P_{transf} for both resonant Auger transition and the neighboring lines are shown. The electrons of the Kr $3d_{3/2}^{-1}5p \rightarrow 4s^{-1}4p^{-1}5p$ resonant Auger transition which is the transition of interest have spin polarization of -46% and the electrons of the Kr $3d_{5/2}^{-1}6p \rightarrow 4s^{-1}4p^{-1}6p$ resonant Auger transition which represent the spectral background have a spin polarization of 52% . Hence this background has a great influence and must be subtracted, as we have shown above.

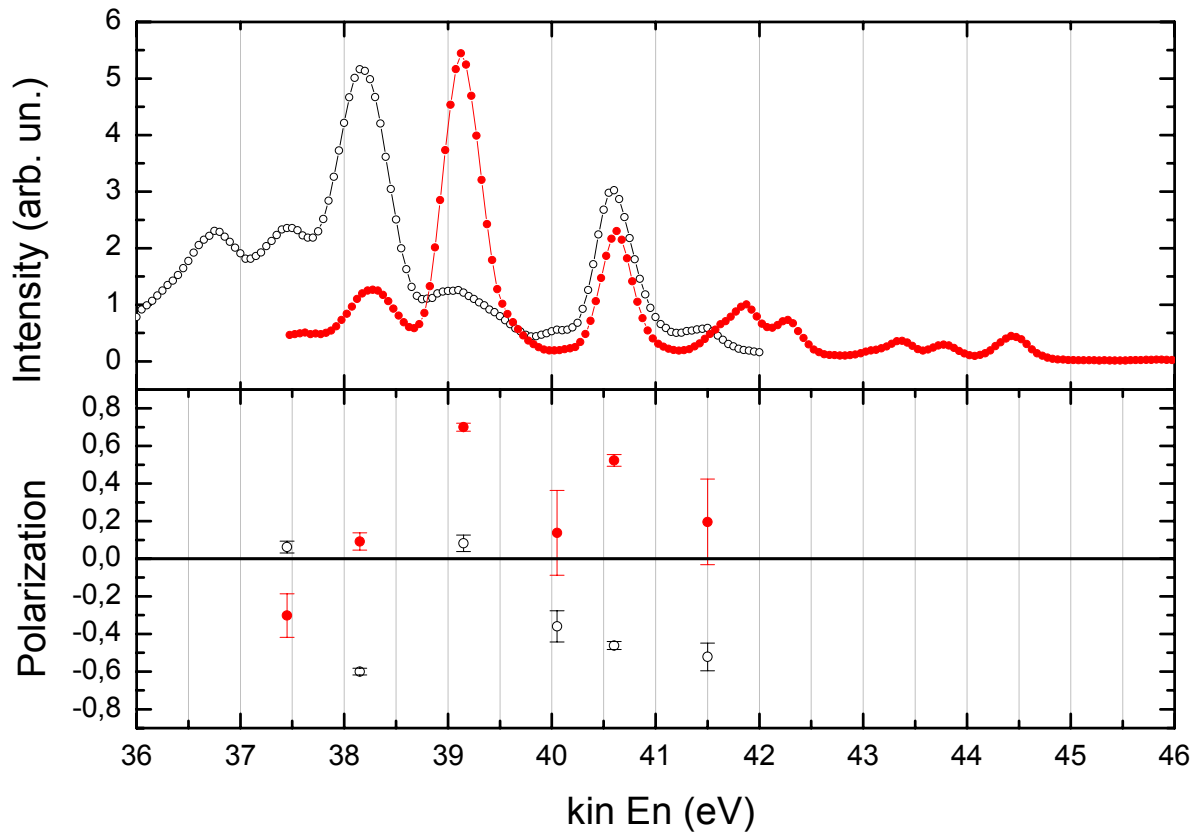
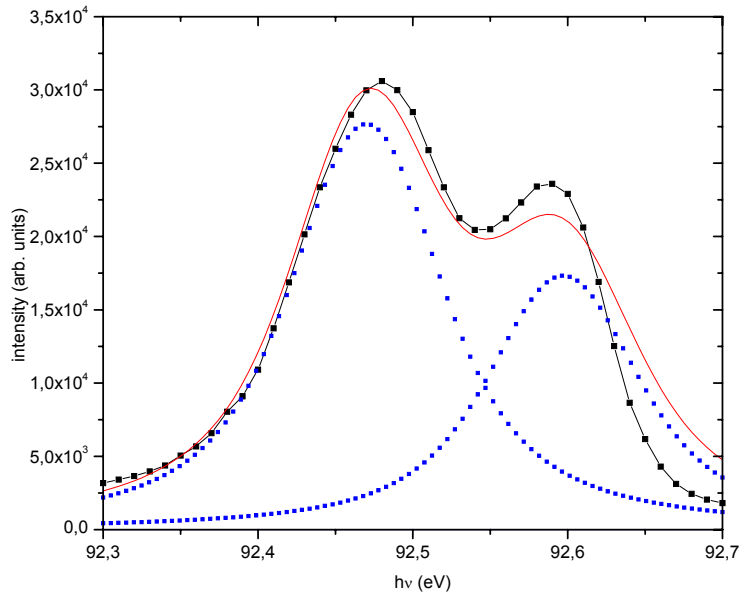


Figure (5-4 4). The upper panel shows two electron spectra, the open circle spectrum is taken at $h\nu = 92.425$ eV and the solid circles spectrum is taken at $h\nu = 92.56$ eV. The lower panel shows the transferred spin polarization of both resonant Auger transitions. The open circles represent the transferred spin polarization of $3d_{3/2}^{-1}5p \rightarrow 4s^{-1}4p^{-1}5p$ and the solid circles represent the transferred spin polarization of $3d_{5/2}^{-1}6p \rightarrow 4s^{-1}4p^{-1}6p$.

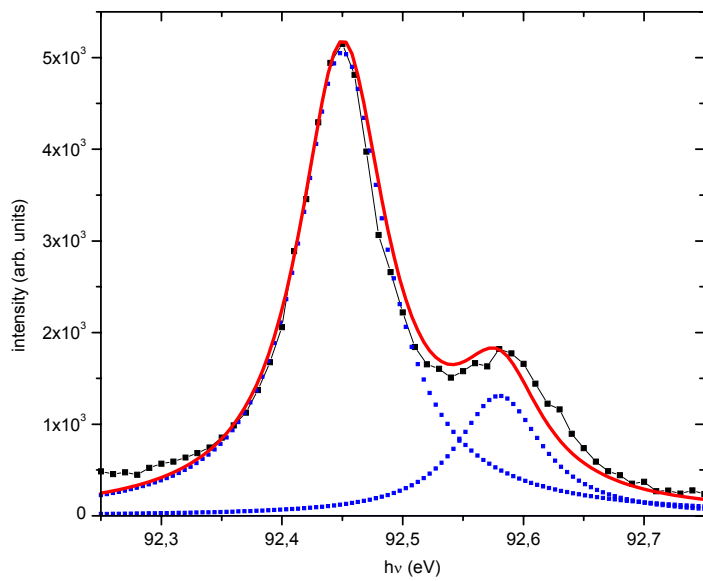
5.4.1 The line fitting of the $h\nu$ scan of the neighboring resonant Auger transitions Kr $3d_{3/2}^{-1}5p \rightarrow 4s^{-1}4p^{-1}5p$ and Kr $3d_{5/2}^{-1}5p \rightarrow 4s^{-1}4p^{-1}6p$

Figure (5-4 5) shows a $h\nu$ scan for the beamline exit slit of 400μ and figure (5-4 6) shows the $h\nu$ scan for a beamline exit slit of 50μ . In both figures the solid line-point curve is the actual measured spectrum, the pointed curves are the Voigt fit of both resonant Kr lines, and the solid line is the sum. The first Kr $3d_{5/2}^{-1} \rightarrow 4s^{-1}4p^{-1}6p$ Voigt fit line at 92.560 eV has a Lorentz width of 86 meV, the Kr $3d_{3/2}^{-1} \rightarrow 4s^{-1}4p^{-1}6p$ Voigt fit line at 92.425 eV has a Lorentz width of 84 meV [45]. For a beam line exit slit of 50μ the Voigt fit corresponds almost exactly to the measured $h\nu$ spectrum, the line width of both lines and their separation of 135 meV agree very well with the measurement.

For a beam line exit slit of 400μ , however the Voigt fit does not correspond to the measured $h\nu$ spectrum, the line width of both lines and their 135 meV separation do not match the measurement very well. Because we have measured the spin polarization of the Kr $3d_{3/2}^{-1} \rightarrow 4s^{-1}4p^{-1}6p$ resonant transition with a slit width = 500μ , there is some uncertainty in determining whether the electron background comes from the Kr $3d_{5/2}^{-1} \rightarrow 4s^{-1}4p^{-1}6p$ resonant transition.



Figure(5-4 5). hv spectrum with slit = 400 μ of resonant Kr 3d $^1_{3/2}$. The spectrometer was set to 38.35 eV.



Figure(5-4 6). hv spectrum with slit = 50 μ of resonant Kr 3d $^1_{3/2}$. The spectrometer was set to 41 eV.

6 Results and Discussion

6.1 Spin polarization transfer for dipole resonances

The calculations performed by N. M. Kabachnik and S. Fritzsche¹ of the intrinsic parameters and the transferred spin polarization for both resonant Auger transitions in addition to the measured transferred spin polarization are presented. The experimental uncertainty includes the statistical error and the uncertainty due to the analyzing power S_{eff} of the Mott polarimeter.

The calculations have not considered the shake up satellite in line IV. The transferred spin polarization of line V² was not measured (see tables (6-1) and (6-2)) and figures (6-1 1) and (6-1 2). The large value of the transferred spin polarization is partially due to the large value of the orientation $A_{10} = \sqrt{3/2} [6]^2$ or [39].

6.1.1 Resonantly excited $3d^{-1}_{5/2} 5p$ state of Krypton

Table (6-1). The measured transferred spin polarization of resonantly excited $3d^{-1}_{5/2} 5p$ state of Krypton and the calculated values

Group	Final State	α_2	ξ_1	Calculation(P_x)	P_x	δP_x
II	$4s^{-1}4p^{-1}(^1P)5p^2S, ^2P, ^2D$	-0.357	-0.678	0.737	0.780	0.064
IV	$4s^{-1}4p^{-1}(^1P)6p$				0.733	0.062
V	$4p^{-3}(^2D)4d(^1P)5p$	-0.361	-0.699	0.759	0.755	0.066
VI	$4s^{-2}(1S)5p^2P$	-0.555	-0.744	0.762	0.795	0.065

¹ private communication.

² V. V. Balashov, A. N. Grum-Grzhimailo and N. M. Kabachnik 2000 Polarization and correlation Phenomena in Atomic Collisions. A Practical Theory Course (New York: Kulwer Academic) page 59

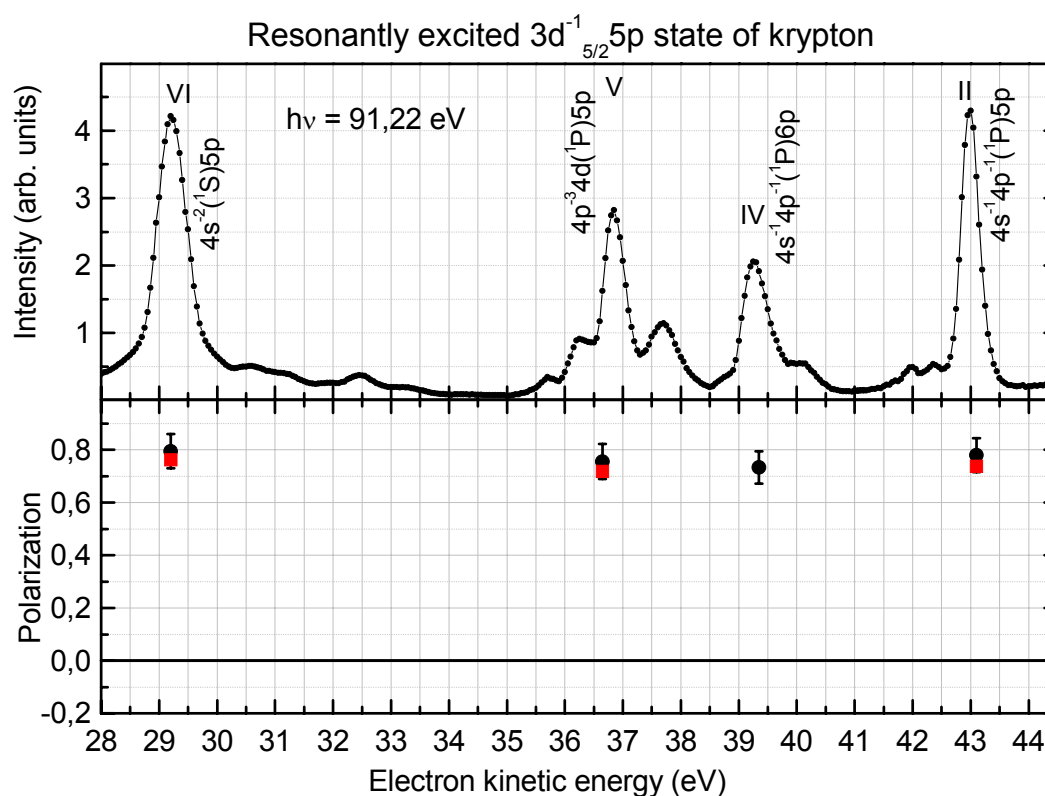


Figure (6-1 1). The measured transferred spin polarization of the resonantly excited $3d_{5/2}^{-1}5p$ state of Krypton and the calculated values. The black circles are the measured values and the gray squares are the calculations.

6.1.2 Resonantly excited $3d_{3/2}^{-1}5p$ state of Krypton

Table (6-2). The measured transferred spin polarization of the resonantly excited $3d_{3/2}^{-1}5p$ state of Krypton and the calculated values

Group	Final State	α_2	ξ_1	Calculation(P_x)	P_x	δP_x
II	$4s^{-1}4p^{-1}(^1P)5p^2S, ^2P, ^2D$	-0.312	0.591	-0.652	-0.660	0.057
IV	$4s^{-1}4p^{-1}(^1P)6p$				-0.54	0.064
V	$4p^{-3}(^2D)4d(^1P)5p$	-0.313	0.586	-0.646	-0.638	0.055
VI	$4s^{-2}(1S)5p^2P$	-0.457	0.722	-0.761	-0.731	0.060

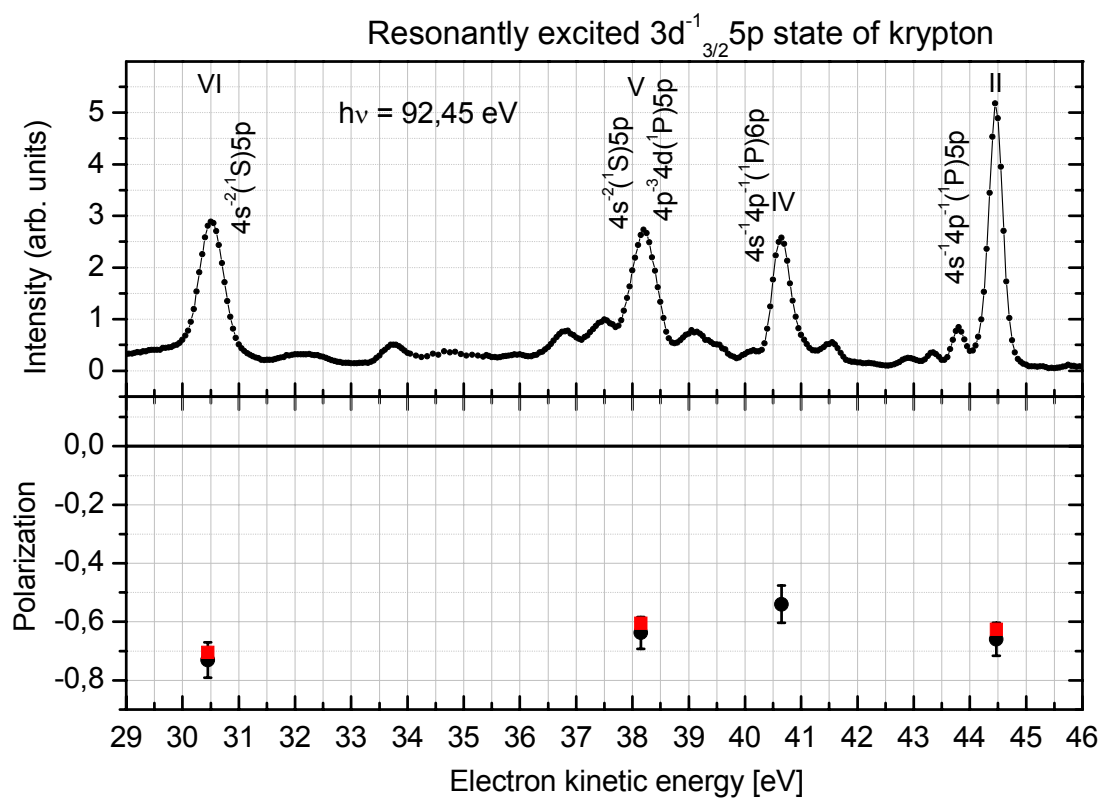


Figure (6-1 1). The measured transferred spin polarization of the resonantly excited $3d^{-1}_{3/2} 5p$ state of Krypton and the calculated values. The black circles are the measured values and the gray squares are the calculations.

6.2 Quadrupole–Dipole Interference in Spin Polarization of Photoelectrons from the Xe 4p shell

To measure the contribution of nondipole terms in photoelectron spin polarization of Xe 4p photoelectrons, it is necessary to select a special measurement geometry in which the electric dipole approximation gives a vanishing value at certain selected angles of electron ejection.

In the selected geometry two orthogonal components were measured:

- 1) P_{long} , the component of the spin polarization of Xe 4p photoelectrons which contains the non dipole contribution to the electron spin polarization,
- 2) the component P_{trans} of the spin polarization of Xe 4p photoelectrons which contains the dipole contribution.

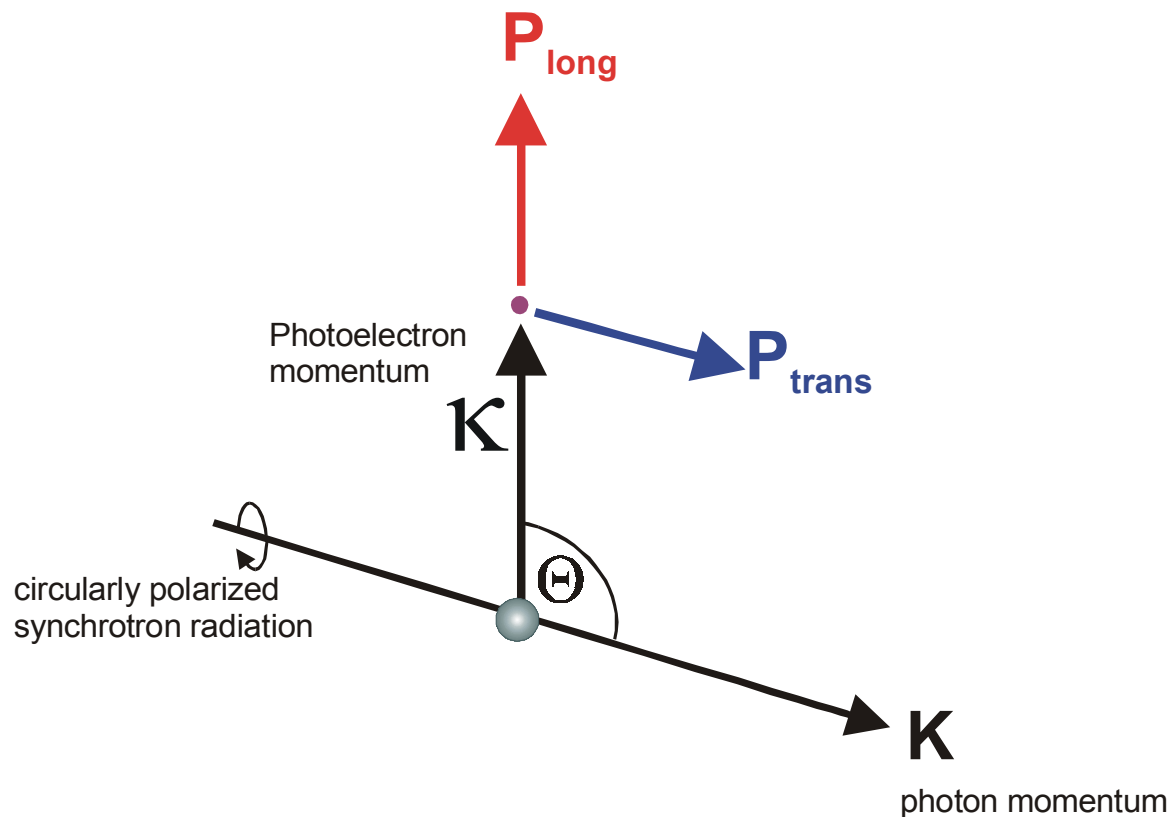


Figure (6-2 1). The two measured spin polarization components: P_{long} is along κ and P_{trans} is along \mathbf{k} .

The P_{long} spin component, see equation (2-5 2), is defined through the geometry where; the unit vector κ in the direction of photoelectron and the unit vector \mathbf{k} in the direction of the circularly polarized light are perpendicular and the spin unit vector: \mathbf{s} is parallel to κ .

$$P_{\text{long}} \Leftrightarrow \kappa \perp \mathbf{k} , \mathbf{s} \perp \mathbf{k}, \mathbf{s} \parallel \kappa$$

$$P_{\text{long}}^{\pm 1} = \pm (1 + 1/4 \beta)^{-1} (\sqrt{6/2} (B_{211}^{1/2} + \sqrt{3/2} B_{231}^{1/2}) = \pm (2 + \beta/2)^{-1} (-\delta) \quad (2-5 2)$$

In this geometry where both unit vectors κ and \mathbf{s} are perpendicular to \mathbf{k} *the electric dipole approximation gives a zero result* to the spin polarization component P_{long} .

As discussed in the theory (section 2.5) the spin polarization component P_{perp} , where all the three unit vectors are perpendicular, contain the non dipole contribution to the electron spin polarization. The component P_{long} was preferred however due to its sign change according to the light helicity. This effect is used to eliminate the apparative asymmetry to the first order as discussed in section 5.1.

The P_{trans} component is the component measured in the geometry, where $\kappa \perp \mathbf{k}$, $\mathbf{s} \parallel \mathbf{k}$, $\mathbf{s} \perp \kappa$

$$P_{\text{trans}} \Leftrightarrow \kappa \perp \mathbf{k}, \mathbf{s} \parallel \mathbf{k}, \mathbf{s} \perp \kappa$$

$$P_{\text{trans}}^{\pm 1} = \pm (1 + 1/4 \beta)^{-1} (A + \gamma/2) \quad (6-2 1)$$

see figure (2-5 2).

In this geometry *the electric dipole approximation gives a maximal contribution* to the spin polarization component P_{trans}

6.2.1 Asymmetry parameter β close to ionization

The predicted quadrupole resonance in the photoionization cross section of Xe 4p near the ionization threshold is not easy to detect due to the smallness of the cross section at low photon energies [18]. This quadrupole resonance in Xe 4p photoelectrons can be observed indirectly by measuring the angular distribution of the Xe 4p photoelectrons.[23], [51], [21], [24] and [59] which have shown the breakdown of the dipole approximation as a description of angular distribution of photoelectrons at low photon energies.

The asymmetry parameter β was measured close to the ionization threshold using linearly polarized light. The plane of polarization of light was switched between horizontal and vertical relative to the direction of photoelectron κ to gain photoelectron intensities for the two angles 0° and 90° between the plane of light and the direction of photoelectron κ to determine the asymmetry parameter β . The result is shown in figure (6-2 2) together with the experimental data of U Becker et al [8], the RRPA calculation by M. Kutzner et al [50], the RPAE *ab initio* calculation by Cherepkov [17]. Both RRPA and RPAE are shifted to the experimental ionization threshold. The error bars are due to the uncertainties arising from the background subtraction. Especially at the photon energies $h\nu = 152.5$ eV and $h\nu = 158$ eV the value of the β parameter turns out to be very sensitive to the neighbouring peaks, leading to a large uncertainty for these points. The measurements between $h\nu = 180$ eV and $h\nu = 200$ eV are in good agreement with the data by Becker et al [8] as well as with the RRPA calculation of Kutzner et al.[50]. We note that the measured asymmetry parameter β follows the sign change at $h\nu = 175$ eV which is also predicted by the theory. Comparing these data to the RPAE calculation it turns out that the β parameter is far from the theory close to the ionization threshold. Also the sign change at ca. $h\nu = 175$ eV favours the unshifted result of the calculation opposite to the nondipole sensitive component P_{long} discussed below.

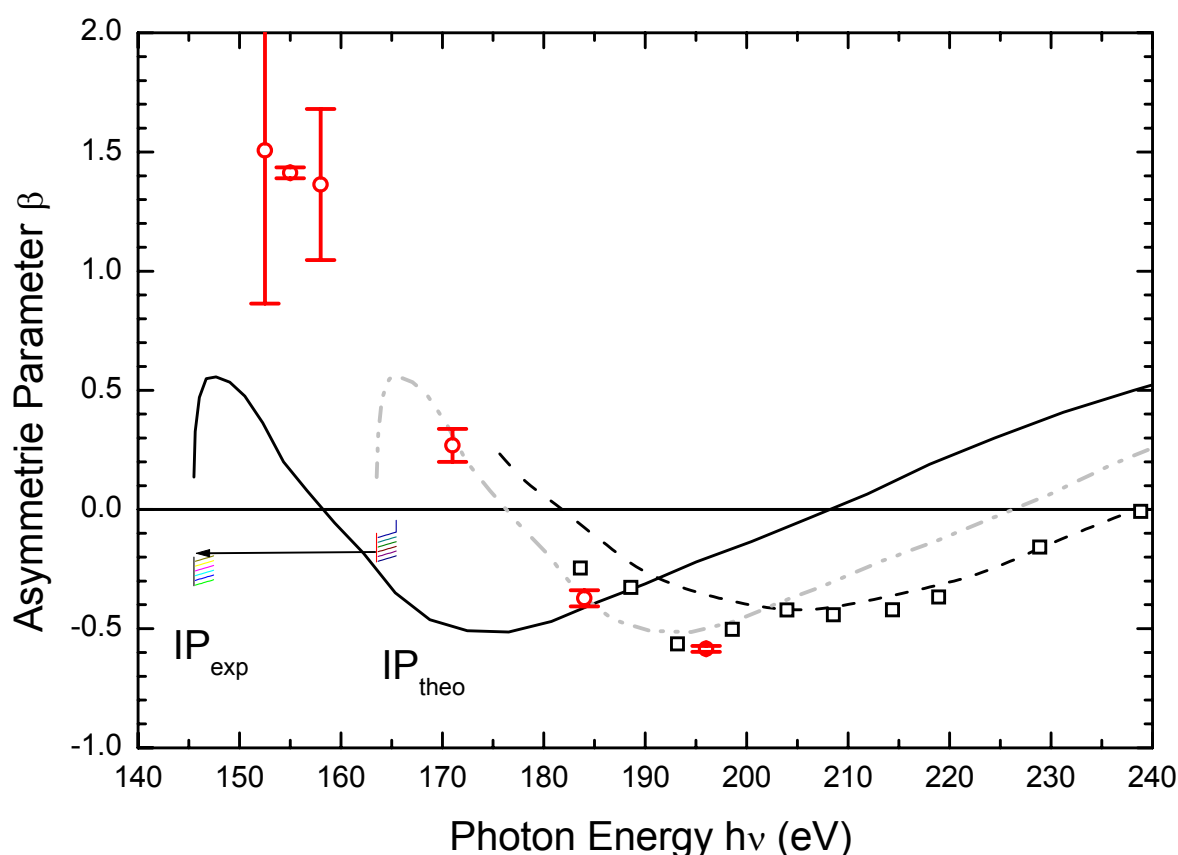


Figure (6-2 2). The measured β parameter for Xe 4p photoelectrons. The circles are our measurements, the squares are the measurement of U. Becker [8]. The gray dash-point curve is the ab initio calculation by Cherepkov [17]. The black solid curve is the shifted gray curve. The black dashed curve is the theory of M Kutzner [49].

6.2.2 Electron Correlations in Xe 4p photoelectrons

The Xe 4p spectrum is dominated by a strong peak which carries about 25% of the total spectral strength [see Figure (5-3 1)], while the rest of the total spectral strength resides above the $4d^8$ threshold. The main peak of Xe 4p seems to arise from a doubly excited level below the $4d^8$ ionization threshold in the form of a compact $4d^8 4f$ configuration which is very strongly perturbed by a $4p^5_{3/2}$ configuration. Neither a Xe $4p_{1/2}$ nor a Xe $4p_{3/2}$ hole can exist as an elementary excitation but becomes smeared over a large energy range. If a Xe 4p hole is created, it will be destroyed by dipolar fluctuations in a short time compared to the period of oscillation and the concept of a 4p hole is therefore meaningless. The most stable and probable state was found to belong to the $Xe^+(4d^8 4f)_{3/2}$ configuration at 145.5 eV [72].

According to this reasoning the measured photoelectron spin polarization of Xe 4p is mainly of Xe $4p_{3/2}$. The theory for the nondipole contribution for spin polarization of Xe 4p is based on calculations for Xe $4p_{1/2}$, and the Xe 4p electron correlations mentioned above were not taken into account.

Within a nonrelativistic approximation and according to the fact that both Xe $4p_{1/2}$ and

Xe $4p_{3/2}$ are fine structure components of the final state due to the ℓs coupling, the spin polarization should vanish if one integrates over both fine structure components in the final state. Consequently the spin polarization of the Xe $4p_{3/2}$ can be deduced from the calculated values for Xe $4p_{1/2}$ when we know the branching ratio that is the relative intensity of both Xe $4p_{1/2}$ and Xe $4p_{3/2}$ which can not be done experimentally as mentioned above. The statistical weight of the magnetic substates $I_{3/2} / I_{1/2} = 2$ is considered instead and correspondingly the theoretical spin polarization curves for Xe $4p_{1/2}$ shown in figures (2-5 1) and (2-5 2) were multiplied by the factor $-1/2$ to obtain the corresponding spin polarization curves for Xe $4p_{3/2}$.

6.2.3 Transferred spin component P_{trans}

The measured transferred spin component P_{trans} , that is the component resulting mainly from the electric dipole contribution, agrees in sign and magnitude with the theoretical data which are calculated according to equation (6-2 1) for Xe $4p_{1/2}$ when these data are multiplied with a factor $-1/2$ as shown in figure (6-2 3).

This justifies our selection of the factor $-1/2$ as discussed in section 6.2.2 and confirms that the measured Xe $4p$ photoelectrons have a Xe $4p_{3/2}$ character.

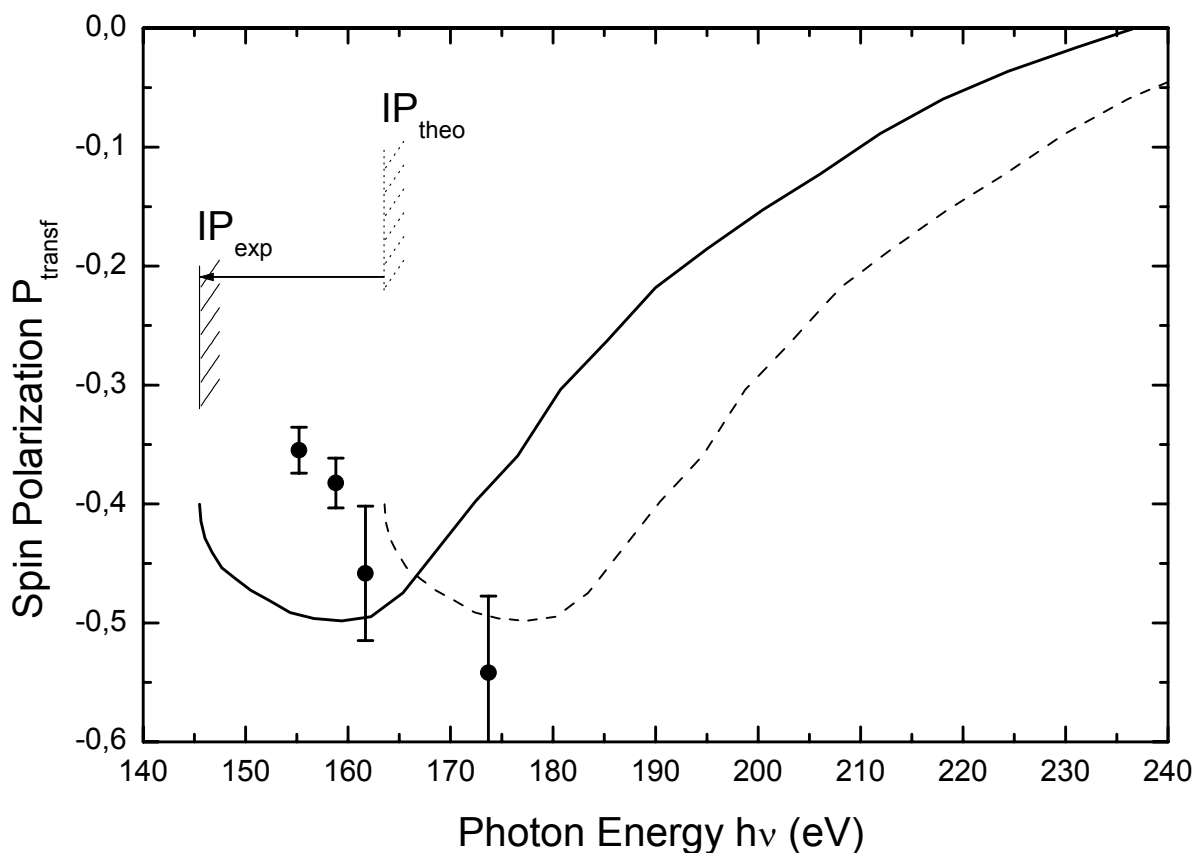


Figure (6-2 3). The measured transferred spin polarization P_{trans} of Xe $4p$. The dashed curve is the calculation by Cherepkov for Xe $4p_{1/2}$ multiplied by a factor $-1/2$. The solid curve is the dashed one shifted to the ionization threshold.

6.2.4 Nondipole sensitive component P_{long}

Figure (6-2 4) shows the measured nondipole sensitive component P_{long} for photon energies close to the ionization threshold of about 150 eV up to 185 eV.

The figure shows the RPAE calculation by Cherepkov adapted for Xe $4p_{3/2}$ as discussed in section 6.2.2 and the adapted IPA calculation by Derevianko [23] for Xe $4p_{3/2}$ (the β and δ parameters are obtained from the relativistic independent particle approximation (IPA) of Derevianko et al and substituted in the second part of equation (2-5 2)). Both IPA and RPAE curves are shifted to the ionization threshold. The measured nondipole sensitive component P_{long} favours the shifted result of the calculation opposite to the asymmetry parameter β discussed above.

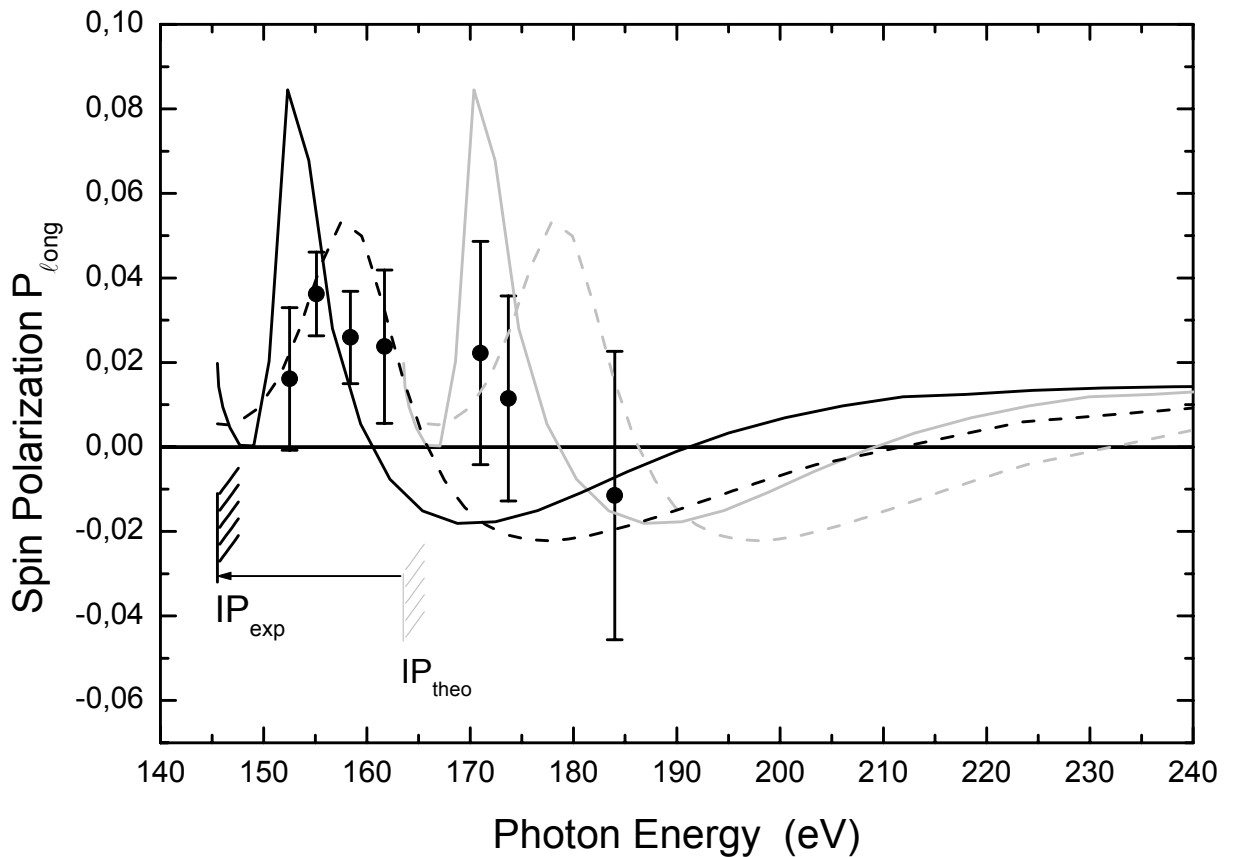


Figure (6-2 4). The measured nondipole sensitive spin polarization component and the theory curves; the solid grey curve is the *ab initio* RPAE theory of the nondipole sensitive spin polarization component [17] and the dashed gray curve is the from *ab initio* IPA theory [23] adapted curve; both theory curves are shifted to the experimental threshold; the solid black curve is the shifted RPAE theory; and the dashed black curve is the shifted IPA theory.

7 Summary

In the first part of this thesis, the transferred spin polarization of resonantly excited Auger electrons of Kr $3d^{-1} 5p$ photoionized by circularly polarized light was measured. The transferred spin polarization is related to the orientation A_{10} (and alignment A_{20}) of core holes induced by the primary photoionization process, and to the intrinsic parameters ξ_1 which characterizes the transferred spin polarization of Auger electrons and α_2 , the anisotropy parameter which characterizes the angular intensity distribution of Auger electrons. Due to the selection rules of dipole excitation of Kr $3d^{-1} 5p$ atoms i.e. $J_i = 1$, A_{10} and A_{20} are known [6], α_2 was calculated and measured by Kitajima [46] et al. The calculation of ξ_1 was performed by N. M. Kabachnik and S. Fritzsche¹.

In the second part of this thesis, the spin polarization of Xe 4p near the ionization threshold was measured to examine the calculations of Cherepkov [17] of contribution of the lowest order nondipole term; the electric-dipole-electric-quadrupole interference terms to the spin polarization of Xe np photoelectrons. The quadrupole matrix elements of the $np \rightarrow \epsilon f$ transitions in Xe calculated in RPAE [18] have strong maxima near the ionization threshold. This behaviour is similar to the well-known maxima in the dipole $nd \rightarrow \epsilon f$ transitions. These dipole $nd \rightarrow \epsilon f$ transitions are responsible for the so-called giant resonances in the total photoionization cross section. They are attributed to the double-well shape of the effective potential for the dipole ϵf partial waves. Both the RPAE non-relativistic calculation from Cherepkov and the relativistic IPA adapted calculation from Derevianko agree qualitatively with the measured nondipole component of electron spin polarization.

¹ Private communication.

8 Appendices

8.1 Appendix 1: Intrinsic parameters and Coulomb matrix elements of the Xe N₄O_{2,3}O_{2,3}³P₁ Auger decay

Spin polarization and intrinsic parameters:

Figure(2-2.5) shows the laboratory coordinate frame of the experiment for measuring the transferred spin polarization of Xe N₄ O_{2,3} O_{2,3}³P₁ Auger electrons with circularly polarized light. The relations for angular distribution and spin polarization are given by the following expressions [63].

$$d\sigma/d\Omega \propto 1 + A_{20} \alpha_2 P_2(\cos\theta) \quad (\text{A-1 1})$$

$$P_{\text{transf}}(\theta) = P_z = (1 + A_{20} \alpha_2 P_2(\cos\theta))^{-1} (A_{10} (\beta_1 + \gamma P_2(\cos\theta))) \quad (\text{A-1 2})$$

$$P_{\text{dyn}}(\theta) = P_y = (1 + A_{20} \alpha_2 P_2(\cos\theta))^{-1} (A_{20} \xi \sin 2\theta) \quad (\text{A-1 3})$$

$$P_{\parallel}(\theta) = P_x = (1 + A_{20} \alpha_2 P_2(\cos\theta))^{-1} (3/4 A_{10} \gamma_1 \sin 2\theta) \quad (\text{A-1 4})$$

$d\sigma/d\Omega$ is the differential cross section for photoionization, P_{transf} and P_{\parallel} are the components of spin polarization in the reaction plane spanned by the photon momentum \mathbf{k} and photoelectron momentum κ , P_{dyn} is the component of spin polarization perpendicular to the reaction plane. A_{10} , A_{20} are the orientation and alignment discussed briefly in chapter 2, $P_2(\cos\theta)$ is the second Legendre polynomial. The parameters α_2 , β_1 , γ_1 and ξ_2 are the intrinsic parameters describing the dynamical properties of the Auger decay.

Connection between intrinsic parameters and Coulomb matrix elements:

The intrinsic parameters α_2 , β_1 , γ_1 , and ξ_2 are related to the amplitude ratios and phase shift differences of Coulomb matrix elements η_1 , η_2 , δ_1 and δ_2 [(2-2 2)-(2-2 5)] in the special Auger decay Xe N₄ O_{2,3} O_{2,3}³P₁ [36], [52].

$$\alpha_2 = (-5(1+\eta_1^2+\eta_2^2))^{-1} (\eta_2^2 + 4 + 4\sqrt{5}\eta_1\eta_2\cos(\delta_1-\delta_2) - 2\sqrt{5}\eta_1\cos(\delta_1) + 4\eta_2\cos(\delta_2)) \quad (\text{A-1 5})$$

$$\beta_1 = (-75(1+\eta_1^2+\eta_2^2))^{-1} (\sqrt{5} - 25\eta_1^2 + 11\eta_2^2 - 21 + 24\eta_2\cos(\delta_2)) \quad (\text{A-1 6})$$

$$\gamma_1 = (-75(1+\eta_1^2+\eta_2^2))^{-1} (2\sqrt{5} - 11\eta_2^2 + 6 + 10\sqrt{5}\eta_1\eta_2\cos(\delta_1-\delta_2) + 6\eta_2\cos(\delta_2)) \quad (\text{A-1 7})$$

$$\xi_1 = (-\sqrt{5(1+\eta_1^2+\eta_2^2)})^{-1}(3\eta_1\eta_2\sin(\delta_1-\delta_2)+\eta_1\sin(\delta_1)-\sqrt{5}\eta_2\sin(\delta_2)) \quad (\text{A-1 8})$$

8.2 Appendix 2: The parameters defining the nondipole corrections to the angular distribution and spin polarization of Xe np photoelectrons [18]

Some terms in equation (2-4 5) are related to the dipole polarization parameters introduced in (2-4 2) by the equations

$$B_{220}^j = -1/2\sqrt{5} \beta^j$$

$$B_{101}^j = 1/\sqrt{3} A^j$$

$$B_{121}^j = 1/\sqrt{6} \gamma^j$$

$$B_{221}^j = \sqrt{2i/3}\sqrt{6}\eta^j$$

The new parameters defining the nondipole corrections in equation (2-4 5) are given by the resses

$$B_{110}^{1/2} = k/B\sqrt{(6/5)}[d_0q_1\cos(\delta_0-\delta_1) + 1/5\sqrt{2} d_2q_1 \cos(\delta_1-\delta_2) + 3\sqrt{3/5} d_2q_3 \cos(\delta_2-\delta_3)],$$

$$B_{330}^{1/2} = k/B\sqrt{(3/35)}[d_0q_3\cos(\delta_0-\delta_3) + 3\sqrt{3/5} d_2q_1 \cos(\delta_1-\delta_2) + 2\sqrt{2/5} d_2q_3 \cos(\delta_2-\delta_3)],$$

$$B_{111}^{1/2} = ik/B\sqrt{5}[d_0q_1\sin(\delta_0-\delta_1) + 2\sqrt{2/5} d_2q_1 \sin(\delta_1-\delta_2) - 3\sqrt{3/5} d_2q_3 \sin(\delta_2-\delta_3)],$$

$$B_{211}^{1/2} = k/B\sqrt{(3/5)}[d_0q_1\cos(\delta_0-\delta_1) - \sqrt{2/5} d_2q_1 \cos(\delta_1-\delta_2) - \sqrt{3/5} d_2q_3 \cos(\delta_2-\delta_3)],$$

$$B_{231}^{1/2} = k/B\sqrt{(2/15)}[d_0q_3\cos(\delta_0-\delta_3) + 3\sqrt{3/10} d_2q_1 \cos(\delta_1-\delta_2) - 4\sqrt{2/5} d_2q_3 \cos(\delta_2-\delta_3)],$$

$$B_{331}^{1/2} = ik/B 4\sqrt{105}[d_0q_3\sin(\delta_0-\delta_3) + 3\sqrt{3/5} d_2q_1 \sin(\delta_1-\delta_2) + \sqrt{2/10} d_2q_3 \sin(\delta_2-\delta_3)],$$

where $B = (d_0)^2 + (d_2)^2$, d_λ is the dipole operator defined in (2-4 1),

δ_l are the phase shifts of partial waves with orbital angular momentum l and

$$q_l = -1/\sqrt{10} \int dr r^4 R_{sp}(r) R_{nt}^{1/2}(r).$$

$$q_3 = \sqrt{3/2}\sqrt{5} \int dr r^4 R_{\text{eff}}(r) R_{n\ell}^{1/2}(r).$$

The nondipole parameters contain four new theoretical values, two quadrupole matrix elements q_1 and q_3 and two corresponding phase shift differences for example $(\delta_2 - \delta_3)$ with $\ell = 2, 3$.

9 Abbreviations

BESSY	Berliner Elektronenspeicherring-Gesellschaft für Synchrotronstrahlung m. b. H.
CSF	Configuration state function.
FISCI	Final ionic state interaction.
HF	Hartee-Fock Method.
IPA	relativistic Independent Particle Approximation.
ISCI	Initial state configuration Interaction.
IISCI	Initial ionic state-configuration Interaction.
MCDF	Multiconfiguration Dirack-Fock calculations.
RPAE	Random Phase Approximation with Exchange.
RRPA	Relativistic Random Phase Approximation.
UHV	Ultra high Vacuum.

10 References

- [1] H. Aksela, J. Jauhiainen, E. Nömmiste, and S. Aksela *Phys. Rev. A* **54**, 605 (1996).
- [2] M. Ya. Amusia, and N. A. Cherepkov, *Case Stud. At. Phys* **5** 47. (1975).
- [3] M. Ya. Amusia, A. S. Baltakov, Z. Felfli and Msezane *A Z Phys. Rev. A* **59** 2544 (1999).
- [4] G. Bradley Armen, Helena Aksela, Teijo Åberg, and Seppo Aksela. *J. Phys B: At. Mol. Opt. Phys.* **33** R49 (2000).
- [5] David Attwood, *Soft X-Rays and extreme Ultraviolet Radiation* Cambridge University Press (1999).
- [6] V. V. Balashov, A. N. Grum-Grzhimailo, and N. M. Kabachnik 2000 *Polarization and correlation Phenomena in Atomic Collisions. A Practical Theory Course* (New York: Kulwer Academic)
- [7] A. Bechler, and R H Pratt, *J. Phys. B* **32** 2889 (1999).
- [8] U. Becker, D. Szostak, H. G. Kerkhoff, M. Kupsch, B. Langer, R. Wehlitz. A. Yagishita and T. Hayaishi *Phys. Rev. A* **39**, 3902 (1989).
- [9] U Becker, D Szostak, M Kupsch, H G Kerkhoff, B Langer, and R Wehlitz *J. Phys. B: At. Mol. Opt. Phys.* **22** 749 (1989).
- [10] H. A. Bethe and E. E. Salpeter, *Quantum Mechanics of One- and Two-Electron Atoms* (1977).
- [11] K Blum, B Lohmann, and E Taute *J. Phys. B* **19** 815(1986).
- [12] B. H. Bransden, and C. J. Joachian *Physics of Atoms and Molecules* Longmann Inc., New York
- [13] C. Brechignac, and J. P. Connerad *J. Phys. B: At. Mol. Opt. Phys.* **27**, 3795 (1994).
- [14] T. A. Carlson, D. R. Mullins, C E Beall, B. W. Yates, J. W. Taylor, D. W. Lindle, B. P. Pullen, and F. A. Grimm *Phys. Rev. Lett.* **60**, 1382 (1988).
- [15] T. A. Carlson, D. R. Mullins, C E Beall, B. W. Yates, J. W. Taylor, D. W. Lindle, and F. A. Grimm *Phys. Rev. A* **39** 1170 (1989).
- [16] N. A. Cherepkov, *adv. At. Mol. Phys.* **19**, 395. (1983).
- [17] N. A. Cherepkov, and S. K. Semenov *J. Phys. B* **34** L211 (2001).
- [18] N. A. Cherepkov, and S. K. Semenov *J. Phys. B* **34** L495 (2001).
- [19] J. W Cooper, *Phys. Rev.* **128**, 681 (1962)
- [20] J. W Cooper, T. Manson *Phys. Rev.* **177** 157 (1969).
- [21] J. W Cooper, *Phys. Rev. A* **47**, 1841 (1993).

- [22] M. Drescher. Rotationsaufgelöste Charakterisierung der Autoionisationsresonanzen von HCl und DCI durch Messung der Photoelektronenspinpolarisation. Dissertation, Universität Bielefeld, (1993).
- [23] A.Derevianko, W. R.Johnson and K. T.Cheng *At. Nucl. Data Tables* **73**, 153 (1999).
- [24] A.Derevianko , O. Hemmers, S. Oblad, P. Glans, H. Wang, S. B. Whitfield, R. Wehlitz, I. A. Sellin, W. R. Johnson, and D. W. Lindle *Phys. Rev. Lett.* **84** 2116 (2000).
- [25] U. Fano, *Phys. Rev.* **178**, 131 (1969).
- [26] T. J. Gay, and F. B. Dunning *Rev. Sci. Instrum.* **63** 1635 (1991).
- [27] A. Gellrich, K. Jost, and J. Kessler *Rev. Sci. Instrum.* **61** 3399(1990).
- [28] U.Heinzmann and N. A. Cherepkov *VUV and Soft X-Ray Photoionization Studies* ed U Becker and D A Shirley (New York: Plenum) pp521-559. (1996)
- [29] U.Heinzmann, *Phys. Rev. Lett.* **25**, 1325 (1970).
- [30] O Hemmers, G Fisher, P Glans, D L Hansen, H Wang, S B Whitfield, R Wehlitz, J C Levin, I A Sellin, R C C Perera, E W B Dias, H S Chakraborty, P C Deshmukh, S T Manson and D W Lindle *J. Physy. B: At. Mol. Opt. Phys.* **30** L727 (1997).
- [31] U Hergenbahn, N M Kabachnik, and B Lohmann *J. Physy. B: At. Mol. Opt. Phys.* **24** 4759 (1991).
- [32] K. N. Huang, *Phys. Rev. A* **26**, 2274 (1982).
- [33] R. E. Imhof and F. H. Read *J. Phys. B: Atom. ;Molec. Phys.*, Vol. **4**, 450 (1971).
- [34] K. Jost *J. Phys. E: Sci. Instrum.* Vol. 12, (1979).
- [35] N. M.Kabachnik *J. Phys. B: At. Mol. Phys.* **14**, L337 (1981).
- [36] N. M.Kabachnik and I. P.Sazhina *J. Phys. B: At. Mol. Phys.* **17**, 1335 (1984).
- [37] N. M.Kabachnik and Lee O V *J. Phys. B: At. Mol. Phys.* **22**, 2705 (1989).
- [38] N. M. Kabachnik. and I. P.Sazhina *J. Phys. B: At. Mol. Opt. Phys.* **23**, L353 (1990).
- [39] N. M.Kabachnik and I. P.Sazhina *J. Phys. B: At. Mol. Opt. Phys.* **35**, 3591(2002).
- [40] B Kammerling, B Krassig and V Schmidt *J. Phys. B: At. Mol. Opt. Phys.* **23** 4487 (1990).
- [41] J. Kessler: *Polarized Electrons* Springer-Verlag 2nd Edition.
- [42] J. Kessler *Rev. Mod. Phys.***41**, 3 (1969).
- [43] T. Khalil, B. Schmidtke, M. Drescher, N. Müller, and U. Heinzmann *Phys. Rev. Lett.* **89**, 53001 (2002).

- [44] Y. S. Kim, I. B. Goldberg, R. H. Pratt *Phys. Rev. A* **51**, 424 (1995).
- [45] G. C. King, M. Tronc, F. H. Read and R. C. Bradford *J. Phys. B: Atom. Molec. Phys.* **10**, 2479, (1977).
- [46] M Kitajima, M Okamoto¹, Y Shimizu H Chiba², S Fritzsche , N M Kabachnik , I P Sazhina, F Koike, T Hayaishi, H Tanaka¹, Y Sato² and K Ueda *J. Phys. B: At. Mol. Phys.* **34**, 3829 (2001)
- [47] Klar H *J. Phys. B: At. Mol. Phys.* **13**, 4741 (1980).
- [48] B. Krässig, M. Jung, D. S. Gemmell, BE. P. Kanter, T. LeBrun, S. H. Southworth, and L. Young 1995 *Phys. Rev. Lett.* **75**, 4736.
- [49] M. O. Krause *Phys. Rev.* **177**, 151 (1969).
- [50] M. Kutzner, V. Radojevic , and H. P. Kelly *Phys.Rev.A* **40**, 5052 (1989).
- [51] Lindle D W and Hemmers O *J. Electron Spectrosc. Relat. Phenom.* **100** 297 (1999).
- [52] B.Lohmann, U. Hergenhahn and N. M. Kabachnik *J. Phys. B: At. Mol. Opt. Phys.* **26** 3327 (1993).
- [53] A. Mank Rotationsselektive Untersuchung von HI-Molekülen durch winkel- und spinaufgelöste Photoelektronenspektroskopie. Dissertation, Universität Bielefeld, (1991).
- [54] N. L. S. Martin , D. B. Thompson, R. P. Bauman , C. D. Caldwell, M. O. Krause, S. P. Frigo, and M. Wilson *Phys. Rev. Lett.* **81**, 1199 (1998).
- [55] W. Melhorn Auger-electron spectroscopy of core levels of atomic Proc. Int. Conf. On X-Ray and atomic Inner-Shell Physics, ed. B Crasemann (New York: American Institute of Physics) (1982).
- [56] W. Mehlhorn Auger-electron spectrometry of core levels of atoms *Atomic Inner-Shell Physics*, ed. B Crasemann (New York: Plenum) (1985)
- [57] C. E. Moore *Atomic Energy Levels (NBS (US) Circular 467)* vol II (Washington, DC: US Govt Printing Office) (1958).
- [58] J. Mursu , J Jauhiainen, H Aksela and S Aksela *J. Phys. B: At. Mol. Opt. Phys.* **31**, 1973 (1998)
- [59] V. I. Nefedov, V. G. Yarzhemsky, I. S. Nefedova, and M. B. Trzhaskovskaya *J. Electron Spectrosc. Relat Phenom.* **113**, 91 (2000).
- [60] K. J. S. Sawhney, F. Senf, M. Scheer, F. Schäfers, J. Bahrtdt, A. Gaupp, W. Gudat *Nuclear Instruments and Methods in Physics Research A* **390** 395 (1997).
- [61] V. Schmidt *Electron Spectroscopy of Atoms using Synchrotron Radiation* Cambridge University Press (1997).
- [62] B. Schmidtke, M. Drescher, N. A. Cherepkov and U. Heinzmann *J. Phys. B: At. Mol. Opt. Phys.* **33**, 2451(2000).

- [63] B. Schmidtke, T. Khalil , M. Drescher, N. Müller, N. M. Kabachnik and U. Heinzmann *J. Phys. B. At. Mol. Phys.* **33**, 5225 (2000).
- [64] B. Schmidtke. Diplomarbeit, Universität Bielefeld, (1998).
- [65] B. Schmidtke , T Khalil , M Drescher, N Müller, N M Kabachnik and U Heinzmann *J.Phys. B. At. Mol. Phys.* **34**, 4293 (2001).
- [66] B. Schmidtke Spinaufgelöste Elektronenspektroskopie zur vollständigen Charakterisierung von Photoionization und Augerzerfall Dissertation, Universität Bielefeld, (2001)
- [67] K. D. Sevier Low Energy Electron Spectroscopy Chapter 3: M. E. Rudd Electrostatic Analysers.
- [68] G. Snell Spinaufgelöste Elektronenspektroskopie an freien Xenon- and Argonatomen mit zirkular polarisierter Synchrotronstrahlung Dissertation, Universität Bielefeld, (1997)
- [69] G. Snell, M. Drescher, N. Müller, U. Heinzmann, U. Hergenahn, J. Viefhaus, F. Heiser, U. Becker, and N. B. Brookes *Phys. Rev. Lett.* **76**, 3923 (1996).
- [70] G. L. Squires: Practical Physics - revised edition 1976 McGraw-Hill.
- [71] J. Tulkki, H. Aksela, N. M. Kabachnik *Phys. Rev. A* **50**, 2366 (1994).
- [72] G. Wendin and M. Ohno, *Phys. Scr.* **14**, 148 (1976).
- [73] G. K. Woodgate Elementary Atomic Structure 2nd Edition Clarendon press Oxford 1980
- [74] F.J.Wuilleumier, M.O. Krause, *Phys. Rev. A* **10** 242 (1974).

11 Acknowledgements (Danksagung)

This thesis is the result of my work in the chair for Molecular and Surface Physics, Bielefeld University with the financial support from the German Research Council (Deutsche Forschungsgemeinschaft).

I am extremely grateful to my supervisor Professor Dr. Ulrich Heinzmann who gave me the opportunity to work in his research group as a PhD student and to participate in the research of circular dichroism in the angular distribution of photoelectrons of bromocamphor molecules at BESSY I and to perform experiments in the field of spin resolved electron spectroscopy at BESSY II where I had the possibility to work with synchrotron radiation in photoionization experiments. I am indeed very thankful for his full this support which enabled me to do my PhD work.

I am very grateful also to Dr. Markus Drescher for his very supportive supervision during my whole time in Bielefeld, and his kind and valuable assistance in Berlin, especially when experimental problems were faced during the limited time slots available for measuring at BESSY II.

I thank Prof. Dr. N. M. Kabachnik and Prof. Dr N. A. Cherepkov for their discussions on the theory.

I thank Dr. Bernd Schmidtke from whom I gained through great scientific experience in the field of the experiment and through discussion of the theory.

The constant interest shown by Dr. Norbert Müller in the details of the experiment and the discussion of the theory and the analysis of the experimental data as well as active participation in the experiment in the laboratory and in Berlin were invaluable. It was a great pleasure to learn from such an enthusiastic physicist.

My thanks are due especially to Dr. Oliver Wehmeyer for his kind support, to Dr. Martin Pohl for his help both in Bielefeld and in Berlin, to Dr. Michael Spieweck, to Dr. Ulf Kleineberg and to Thomas Westerwalbesloh for their great assistance.

I thank Toralf Lischke and Dr. Norbert Böwering with whom I participated in the experiment of circular dichroism in the angular distribution of photoelectrons of bromocamphor molecules at BESSY I.

I thank Dr. Peter Siffalovic, and Martin Michelswirth for their experimental support, Thorsten Uphues for his support in Berlin in the experiment and in networking the computers and Christian Meier for his support in computer management.

I thank the secretaries Ms Kay Lofthouse, Ms Karla Schneider and Ms Karin Wisotzky.

In particular I would like to thank Mr Volker Schimmang for his technical support and the great help in transporting the experiment to Berlin, and all my colleagues in the Faculty of Physics, especially the Mechanical Workshop team with Mr Gronemeyer and the Electronic Workshop team with Mr Wild and Mr Retzlaff.

I thank all the staff at BESSY II for their friendliness and the excellent working conditions.

12 Oath (Eidesstattliche Erklärung)

Hiermit versichere ich, die vorliegende Arbeit eigenständig and ohne fremde Hilfe durchgeführt zu haben. Alle benutzten Hilfsmittel sind in der Literaturliste kenntlich gemacht.

Bielefeld, Dezember 2002

Tarek Khalil

13 Curriculum vitae

Tarek Khalil

Date and of birth 17.10.1963 /El Giza , Egypt

Marital status Married

Nationality Egyptian

School

1980 Gamal Abdel-Nasser secondary school
General Secondary Education Certificate Examination

Study in Cairo

1980 – 1985 Cairo University: Faculty of Science
BSc in Biophysics

1.1.1986 – 1.3.1987 Egyptian Army

Graduation courses in Germany

1988 – 1889 Course in the German Language at University of Cologne, Germany.

1990 – 1999 Study at the Faculty of Physics of
Ludwig–Maximilians–University of Munich, Germany.

Since 1999 Scientific employee and PhD student at the Faculty of Physics,
University of Bielefeld, Germany.